2011

Long-Term Quantitative Microscopy: From Microbial Population Dynamics to Growth of Plant Roots

Zak Frentz

LONG-TERM QUANTITATIVE MICROSCOPY: FROM MICROBIAL POPULATION DYNAMICS TO GROWTH OF PLANT ROOTS

A Thesis Presented to the Faculty of
The Rockefeller University
in Partial Fulfillment of the Requirements for
the degree of Doctor of Philosophy

by

Zak Frentz

June 2011

LONG-TERM QUANTITATIVE MICROSCOPY: FROM MICROBIAL POPULATION DYNAMICS TO GROWTH OF PLANT ROOTS

Zak Frentz, Ph.D.
The Rockefeller University 2011

Quantitative optical measurements at the micron scale have been crucial to the study of multiple biological processes, including bacterial chemotaxis, eukaryotic gene expression and fly development. Extending measurements to long time scales allows complete observation of processes that are otherwise studied piecemeal, such as development and evolution. This thesis describes the development of two types of microscope for making long term, quantitative measurements, and the tools for image analysis.

The first device is a digital holographic microscope for measuring microbial population dynamics. It allows three dimensional localization of hundreds of cells within a mm^3 sized volume, at micron resolution and an acquisition period of minutes. The technique is simple and inexpensive, which enabled us to construct ten replicate devices for parallel measurements. Each device incorporates precise and programmable control of light and temperature for the microbial ecosystem. Experiments were performed with the green algae *Chlamydomonas reinhardtii* and the ciliate *Tetrahymena reinhardtii*, both together and in isolation, and continued for as long as 90 days. The population dynamics exhibited a striking degree of repeatability, despite the presence of added noise in the illumination, spatial gradients of cell density, convection currents and phenotypic changes of both species.

The second device is a thin light sheet fluorescence microscope for tracking nuclei in growing roots of the flowering plant *Arabidopsis thaliana*. The device incorporates a chamber designed to maintain optical quality while providing conditions for root growth. Optical feedback to a translation stage is used to maintain the root tip in the field of view as the root grows by centimeters over several days. Data from a three day experiment is presented to demonstrate the technique. Over 1,000 nuclei were tracked simultaneously, and hundreds of cell divisions were automatically identified. The device was also used to image the regeneration of a root tip after surgical excision. The data corroborate earlier investigations at a more detailed level than was previously possible.

To Marie Frentz, who showed me how to tinker.

Ignignokt: You and your third dimension.
Frylock: What about it?
Ignignokt: Oh, nothing, it's cute. We have five.
[Pause]
Err: Th... Thousand!
Ignignokt: Yes, five thousand.
Err: Don't question it!
Frylock: Oh yeah? Well, I only see two.
Ignignokt: Well, that sounds like a personal problem.
-*Aqua Teen Hunger Force*

Acknowledgements

The years spent on the work presented in this thesis were fun and full, and I believe I learned some lessons throughout. I would like to thank several colleagues who made this project not only possible, but also a pleasure. In particular, I thank

First, my advisor Dr. Stanislas Leibler. Stan's enthusiasm, laments, honesty, and constant stream of ideas have been inspiring and influential. He has tried to show me how to write and how to give a talk and I hope he has succeeded to some extent. The lab has been my favorite place to be for many years now, with talented collaborators and interesting speakers, and I doubt there are many places like it.

Seppe Kuehn and Giovanni Sena, with whom I worked very closely. Seppe and I worked together to develop digital holographic microscopy for measuring population dynamics of microbes. I think we have thoroughly explored the possible combinations of each of us thinking that the project would never work or feeling confident in its success. I am grateful for his many efforts, and for his open-mindedness, patience and perseverance. Giovanni wanted to study regeneration in plant roots. Starting with a version of the thin light sheet microscope that Doeke had designed for measuring population dynamics, we developed a device for tracking cell nuclei for many days in growing *Arabidopsis* roots. While the microscopy was fairly straightforward, the steps in designing a growth chamber and protocol for growing roots in the microscope ranged from challenging to hilarious. I am grateful for his positive attitude and curiosity, and for teaching me some impolite Italian words from across the lab.

Doeke Hekstra, who introduced me to Rockefeller and to the lab. His bravery and scientific skills have made the quantitative and long term study of closed microbial ecosystems possible. He is kind, clever and helpful, and working with him has been a joy.

Other present and former members of the lab: John Chuang for comments on drafts and for help with microcontrollers and code, Sriram for electronics help, Jack Merrin and Remy Chait for introducing me to the machine shop, and Clément Nizak and Edo Kussell for welcoming me to the lab and working with me on some early projects.

The members of my thesis committee. Dr. Shai Shaham and Dr. Albert Libchaber have been supportive and insightful throughout, and their many

questions in our meetings are much appreciated. I am honored to have Professor Howard Berg as external member of my committee, whose exploration of bacterial chemotaxis influenced my decision to pursue science.

Dr. Ken Birnbaum, for his help with the project on plant roots. His knowledge and advice were much needed.

Dr. Tony Maggs, for his help with holographic reconstructions and image analysis.

Professors S. R. Srinivasa Varadhan and Esteban Tabak, for their courses in probability and statistics.

The Information Technology department, especially Bala Jayaraman, Vlad Maynfeld and Tushit Shukla.

The Dean's Office and the David Rockefeller Graduate program, for support and freedom.

Dan Larson and Yasser Roudi, who have been invaluable colleagues and dear friends. I thank them for sharing ideas, knowledge, pork chops and beer.

My family and friends have shown me much love and support, and deserve better thanks than I can write. I love you all.

Table of Contents

List of Figures

List of Tables

Chapter 1

Introduction to closed ecosystems

1.1 Ecology and Evolution

The interactions an organism makes with its environment and with other organisms determine its success in survival and reproduction. At the population level and time scales of many generations[1], those interactions represent evolutionary pressures, which are in general dynamic. Compared to the processes of mutation, drift, and gene flow, the mechanisms through which interactions determine selection and the effects of the dynamic nature of interactions are largely unknown.

Progress requires phenomenology - with few strong experimental results, theory is unconstrained and predictions are difficult. Models of population dynamics in ecosystems with many species require at least one dimension per species, and interactions in a branching process are necessarily non-linear, so that even the simplest models of interacting species can have very rich dynamics. It is not even clear that simple models should exist, since if there is in reality a set of equations which determine the population dynamics, the phase space may have very many dimensions, and it may be the case that none of these dimensions corresponds to the number of individuals

[1] In this text, time scales are measured in terms of the generation time of the species studied, τ_{gen}. Long time scales refer to durations $\tau \gg \tau_{gen}$. When multiple species are present, the longest generation time is used. In many experiments, generation times are not measured or known - in this case, typical generation times for the relevant species are used.

of a given species. For example, the concentrations of various chemical moieties may have important roles in the dynamics(26). Even for simple models which only include population sizes, it is not trivial to formulate a model of interacting species which is realistic and generally predictive.

For example, the Lotka-Volterra equations(21) for two species interacting as predator and prey have a saddle at the origin (extinction of both species) and another fixed point around which all trajectories are limit cycles. This model has a feature which is quite unrealistic biologically - periodic solutions approach very low populations of prey, and in the absence of predators, prey populations diverge exponentially. A more realistic model can be defined, by introducing a carrying capacity, and this model can be considered for n interacting species; however, provided that the number of species is large enough ($n \geq 5$ for competitive Lotka-Volterra equations), by varying the parameters the solutions can have any dynamical behavior, including fixed points, limit cycles, and chaotic attractors(25). Such flexibility is a general feature of ecological models. Without a method for estimating interaction coefficients or constraining the form of the dynamics, these models cannot say much about how interactions determine selection pressures or ecosystem dynamics.

Although the population sizes may not strictly determine the dynamics of an ecosystem, they are certainly important evolutionary variables. As thermodynamics shows, it is possible that systems with many degrees of freedom can be described more simply. Some phenomenology can be established experimentally: What types of dynamical behaviors are possible in ecosystems? How does the number of species comprising an ecosystem influence population dynamics? How are dynamics different for ecosystems of lab strains which are artificially mixed compared to strains which have coevolved, and can this reveal selection at the ecosystem level? How do environmental fluctuations influence population dynamics, and how do ecosystems adapt to these fluctuations? These remain open questions.

1.2 Repeatability

The repeatability of ecosystem dynamics is especially relevant to this thesis: given the sources of randomness inherent to biological systems, how do the outcomes differ for replicate preparations of ecosystems and repetitions of the same experiment? This question rarely arises in the ecology literature, since natural ecosystems can hardly be prepared in replicate with defined initial conditions. However, the related concept of ecosystem stability is central to ecology, with practical applications for conservation biology.

Since theoretical and experimental work deal with individual ecosystems, stability is defined in terms of the temporal behavior of the system, and various types are studied depending on the dynamics of the system and the perturbations applied(15). These definitions are most useful when the dynamics of the system are known; for most experimental systems the dynamics are not known even approximately, and fluctuations are taken to be the high frequency components of the dynamics remaining after subtraction of a trend. This separation is arbitrary and possibly incorrect, as nonlinear systems and chaotic systems in particular have broadband power spectra even in the absence of stochasticity(8). Ecosystems can exhibit rapid responses to boundary condition perturbations, especially in spatial distribution (see chapter 4). In ecological studies these responses often occur on time scales shorter than the measurement period(5, 23). In addition, temporal measures of stability derived from single systems cannot separate random fluctuations due to intrinsic factors, such as demographic effects, phenotypic switches or mutations, from those due to extrinsic factors, such as environmental fluctuations.

If many replicate ecosystems are available and the boundary conditions can be carefully controlled, several more useful characterizations of dynamics can be considered. These quantify the repeatability of the dynamics: if many identical or very similar

replicates are maintained in identical boundary conditions, how similar do they remain over time?

For ergodic, deterministic dynamical systems this is described by the spectrum of Lyapunov exponents, which are the exponential rates of separation of infinitesimally close points along various directions, averaged over time(22). The positive exponents, which determine repeatability, can be estimated from a single time series without explicit knowledge of the underlying dynamics(7, 8). For practical purposes the positive exponents quantify the sensitivity to initial conditions or to small perturbations imposed without changing the dynamical laws. However, this approach requires recurrence in the data, so that the linear approximation to the underlying map can be estimated without overfitting. Measurement noise can severely limit the estimation of Lyapunov exponents, and although the concept of Lyapunov exponents can be extended to inherently stochastic systems(4), algorithms for estimating these exponents from time series are not known. Since typical ecosystem dynamics are inherently stochastic and there is no reason to expect multiple recurrence or ergodicity of the population dynamics, the Lyapunov exponents are not the most practical metrics of repeatability.

Our analyses will employ statistical measurements of repeatability, namely the coefficient of variation (CV) and the standard deviation of the logarithm of cell counts, $\sigma(\log n)$. These quantities are useful for characterizing the differences across replicate ecosystems in which temporal fluctuations tend to be multiplicative. This is likely the case for any ecological system which exhibits a large dynamic range, as the known sources of change, i.e. birth and death, occur at rates proportional to the cell density. The CV and $\sigma(\log n)$ are approximately equal when the deviation is small compared to the mean. Either measure will be referred to as the divergence, and its behavior over time will be of especial interest.

1.3 Experimental Systems

Mutation, drift and gene flow can be defined for a population of organisms, conditional on the environment in which they are studied, and results can be obtained in well controlled laboratory conditions, often within a few generations. In contrast, study of environmental and intra-species interactions requires either field research, which typically involves large, complex and singular sites of undefined species composition and uncontrolled boundaries, or laboratory study, which requires development of model systems.

Microbial systems are particularly useful for laboratory study, due to short generation time, ease of cultivation of large populations, tractable genetics, and growth in defined media. Over intermediate time scales, microbial environments can be controlled experimentally(13, 19), and manipulated dynamically(3, 6, 9). Evolutionary time scales of several thousand generations have been studied, using batch culture and serial transfer (20) and continuous culture(29). However, using these methods to maintain populations of multiple species for long times is onerous and often impossible due to extinction or sporulation(16, 28), although exceptions exist(11). Interactions between organisms can involve excreted proteins and small molecules, so methods which involve replacing media either continuously or periodically may obscure interactions by dilution.

Closed ecosystems present a solution to many of the experimental limitations of serial transfer and continuous culture. These are populations of organisms in liquid culture housed in a transparent vessel which is sealed to prevent material exchange(14, 27). Closing the system to material exchange preserves chemical interactions, avoids contamination and the chore of replacing medium, and simplifies the definition of the boundary. Cubic centimeter sized ecosystems are persistent for as long as 1000 days, making them ideal for the long term study of many replicates.

Research in closed ecosystems began in the context of space exploration, with the goal of providing life support systems for humans on extended missions through ecological turnover(27). Smaller closed ecosystems were used to show that metabolic activity could persist for as long as 9 years, and suggested that closed ecosystems exhibited positive feedback controls to variations in initial conditions(18). A commercial closed ecosystem called the EcoSphere is a sealed glass sphere filled with filtered sea water containing uncharacterized microbes, tiny shrimp, algae, gravel, shells, dead coral and air (shown in Figure 1.1)(12). Closed ecosystems of known species composition were developed and studied by Doeke Hekstra in the laboratory of Stanislas Leibler(14), motivating the methodologies developed in this thesis.

The closed ecosystems studied by Hekstra were adapted from three species ecosystems consisting of *Escherichia coli*, *Euglena gracilis* and *Tetrahymena thermophila*, which had been shown to persist for 130 days, although the sealing of those ecosystems was not discussed(17). *Euglena* was replaced by the smaller alga *Chlamydomonas reinhardtii*, and *E. coli* and *T. thermophila* were transformed with fluorescent protein to create a three species ecosystem whose population dynamics could be measured by fluorescence microscopy(14). Ecosystems were prepared in small (4 cm^3) glass cuvettes, sealed with screw tops, and measured in a custom microscope employing selective plane illumination(10, 14).

In one set of experiments, several replicate ecosystems were housed in an incubator providing constant temperature and illumination, and individually transferred by hand to the microscope to measure population densities. In 25 of 27 systems, all three species persisted for at least 90 days. Typical ecosystem population densities were below $10^6\,cm^{-3}$, and the imaged volume was on the order of nanoliters. To obtain a reliable estimate of population density required measurement durations of 30-60 minutes.

In the first experiment, 9 ecosystems were measured for ten weeks at a frequency of 4 to 7 per week; in the second, 50 replicate ecosystems were measured for 90-100 days

Figure 1.1: Ecosphere - a commercially available closed ecosystem containing shrimp, algae and microbes. Taken from the EcoSphere website (`http://www.eco-sphere.com/index.html`).

at frequencies of 2, 1, 0.5, 0.25 and 0.125 per week. The mean dynamics from both experiments and all measurement frequencies were similar. The divergence of population densities across systems was measured by $(\det \Sigma_{ij})^{1/6} = |\mathrm{cov}(\log n_i, \log n_j)|^{1/6}$, which is the equivalent of $\sigma(\log n)$ for a three species system. The divergence exhibited a linear increase with time up to day 60, followed by an apparently saturating slower increase until the end of the experiment. Manual inspection of ecosystems at the end of the experiment revealed strong, variable spatial heterogeneity, with high concentrations of debris and live cells on many cuvette bottoms and near the water-air interface,

and adhering colonies on vertical walls. *E. coli* was observed in several phenotypic states, including microcolonies, filamentous networks and a three dimensional matrix. In some systems, large *T. thermophila* positive for chlorophyll were observed, indicating the generation of a phenotype capable of consuming *C. reinhardtii*.

The presence of phenotypic differences, spatial heterogeneity and divergence in population densities underscores the importance of studying many replicates, as ecosystems contain many potential sources of randomness. Some uncharacterized variation exists in the initial conditions no matter how carefully they are prepared, and processes like mutation and phenotypic switching are inherently stochastic. Since dynamics may be sensitive to variations in the initial conditions or to the random changes that occur in the course of an experiment, drawing conclusions from a single realization of an ecological experiment cannot be justified. Rather, a statistical characterization must be made from measuring replicates. The number of replicates which should be measured depends on the system, as well as the questions being asked.

The ideal methodology would achieve automated measurement from multiple replicate ecosystems and extend measurements to a larger region ($\gg$ nL) of each ecosystem, while still meeting the requirement of counting individuals non-invasively at frequencies of minutes for durations of months. Spatial heterogeneity may result in large artifacts due to stirring caused by sample loading, so in situ measurements are preferable.

Selective plane illumination microscopy combined with a motorized stage could be used to scan several systems housed in the microscope chamber, while sampling larger volumes within each single system. However, the reliance on moving parts for long term experiments and the limitations of speed imposed by scanning ruled out this approach. Flow cytometry has been automated to measure population dynamics of yeast, but the duration of these experiments has been limited to 40 hours(1). The flow and dye required for this technique violate the criterion of non-invasiveness. Bulk measurements such as optical density or total fluorescence do not count individuals

and so can be influenced by aggregation, morphological changes or fluctuations in fluorescence intensity. Work with microfluidic chemostats has achieved measurements of population dynamics at single cell resolution for hundreds of hours via fluorescence microscopy(2). It is not known if ecosystems can be designed which persist in such small volumes (nL scale, or a cube with 100 μm sides), however the synthetic three species ecosystems developed by Hekstra exhibit frequent extinction events at volumes below 150 mm^3(14).

Digital inline holographic microscopy is a simple and inexpensive optical technique for imaging dilute suspensions of small objects in three dimensions by computing diffraction integrals from two dimensional recordings of interference patterns(30). It has been used to image microliter sized volumes, track algae performing chemotaxis and study the swimming behavior of dinoflagellates preying on motile algae(24, 30). It has not been used to measure population dynamics. The main difficulties lie in automating image analysis for cell counting, as the imaging characteristics of holography depend strongly on location in object space, and out of focus light from large or bright objects can interfere with identification of organisms throughout the imaged region. By overcoming these difficulties we were able to achieve accurate counting of single species in isolation as well as two coexisting species. The optical system, reconstruction technique and image processing routines used to measure population dynamics in closed ecosystems are described in detail in chapter 2.

Bibliography

[1] Nicholas R. Abu-Absi, Abdelqader Zamamiri, James Kacmar, Steven J. Balogh, and Friedrich Srienc. Automated flow cytometry for acquisition of time-dependent population data. *Cytometry Part A*, 51A:87–96, 2003. 8

[2] Frederick K. Balagaddé, Lingchong You, Carl L. Hansen, Frances H. Arnold, and Stephen R. Quake. Long-term monitoring of bacteria undergoing programmed population control in a microchemostat. *Science*, 309:137–140, 2005. 9

[3] Erez Braun and Naama Brenner. Transient responses and adaptation to steady state in a eukaryotic gene regulation system. *Physical Biology*, 1:67–76, 2004. 5

[4] Andrew Carverhill. Flows of stochastic dynamical systems: ergodic theory. *Stochastics*, 14:273–317, 1985. 4

[5] Kathryn L. Cottingham and Daniel E. Schindler. Effects of grazer community structure on phytoplankton response to nutrient pulses. *Ecology*, 81:183–200, 2000. 3

[6] Blandine Descamps-Julien and Andrew Gonzalez. Stable coexistence in a fluctuating environment: An experimental demonstration. *Ecology*, 86:2815–2824, 2005. 5

[7] Jean-Pierre Eckmann, S. Oliffson Kamphorst, David Ruelle, and Sergio Ciliberto. Liapunov exponents from time series. *Physical Review A*, 34:4971–4979, 1986. 4

[8] Jean-Pierre Eckmann and David Ruelle. Ergodic theory of chaos and strange attractors. *Reviews of Modern Physics*, 57:617–656, 1985. 3, 4

[9] Sabine Flöder, Jotaro Urabe, and Zen-ichiro Kawabata. The influence of fluctuating light intensities on species composition and diversity of natural phytoplankton communities. *Oecologia*, 133:395–401, 2002. 5

[10] Eran Fuchs, Jules S. Jaffe, Richard A. Long, and Farooq Azam. Thin laser light sheet microscope for microbial oceanography. *Optics Express*, 10:145–154, 2002. 6

[11] Gregor F. Fussmann, Stephen P. Ellner, Kyle W. Shertzer, and Nelson G. Hairston Jr. Crossing the Hopf bifurcation in a live predator-prey system. *Science*, 290:1358–1360, 2000. 5

[12] J. A. Hanson and H. P. Stevens. Experimental ecosystems sealed in glass. Technical report, Jet Propulsion laboratory (NASA and CalTech), Pasadena, CA, 1984. 6

[13] Matthew Hegreness, Noam Shoresh, Doris Damian, Daniel Hartl, and Roy Kishony. Accelerated evolution of resistance in multidrug environments. *Proceedings of the National Academy of Sciences of the United States of America*, 105:13977–13981, 2008. 5

[14] Doeke Hekstra. *Population dynamics in a model closed ecosystem.* PhD thesis, The Rockefeller University, New York, New York, 2009. 5, 6, 9

[15] Anthony R. Ives and Stephen R. Carpenter. Stability and diversity of ecosystems. *Science*, 317:58–62, 2007. 3

[16] J.L. Jost, J. F. Drake, A. G. Fredrickson, and H. M. Tsuchiya. Interactions of *Tetrahymena pyriformis*, *Escherichia coli*, *Azotobacter vinelandii*, and glucose in a minimal medium. *Journal of Bacteriology*, 113:834–840, 1973. 5

[17] Z. Kawabata, K. Matsui, K. Okazaki, M. Nasu, N. Nakano, and T. Sugai. Synthesis of a species-defined microcosm with protozoa. *Journal of Protozoology Research*, 1995:23–26, 1995. 6

[18] Elizabeth A. Kearns and Clair E. Folsome. Measurement of biological activity in materially closed microbial ecosystems. *Biosystems*, 14:205–209, 1981. 6

[19] Roy Kishony and Stanislas Leibler. Environmental stresses can alleviate the average deleterious effect of mutations. *Journal of Biology*, 2:14, 2003. 5

[20] Richard E. Lenski and Michael Travisano. Dynamics of adaptation and diversification: A 10,0000-generation experiment with bacterial populations. *Proceedings of the National Academy of Sciences of the United States of America*, 91:6808–6814, 1994. 5

[21] Alfred J. Lotka. Analytical note on certain rhythmic relations in organic systems. *Proceedings of the National Academy of Sciences of the United States of America*, 6:410–415, 1920. 2

[22] Aleksandr Lyapunov. *The general problem of the stability of motion.* Taylor & Francis Inc., Bristol, PA, 1992. Translated from Russian by Anthony T. Fuller. 4

[23] Daniel L. Potts, Travis E. Huxma, Brian J. Enquis, Jake F. Weltzin, and David G. Williams. Resilience and resistance of ecosystem functional response to a precipitation pulse in a semi-arid grassland. *Journal of Ecology*, 94:23–30, 2006. 3

[24] Jian Sheng, Edwin Malkiel, Joseph Katz, Jason Adolf, Robert Belas, and Allen R. Place. Digital holographic microscopy reveals prey-induced changes in swimming behavior of predatory dinoflagellates. *Proceedings of the National Academy of Sciences of the United States of America*, 104:17512–17517, 2007. 9

[25] Stephen Smale. On the differential equations of species in competition. *Journal of Mathematical Biology*, 3:5–7, 1976. 2

[26] Robert W. Sterner and James J. Elser. *Ecological stoichiometry: The biology of elements from molecules to the biosphere.* Princeton University Press, Princeton, NJ, 2002. 2

[27] Frieda B. Taub. Closed ecological systems. *Annual Review of Ecology and Systematics*, 5:139–160, 1974. 5, 6

[28] H. M. Tsuchiya, J. F. Drake, J. L. Jost, and A. G. Fredrickson. Predator-prey interactions of *Dictyostelium discoideum* and *Escherichia coli* in continuous culture. *Journal of Bacteriology*, 110:1147–1153, 1972. 5

[29] Holly A. Wichman, Jack Millstein, and J. J. Bull. Adaptive molecular evolution for 13,000 phage generations: A possible arms race. *Genetics*, 170:19–31, 2005. 5

[30] Wenbo Xu, M. H. Jericho, I. A. Meinertzhagen, and H. J. Kreuzer. Digital in-line holography for biological applications. *Proceedings of the National Academy of Sciences of the United States of America*, 98:11301–11305, 2001. 9

Chapter 2

Digital holographic microscopy for imaging microbes

Our goal was to develop a technique to simultaneously count individual microbes in several replicate aquatic ecosystems at a resolution of microns and minutes over durations of days and volumes of mm^3. To this end, we constructed 10 copies of a digital inline holographic microscope in a lensless configuration(12, 26). Image analysis software was developed to automatically identify individual organisms and to distinguish organisms from two species. This chapter briefly reviews the principles of holography, describes the technical aspects and performance of the device, and details the reconstruction process and image analysis algorithms for our implementation.

2.1 Holography

Holography describes the reconstruction of the three dimensional light distribution from an object or scene from a two dimensional recording. Holography was invented by Dennis Gabor, and demonstrated in 1948(7, 8). A spatially and spectrally filtered beam from a mercury arc lamp was focused by a microscope objective to provide a nearly coherent point source, used to illuminate an aperture inscribed with the names of Huygens, Young and Fresnel. The wave scattered by the aperture interfered with the unscattered portion of the reference beam, and the interference pattern was recorded

on photographic film. The film was developed as a transparent negative, which when illuminated by the reference beam produced an image of the aperture (Figure 2.1).

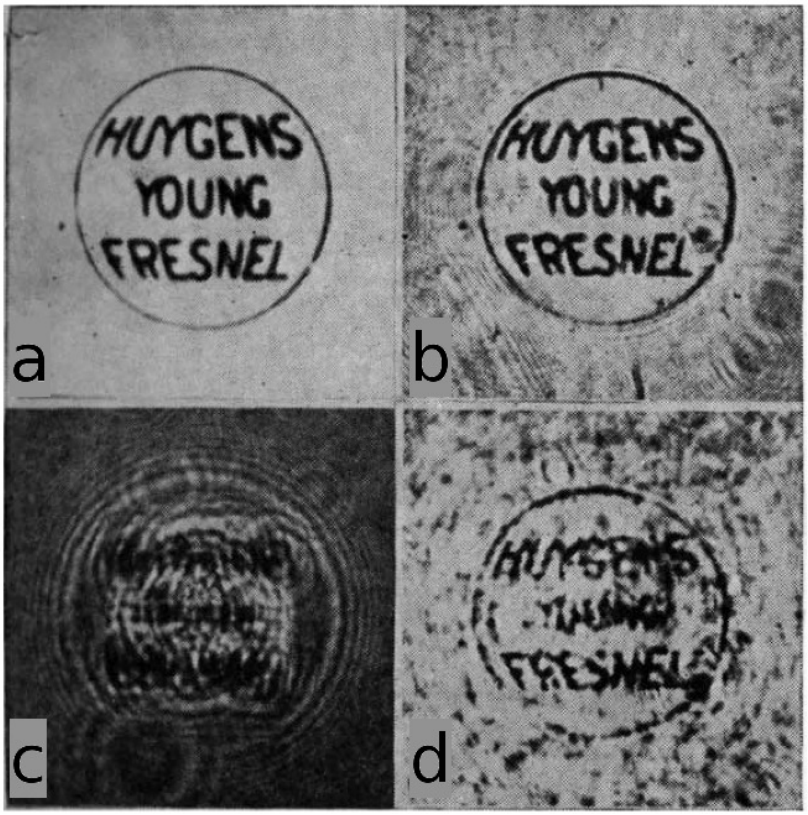

Figure 2.1: First demonstrated hologram and optical reconstruction - From Gabor, 1948(7): (a) original micrograph, 1.4 mm diameter (b) photograph of micrograph through reconstruction optics, for comparison to reconstruction (c) hologram (d) optical reconstruction from (c).

The principle of holography is a solution to a boundary value problem: the values of a coherent light wave's amplitude and phase on a closed surface contain all the information for reconstructing the amplitude and phase of that wave elsewhere in space, either physically, by illuminating the recording with a coherent wave with the same wavelength as the sample wave, or numerically, via a diffraction integral(1), as described in the next section. Light based holography can be used to image objects from the size of microns to meters, and the technique has been extended to x-rays and electrons(13, 24).

The sample is illuminated by a coherent wave and recordings are made in transmission or reflection. The same principle underlies some types of acoustic imaging, where the phase can be recorded directly due to sound waves' accessible temporal period ($\sim \mu$s)(16). Available optical sensors are orders of magnitude too slow to temporally sample the phase of light waves (period $\sim$ fs), so sample waves are interfered with waves of known or reproducible phase behavior to convert phase to amplitude. The interference pattern is called a hologram.

The illumination or reference wave can be split by a beam splitter and used to interfere with the sample wave at the recording plane. For samples of sufficiently low optical density, the portion of the reference beam which is unperturbed by the sample can be used to directly produce the interference pattern, which avoids splitting the beam; this technique is known as inline holography. The inline approach to microscopy minimizes the requirement of coherence length for the laser used to produce the reference beam, since the path lengths of the sample and reference waves largely overlap and can be as short as centimeters - commercial laser pointers are sufficient for inline holographic microscopy(9, 26).

2.2 Digital Holography

Quantitative measurement of the interference pattern allows numerical reconstruction of the sample wave, a technique called digital holography(11). Although proposed in 1967, digital holography was rarely utilized until the early 2000s, when digital image sensors with millions of micron sized pixels and computers capable of calculating reconstructions on time scales of minutes became readily available, at which point digital holographic microscopy matched traditional microscopy in resolution(2, 3, 19, 21, 26).

A drawback of digital image sensors for holography is their pixel size, typically measuring several micron per side. The interference pattern resulting from a microscopic

sample illuminated by a monochromatic plane wave of wavelength λ has fringes separated by a fraction of λ, with fringe spacing decreasing with increasing sample size. Undersampling the interference pattern results in degradation of reconstruction quality. The pixel spacing of most digital image sensors is at least a factor 10 too large to adequately sample optical holograms, and so for this purpose the fringe spacing must be magnified. Two techniques exist: fringes can be magnified by placing a magnifying lens system between the sample and the sensor(21), or the curvature of the reference wave can brought closer to the curvature of the sample wave by focusing it to a point source placed close to the sample(26), respectively known as Fresnel and lensless holography.

Besides sampling frequency, the demands of digital holography on image sensors are lax compared to fluorescence microscopy, which requires high sensitivity and low noise. For inline holography the scattering efficiency of the sample determines the signal to noise ratio and the laser intensity determines the exposure time - for microbial samples, interference fringes have amplitude orders of magnitude larger than the amplifier noise of commercial digital camera sensors, and exposure times can be on the order of milliseconds for low power lasers(9, 21). A gradient index (GRIN) lens can be used to create the point source reference wave(12); these lenses are inexpensive and can be easily coupled to optical fibers, producing from laser diodes point sources nearly free from aberrations. Laser diodes can be modulated electronically, while gas lasers must be shuttered either mechanically or by optoelectric modulator, methods which are unreliable over long times or bulky and expensive.

In constructing our implementation of lensless digital inline holographic microscopy we took advantage of the technique's flexibility by using relatively inexpensive components. The reference beam is provided by a 635 nm 1 mW laser diode (FMXL635-001, Blue Sky Research, Milpitas, CA), coupled to a single mode fiber which is glued to a custom GRIN lens assembly (GRINTech GmbH, Jena, Germany) consisting of a 6.2 mm glass spacer and a custom pitch, 0.5 NA GRIN lens. The beam exits the fiber at

a numerical aperture of 0.10 (e^{-2}) and the GRIN lens assembly focuses this to a spot on the outer surface of the lens with a numerical aperture of 0.27 (e^{-2}). Beams from laser diodes are astigmatic and spatially extended(25). We attempted to focus crudely collimated laser diodes but the resulting beams were highly heterogeneous in intensity and exhibited severe aberration, while the beams from the single mode fiber/GRIN lens assembly combinations were approximately Gaussian (Figures 2.2 and 2.3). Because the GRIN lens is flat it can be easily coupled with precise alignment to the fiber and the sample.

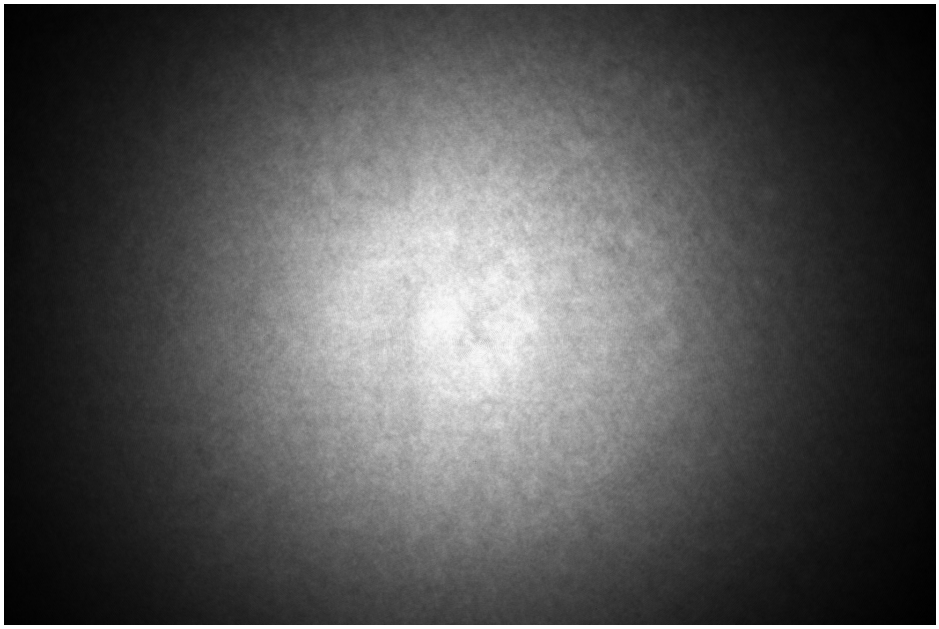

Figure 2.2: Example reference beam profile - median projection of 59 sequentially acquired holograms at relatively high cell density ($> 10^4$ /mL). The diagonal bands of intensity are due to reflection off a flat surface, presumably at the interface of the cuvette wall with air. Since these are present in raw holograms as well, the normalized hologram is not affected.

A commercial digital single lens reflex camera was adapted for use in our setup (3474 $\times$ 2314 square pixels, 6.4 μm pitch, Digital Rebel XT, Canon, Lake Success, NY). The camera body blocked proper access to the sensor so we removed the CMOS sensor from the camera body and electronically reattached it with 15 cm shielded ribbon

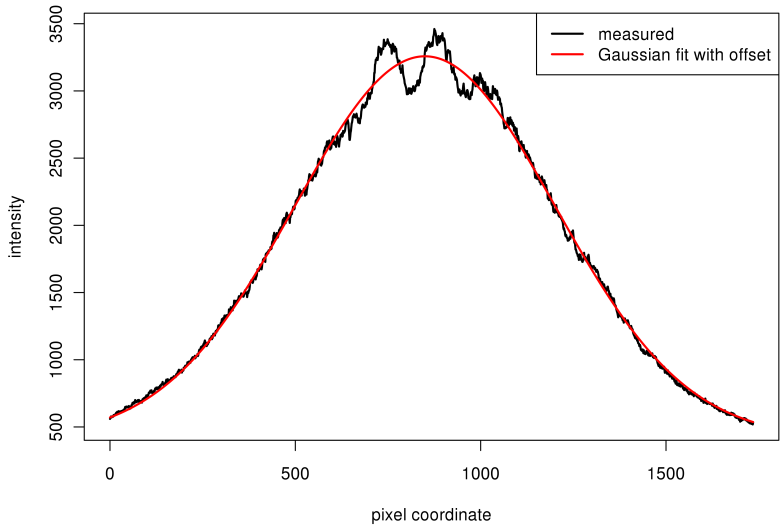

Figure 2.3: Gaussian fit to reference beam profile - fractional RMS of residuals was 0.038.

cables and connectors (Figure 2.4). The open source gphoto library is used to control camera acquisition and DCRAW is used to decode the raw formatted images (`http://gphoto.sourceforge.net`, `http://www.cybercom.net/~dcoffin/dcraw/`). The timing of camera exposure is not well controlled, so exposure times of 200 ms are used and a laser pulse is triggered by the computer via a digital to analog converter (DAC) (U3, LabJack, Lakewood, CA) once during the exposure. We could not remove the Bayer color filter deposited on the sensor above the light sensitive pixels, so we extract every fourth pixel corresponding to red-pass filters in the Bayer pattern.

The laser is powered by a custom circuit providing constant optical power with power and pulse duration adjustable by potentiometers (Figure 2.5). Pulse duration was set at 500 μs and power was adjusted to fill the dynamic range of the camera sensor. This pulse length is sufficiently short to prevent blurring of the fastest swimming organisms studied in our ecosystems; *Tetrahymena thermophila* swims as fast as 1 mm/s, or less than 500 nm per laser pulse.

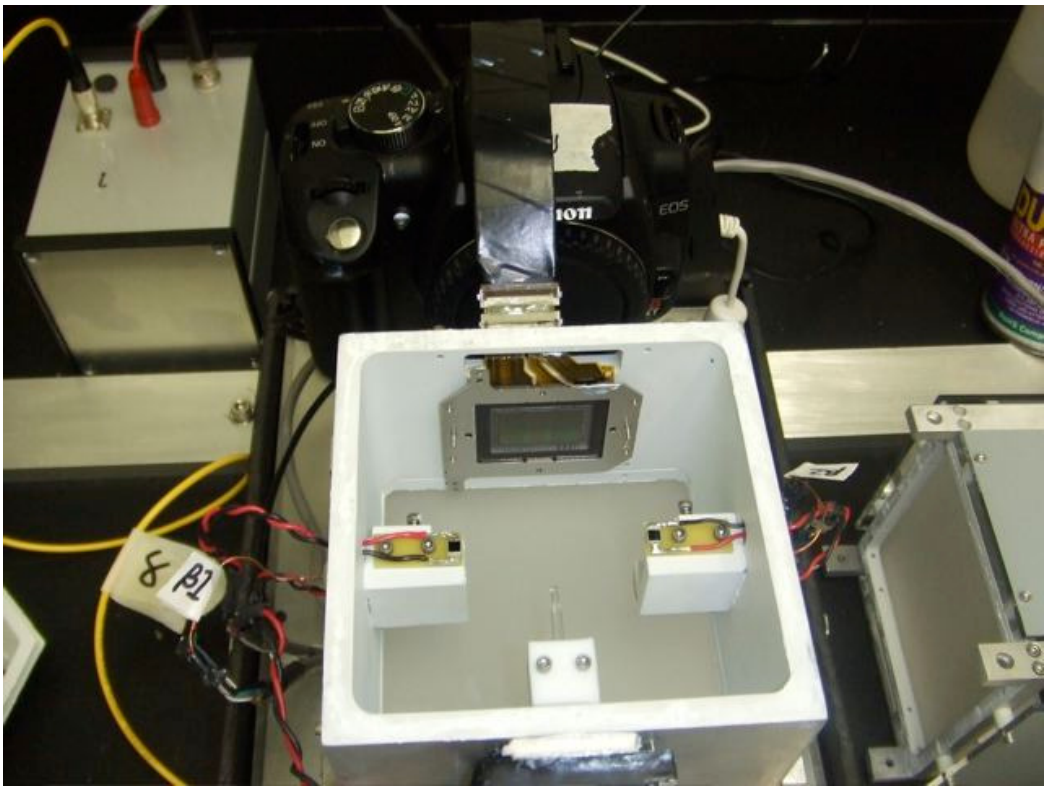

Figure 2.4: Photograph of DIH microscope optics

Illumination for photosynthesis is provided by two 1 W light emitting diodes (Luxeon , Philips, San Jose, CA), controlled by a current source adjustable by the computer through the DAC (FET/bipolar current source suitable for high currents, from Figure 4.12, Horowitz and Hill, 1989(14)).

We designed and machined an aluminum frame to house the optics, ecosystem sample and the LEDs for a prototype device. The laser is situated 46.5 mm from the sensor, and the beam is centered on the sensor to within 200 μm. Four photodiodes and two thermistors were placed on the aluminum sample holder and connected to a custom circuit to monitor LED intensity and sample holder temperature throughout experiments (Figures 2.7 and 2.6). We aimed to provide a homogeneous distribution of light intensity at the sample, to prevent preferential response by phototactic organisms. Two layers of diffusive plastic screens were placed between each LED and the sample.

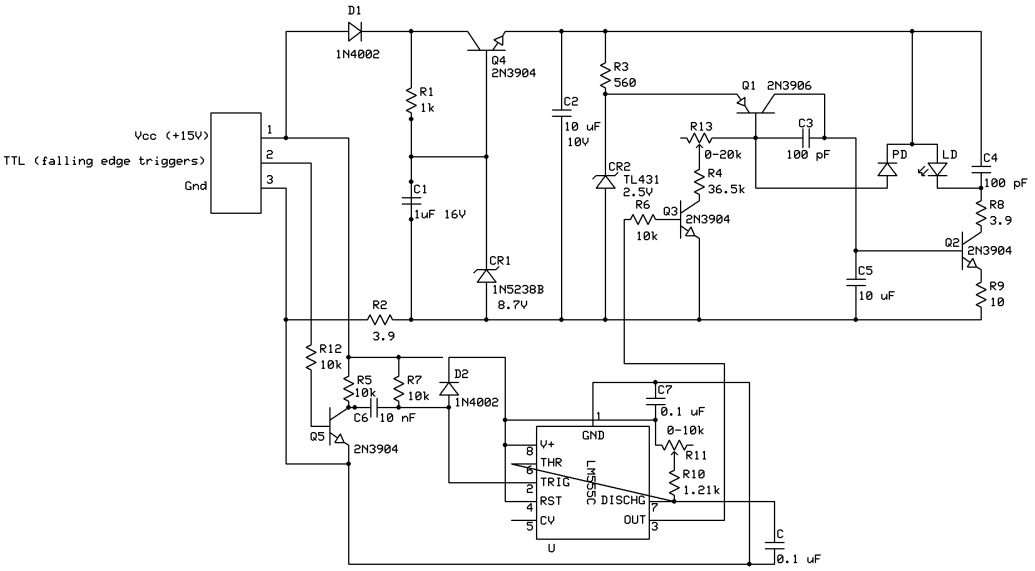

Figure 2.5: Laser diode modulation circuit diagram - adapted from SG-LD1 from Sam's laser FAQ (`http://www.repairfaq.org/sam/lasersam.htm`)

We initially attempted to provide homogeneous light distributions by surrounding the sample with a rectangular prism of polished transparent plexiglass, so that multiple internal reflections would smooth out the already broad beam from each LED. This method was abandoned due to difficulties imaging through plexiglass.

The sample consists of a rectangular quartz cuvette (inner dimensions 5 by 10 by 40 mm, wall thickness 1.25 mm, Starna Cells, Inc., Atascadero, CA) filled with transparent liquid medium, microbes and air. The cuvette is placed with one of its largest walls contacting the GRIN lens so that the laser beam enters the cuvette 2 cm from either horizontal end and offset by 2 mm below the vertical center to allow imaging in the presence of a significant air bubble (Figure 2.6). Index matching optical gel is spread on the face of the GRIN lens before pushing it against the cuvette wall.

Preliminary experiments were conducted on an optical table in a microscope room, with temperature controlled by a thermostat. While the optics of the prototype device were sufficient for high quality reconstructions, it was found that large oscillations in imaged cell counts of algae correlated with oscillation of the same period of $\sim 30 -$

60 min (Figure 2.8). We implemented temperature control of the sample holder using a Peltier element mounted to the plate of the optics frame holding the lens assembly, with feedback from one of the thermistors in the sample holder input to a custom proportional-integral-derivative (PID) feedback circuit (Figures 2.9 and 2.10). The side of the Peltier element which does not contact the sample holder frame is mounted to an aluminum heat pipe, which is insulated inside a light tight black cardboard box, and terminated with a large heat sink outside the cardboard box. The control has a time constant of approximately 90 seconds.

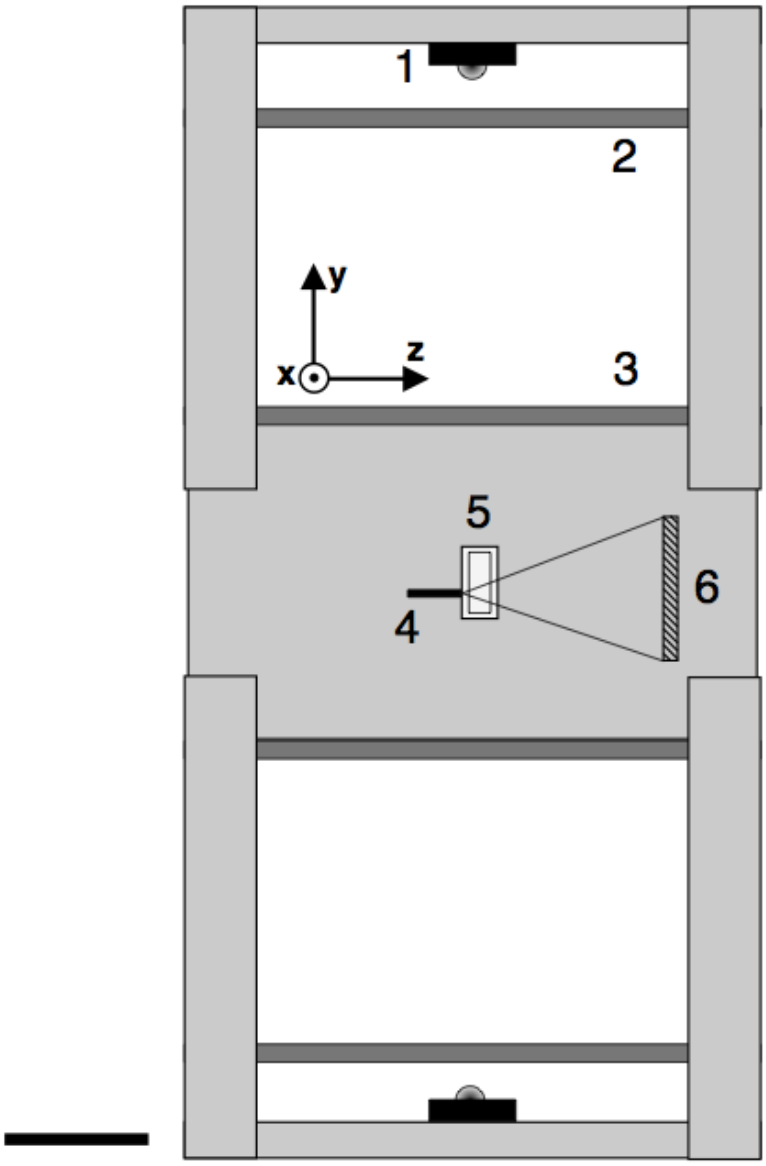

Figure 2.6: DIHM schematic - (1) white LED (2), (3) diffusive screens (4) GRIN lens assembly (5) sample cuvette (6) camera sensor. Gravity points along the negative y-axis. Scale bar: 25 mm.

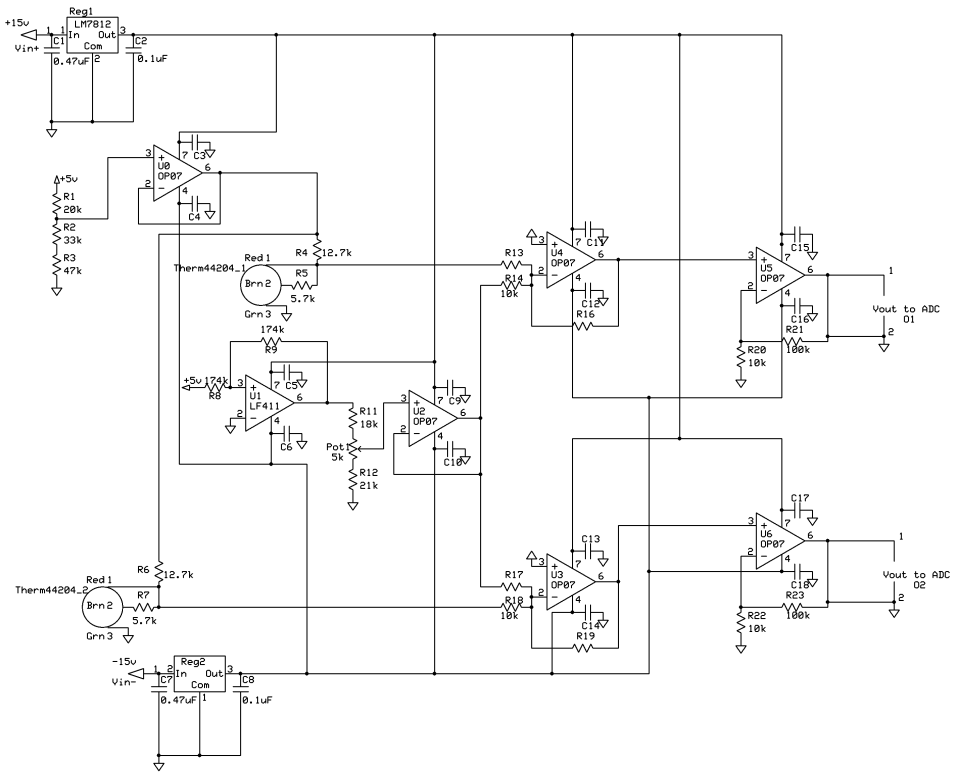

Figure 2.7: Amplifier for thermistor readings

Having tested the prototype device, we designed the final device for replicate construction. A commercial machine shop (eMachineShop, Mahwah, NJ, `http://www.emachineshop.com`) constructed replicate parts for the assembly of 10 devices, mostly of aluminum, to tolerances of 100 μm. The devices were assembled and mounted on silicone elastomers (NT35-264, Edmund Optics, Barrington, NJ) on a bench in a temperature controlled room maintained at 18 ± 0.1 C. Five of the microscopes are shown in Figure 2.11, and the array of computers controlling the ten microscopes is shown in Figure 2.12.

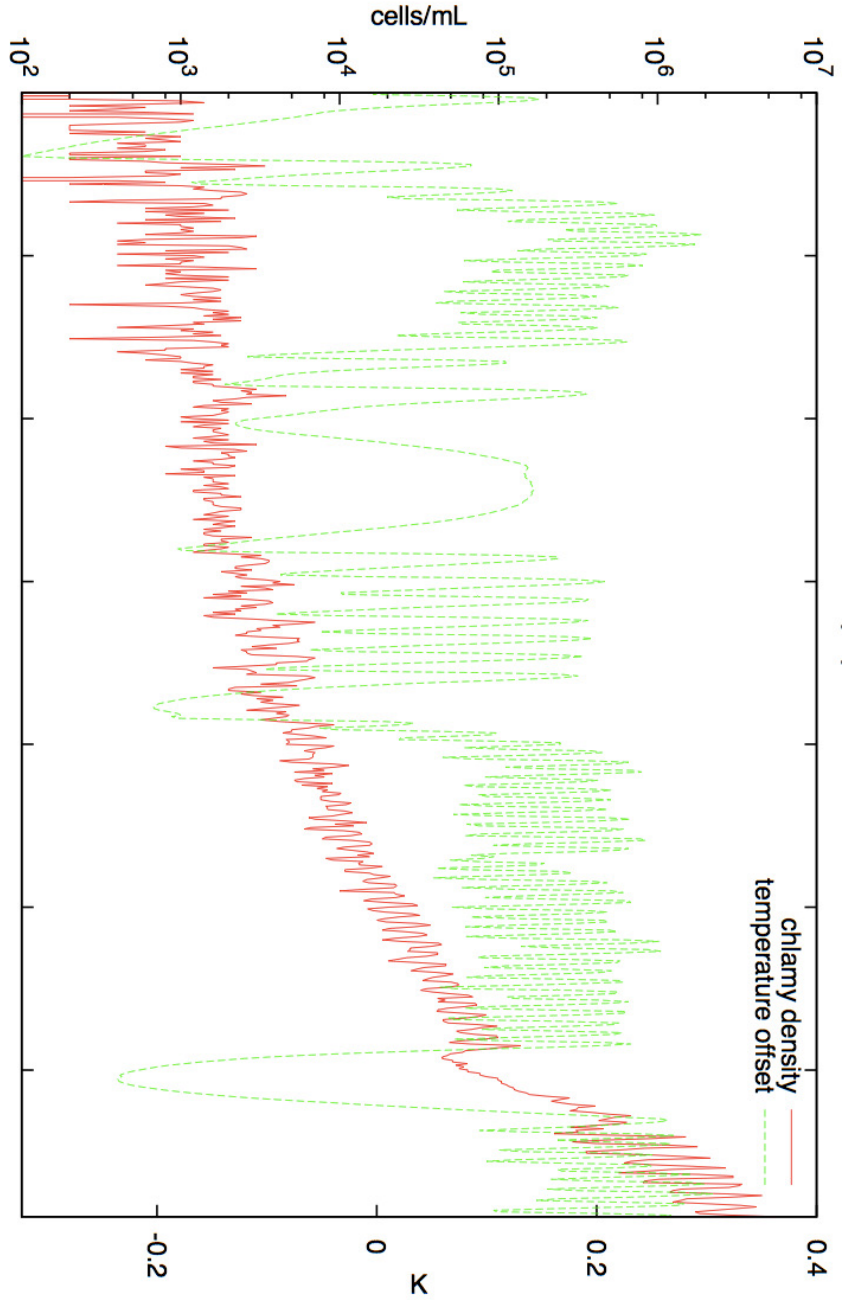

Figure 2.8: Temperature oscillations - Data from a preliminary experiment with *C. reinhardtii* showing large amplitude oscillations of population density, correlated with temperature oscillations. Temperature are plotted with an offset - mean temperature was around 20 C.

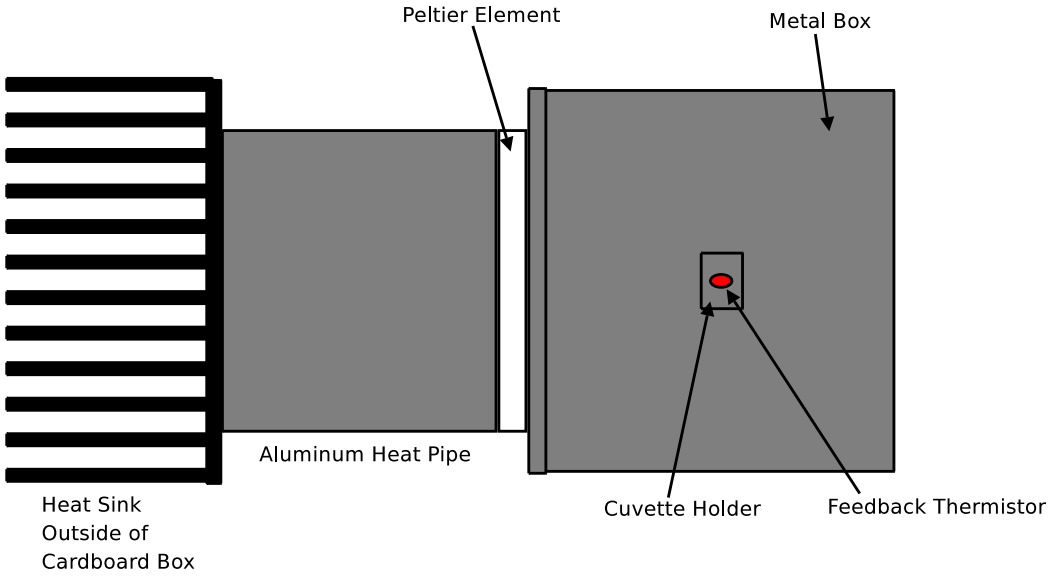

Figure 2.9: Temperature control schematic - A thermistor in the sample holder feeds back to a PID circuit controlling a current source powering a Peltier element.

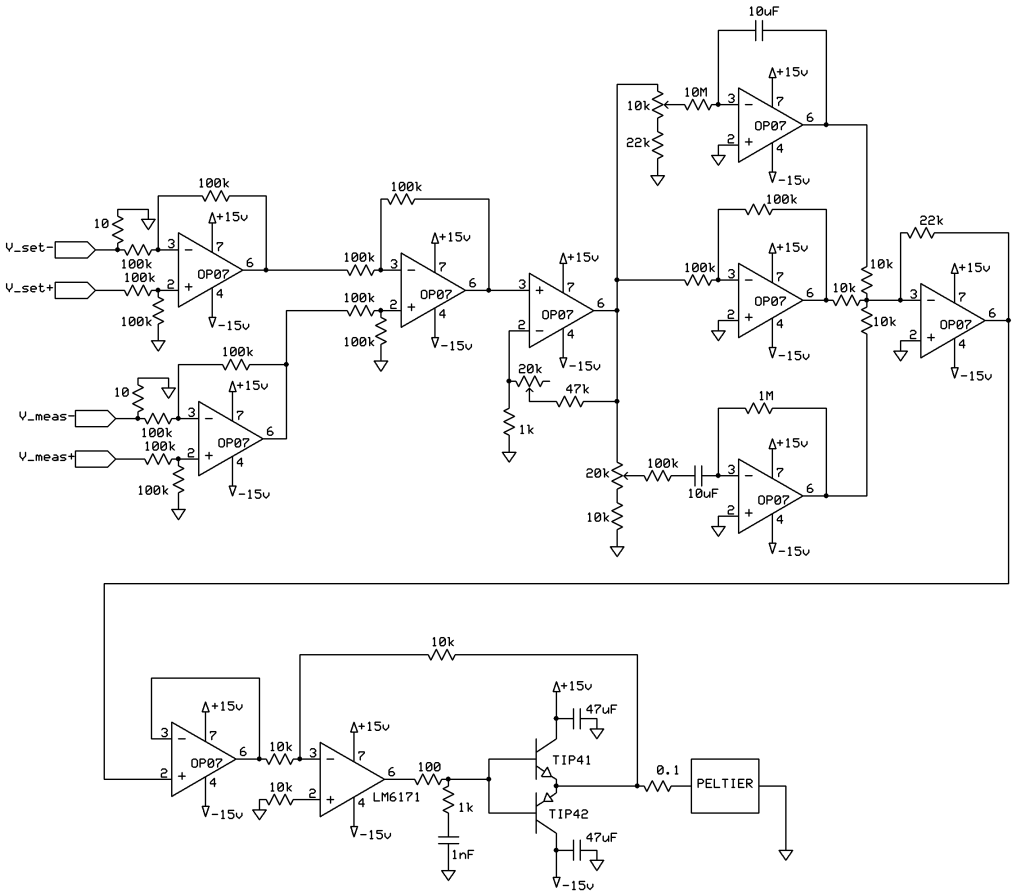

Figure 2.10: Temperature control PID circuit diagram

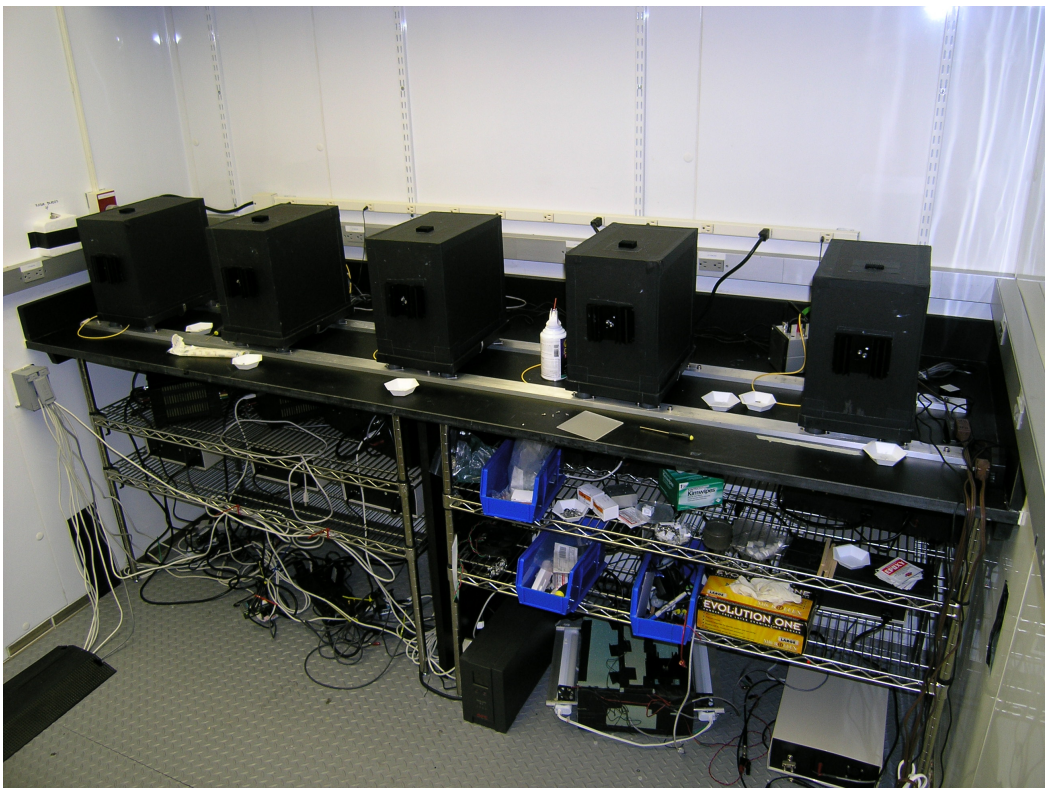

Figure 2.11: Photograph of DIH microscopes - five microscopes (black boxes) are shown on one half of an environmentally controlled room, in which temperature is 18±0.1 C.

Figure 2.12: Array of DIHM computers - ten computers, one for each microscope, control the acquisitions, record voltages from the ADC and perform reconstructions and analysis. Each computer is powered by an uninterruptible power supply, and connects to its microscope through USB cables entering the environmental room through a small hole drilled in the wall.

2.3 Reconstruction

Given the complex amplitude U_s of a wave on a surface S, the wave's value elsewhere can be calculated using the first Rayleigh-Sommerfeld diffraction integral(1, 18, 23), where we assume that the sensor and sample interfaces are perpendicular to the axis of the beam from the GRIN lens (this is true to a few milliradians):

$$U_s(\boldsymbol{r'}) = -\frac{ikz'}{2\pi}\int_S \frac{e^{ik|\boldsymbol{r}-\boldsymbol{r'}|}}{|\boldsymbol{r}-\boldsymbol{r'}|^2}U_s(\boldsymbol{r})\ dS \tag{2.1}$$

Consider a sample illuminated by a reference wave U_r, placed between the source of the reference and a camera sensor. If the sample scatters only a small fraction of the incident light, the wave at the sensor can be written as the sum of the scattered sample wave U_s and the unscattered reference wave:

$$U(\boldsymbol{r}) = U_r(\boldsymbol{r}) + U_s(\boldsymbol{r}) \tag{2.2}$$

for all $\boldsymbol{r}$ on the sensor. The sensor records the intensity:

$$\begin{aligned} I(\boldsymbol{r}) &= |U_r(\boldsymbol{r}) + U_s(\boldsymbol{r})|^2 \\ &= I_r(\boldsymbol{r}) + U_r(\boldsymbol{r})U_s^*(\boldsymbol{r}) + U_r^*(\boldsymbol{r})U_s(\boldsymbol{r}) + I_s(\boldsymbol{r}) \end{aligned} \tag{2.3}$$

which is called the hologram. The third term in (2.3) is proportional to U_s and if determined, can be used in equation (2.1) to image the sample. To this end, the first term in (2.3) can be approximately measured and its values (I_r') subtracted from the sample hologram:

$$I - I_r' \approx U_r(\boldsymbol{r})U_s^*(\boldsymbol{r}) + U_r^*(\boldsymbol{r})U_s(\boldsymbol{r}) + I_s(\boldsymbol{r}) \approx U_r(\boldsymbol{r})U_s^*(\boldsymbol{r}) + U_r^*(\boldsymbol{r})U_s(\boldsymbol{r}) \tag{2.4}$$

The measurement of the reference intensity I_r' can be accomplished by recording the reference wave passing through a cuvette filled with water or by making a temporal average of holograms acquired from a sample with low density of scatterers. The first method has the disadvantage that unless very precise ($< \mu$m) alignment is achieved for the water-filled and sample cuvettes, any scratches on the cuvette wall will The latter method has the advantage that contributions from The difference can then be normalized by the reference amplitude:

$$\frac{I - I_r'}{\sqrt{I_r'}} \approx U_s \exp(-i\phi_r) + U_s^* \exp(i\phi_r) + \frac{|U_s|^2}{\sqrt{I_r'}} \tag{2.5}$$

where I_r' is the measured reference intensity and $\phi_r(\boldsymbol{r})$ is the phase of the reference wave on the sensor. The last term can be ignored, since the small scattering assumption means $|U_s| \ll |U_r|$. In an experimental setup the phase of the reference wave is approximately known; for example, for a diverging spherical wave, $\phi_r(\boldsymbol{r}) \approx k|\boldsymbol{r} - \boldsymbol{r}_f|$ where k is the wavenumber and $\boldsymbol{r}_f$ is the focus of the spherical wave. This phase can be subtracted from the normalized hologram:

$$\frac{I - I_r'}{\sqrt{I_r'}} \exp\left(i\phi_r\right) \approx U_s + U_s^* \exp(i2\phi_r) \tag{2.6}$$

The first term represents the sample wave while the second, called the "twin image," has the form of the sample wave inverted about the reference beam focus. The presence of the second term is due to the ambiguity of the sign of the complex amplitude inferred by measuring intensity. For our setup, reconstruction planes within the sample place objects in the twin image out of focus by at least 2.5 mm (60 focal depths). Therefore the twin image contributes background which is dim and varies slowly in space, and so does not impede identification of focused objects. The contribution from the twin image is subsequently ignored.

The Cartesian axes are depicted in Figure 2.13: x is the horizontal axis through the

long dimension of the cuvette, and from the laser points to the right; y is the vertical axis and points opposite gravity; z is the optical axis, increasing from the reference source to the camera sensor. The x and y origins correspond to the center of the camera sensor. The z origin corresponds to the axial position of the source focus and is referred to as the proximal side. The cuvette walls correspond to $z \approx 1250\,\mu$m and $z \approx 6250\,\mu$m, varying 50 μm across microscopes.

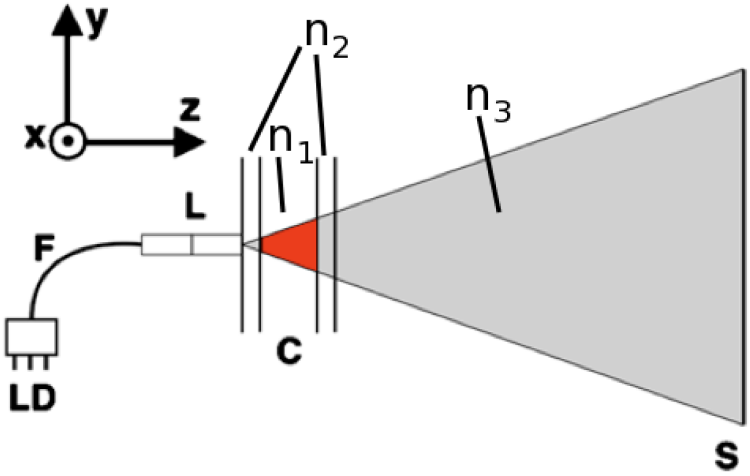

Figure 2.13: Imaging geometry - (LD) laser diode, (F) optical fiber, (L) GRIN lens assembly, (C) sample cuvette, (S) CMOS sensor. n_1, n_2 and n_3 label the refractive indices of water, quartz and air. The reference beam is shaded, and imaged region is colored red.

2.3.1 Distance approximation

The integral in (2.1) must be considered computationally. Although continuous integrals are written, all actual computations are discrete. Let N be the number of pixels on the sensor ($N \approx 4 \times 10^6$) and M be the number of planes to be reconstructed ($M \approx 10^2$). To reconstruct the entire imaged volume at the resolution of the device, $\boldsymbol{r'}$ must be calculated for NM points, while each integral over the sensor involves N points, which represents a daunting computation ($\sim 10^{15}$ floating point operations).

Since we wish to acquire data from experimental systems as rapidly as possible, a more efficient calculation is necessary.

The equation (2.1) is a convolution, and can therefore be calculated using two fast Fourier transforms (FFTs). However, each convolution yields a reconstructed image with sampling interval equal to the sampling interval of the hologram. For digital image sensors, this is typically several micron, and so achieving reconstructions sampled at the optical resolution of the microscope via convolution requires repeating the FFT many times with sub-pixel shifts in two dimensions. For our microscope the number of FFTs per plane necessary to achieve proper sampling is 288, which is prohibitively expensive, and can be reduced to 1 with the following approximation.

The exponent in (2.1) can be approximated in order to convert the integral to an FFT, reducing the number of calculations to $MN \log N \approx 10^{10}$ floating point operations. The approximation takes advantage of the small sample size relative to the object to sensor distance. All distances in this section are measured from an object origin $\boldsymbol{r_0}$ within the imaged region of the sample. Expand $|\boldsymbol{r} - \boldsymbol{r'}|$ in powers of $\frac{r'}{r}$:

$$|\boldsymbol{r} - \boldsymbol{r'}| = r - \frac{\boldsymbol{r}\boldsymbol{r'}}{r} + \frac{(\boldsymbol{r} \times \boldsymbol{r'})^2}{2r^3} + \dots \tag{2.7}$$

Using this expression in (2.1), keeping the first two terms in the exponent and the first term in the denominator, the diffraction integral is

$$U_s(\boldsymbol{r'}) \approx -\frac{ik(z' + z_0)}{2\pi} \int_S \frac{e^{ik(r - \boldsymbol{r}\boldsymbol{r'}/r)}}{r^2} U_s(\boldsymbol{r}) \; dS \tag{2.8}$$

which can be converted to a Fourier transform through change of variable. Introduce

variables u and v, and label the coordinates of $\boldsymbol{r} = (x, y, z)$:

$$\begin{aligned} r &= \sqrt{x^2 + y^2 + (z - z_0)^2} \\ u &= x/r \qquad\qquad\qquad\qquad v = y/r \end{aligned} \tag{2.9}$$

In these variables, (2.8) is

$$U_s(x', y', z') \approx -\frac{ik(z' + z_0)}{2\pi} \int\int e^{-ik(ux' + vy')} \frac{e^{ik(r - zz'/r)}}{1 - u^2 - v^2} U_s(ru, rv)\ du\ dv \tag{2.10}$$

which can be computed by FFT. The values of U_s are calculated from the normalized hologram by interpolation, and multiplied by $\frac{e^{ikr}}{1-u^2-v^2}$, then for each reconstruction multiplied by the phase $e^{ikzz'/r}$. The reconstructed wave is a complex amplitude, although in practice only its amplitude is used for image analysis.

2.3.2 Effects of phase approximation

Omitting additional terms in (2.7) results in aberrations in the reconstructed sample wave in the form of distortion and coma. These aberrations depend on the lateral spatial coordinates and so cannot be corrected numerically in the reconstruction by FFT. The most important effect of coma is to reduce the reconstructed intensities. Several processes cause strong spatial dependence in reconstructed intensity; these are considered together in section 2.5.1. Distortion causes a shift in the location of a reconstructed object relative to its actual location, and can be considered analytically[1].

Consider a scatterer at $\boldsymbol{r''}$: we use the next term in the expansion (2.7) to determine the reconstructed location to the next order in $\frac{r'}{r}$. The phase at the sensor is $\phi(\boldsymbol{r}) = k|\boldsymbol{r} - \boldsymbol{r''}|$ but the truncation to the first two terms in (2.7) adds aberration for a given

[1] In this section, it is assumed that all propagation occurs through vacuum, which is not the case for our setup. The extension to propagation through multiple media is trivial but lengthy and is omitted.

point of reconstruction $\boldsymbol{r'}$:

$$\tilde{\phi}(\boldsymbol{r}) = k\left(|\boldsymbol{r} - \boldsymbol{r''}| + \frac{(\boldsymbol{r} \times \boldsymbol{r'})^2}{2r^3} + \dots \right) \tag{2.11}$$

Distortion along the optical axis results in the largest displacements. Consider a point on the axis at $\boldsymbol{r''} = (0, 0, z'')$, which reconstructs at $\boldsymbol{r'} = (0, 0, z')$. Using the paraxial approximation, the phase at the sensor to third order in z' is

$$\tilde{\phi}(\boldsymbol{r}) \approx k\left(z - z'' + \frac{\rho^2}{2(z - z'')} + \frac{z'^2\rho^2}{2z^3} + \frac{z'^3\rho^2}{2z^4} \right) \tag{2.12}$$

where ρ is the lateral coordinate on the sensor: $\rho = (x^2 + y^2)^{1/2}$. The coefficient of $\rho^2/2$ determines the plane z' at which the aberrated wave focuses:

$$\frac{\rho^2}{2(z - z')} = \frac{\rho^2}{2}\left(\frac{1}{z - z''} + \frac{z'^2}{z^3} + \frac{z'^3}{z^4} \right) \tag{2.13}$$

Solving for z'' gives

$$z'' \approx z'\left(1 - \frac{z'}{z} + \frac{z'^2}{z^2} \right) \tag{2.14}$$

to second order in $\frac{z'}{z}$. In our setup, the shift from distortion reaches a maximum of 220 μm at the cuvette wall.

Distortion causes somewhat smaller lateral shifts: consider a scatterer at $\boldsymbol{r''} = (x'', y'', z'')$ which focuses at $\boldsymbol{r'} = (x', y', z')$. The lateral distortion can be calculated from the aberration $\Delta\phi$ for each point on the sensor(1):

$$\delta x' = |\boldsymbol{r} - \boldsymbol{r'}| \frac{\partial \Delta\phi}{\partial x} \tag{2.15}$$

where the aberration can be calculated to second order from (2.7):

$$\frac{\partial \Delta\phi}{\partial x} = \frac{1}{2r^3}\Big(2x\big(y'^2+z'^2\big) - 2\big(x'y'y + x'z'z\big) - \frac{3x}{r^2}\big(x'^2(y^2+z^2) + y'^2(x^2+z^2) + z'^2(x^2+y^2)\big)\Big) \tag{2.16}$$

A similar equation holds for the vertical shift $y'' - y'$. Integrating over x and y as in reconstruction, the total shift is

$$\begin{aligned} x'' - x' &= -\frac{|\boldsymbol{r} - \boldsymbol{r'}|x'z'z}{r^3} \\ &\approx -\frac{x'z'}{z} \end{aligned} \tag{2.17}$$

which represents a shift proportional to lateral distance from the optical axis and distance along the axis from the object origin. The shift is away from the axis for $z'' < 0$, towards the axis for $z'' > 0$, and largest at the cuvette walls, where it accounts for a 6% change in lateral position.

The calculated distortions are used to find the object position $\boldsymbol{r''}$ from the focal position $\boldsymbol{r'}$. These corrections have been verified for holograms of a cuvette with marked walls and holograms of a square grid, as described in section 2.6.

2.3.3 Reference Phase

The reference wave emerging from the GRIN lens assembly is nearly free of aberration and its phase can be approximated by $\phi_r(\boldsymbol{r}) \approx k|\boldsymbol{r} - \boldsymbol{r}_f|$. However, when the sample is present, several interfaces refract the reference before it strikes the sensor (Figure 2.13). The effects of refraction must be accounted for in subtracting the reference phase from the normalized hologram; otherwise the reconstructed object space would be improperly scaled and image quality would be degraded.

Three materials are involved: water, quartz and air, with refractive indices of 1.333,

1.458, 1.000 at 635 nm and depths of 5, 2.5 and 39 mm. Under the paraxial approximation, the lateral displacement in each medium can be written in terms of the refractive indices n_i and axial depths ℓ_i:

$$\begin{aligned}
\rho_1 &\approx \frac{n_2 n_3 \ell_1}{n_2 n_3 \ell_1 + n_1 n_3 \ell_2 + n_1 n_2 \ell_3} \rho \equiv \zeta_1 \rho \\
\rho_2 &\approx \frac{n_1 n_3 \ell_2}{n_2 n_3 \ell_1 + n_1 n_3 \ell_2 + n_1 n_2 \ell_3} \rho \equiv \zeta_2 \rho \\
\rho_3 &\approx \frac{n_1 n_2 \ell_3}{n_2 n_3 \ell_1 + n_1 n_3 \ell_2 + n_1 n_2 \ell_3} \rho \equiv \zeta_3 \rho
\end{aligned} \tag{2.18}$$

The optical path length from the source to the sensor through the interfaces determines the phase:

$$\phi_r(\rho) = k_1 \sqrt{\zeta_1^2 \rho^2 + \ell_1^2} + k_2 \sqrt{\zeta_2^2 \rho^2 + \ell_2^2} + k_3 \sqrt{\zeta_3^2 \rho^2 + \ell_3^2} \tag{2.19}$$

where k_i are the wavenumbers in the three media. Expanding as a Taylor series, the phase can be written to fourth order in ρ:

$$\phi_r(\rho) \approx \sum_{j=1}^{3} k_j \ell_j + \frac{\rho^2}{2} \frac{k_j \zeta_j^2}{\ell_j} - \frac{\rho^4}{8} \frac{k_j \zeta_j^4}{\ell_j^3} \tag{2.20}$$

A similar expression is used to correct the phase from the focal plane of the reconstruction to the sensor; for objects in these planes, the scattered wave only passes through one of the quartz walls of the cuvette, and the axial depth in water depends on the location of the plane itself. The phase on the sensor for an object on the beam axis, located a distance ℓ_1' from the cuvette wall towards the sensor, can be written to fourth order in ρ:

$$\phi_s(\rho) \approx \sum_{j=1}^{3} k_j \ell_j' + \frac{\rho^2}{2} \frac{k_j \zeta_j^2}{\ell_j'} - \frac{\rho^4}{8} \frac{k_j \zeta_j^4}{\ell_j'^3} \tag{2.21}$$

where $\ell_2' = \ell_2/2$ and $\ell_3' = \ell_3$. For each reconstructed plane, this expression is used to correct for defocus and primary spherical aberration for in focus objects. The correction leaves some aberration for out of focus objects and introduces some curvature of field.

In principle the curvature could be taken into account after reconstruction to determine the exact location of the scatterer along the optical axis. In our setup, the relatively low numerical aperture results in shifts due to curvature of only a few micron, which is smaller than the uncertainty in location due to the focal depth of 40 μm, and so shifts due to curvature caused by refraction are ignored.

2.4 Hardware performance

2.4.1 Imaging

An example normalized hologram is shown in Figure 2.14; in this and all other holographic images, whiter pixels indicate higher intensities. Holographic reconstructions yield high contrast images of cells as small as bacteria, across a field of view which reaches 3 mm in width at the distal cuvette wall, as shown in Figures 2.15 and 2.16. The resolution is 1.7 μm in x, 2.3 μm in y, and 41.5 μm in z, as measured by the full width at half maximum intensity of reconstructed holograms of 1.1 μm diameter polystyrene beads, allowing individuals to be separated at cell densities up to the limit inherent to inline holography. The region imaged with DIHM measures hundreds of microbial body lengths per side, allowing spatial gradients in density to be measured.

Reconstructions were made of holograms of a 200 μm square grid, printed out of photoresist on the inside of a cuvette otherwise similar to those used for ecological experiments. These were used to verify the calculated pixel scale and the corrections for distortion, both to better than 1%.

2.4.2 Boundary conditions

The temperature at the feedback thermistor was constant within $\pm 0.004\,\mathrm{C}$ for as long as 90 days in each microscope. LED intensity, when set to a constant level, was stable to $\pm 0.3\%$ over 90 days.

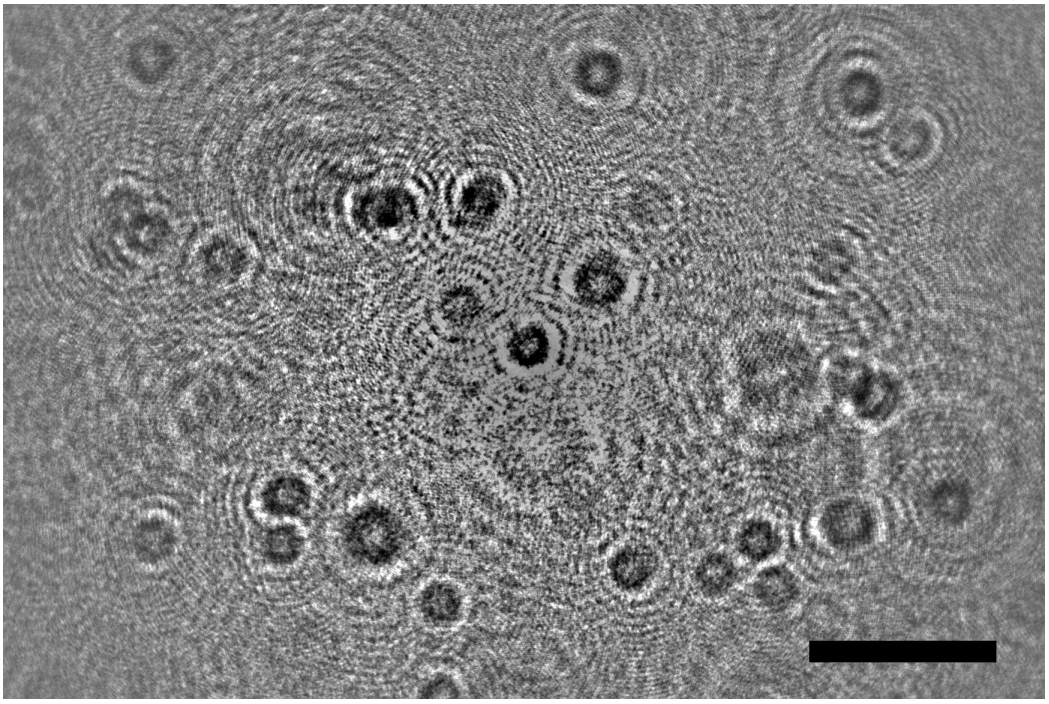

Figure 2.14: Example hologram - Normalized hologram of *T. thermophila* and *C. reinhardtii*. In this and all other holographic images, whiter pixels indicate higher intensities. Scale bar is 4 mm.

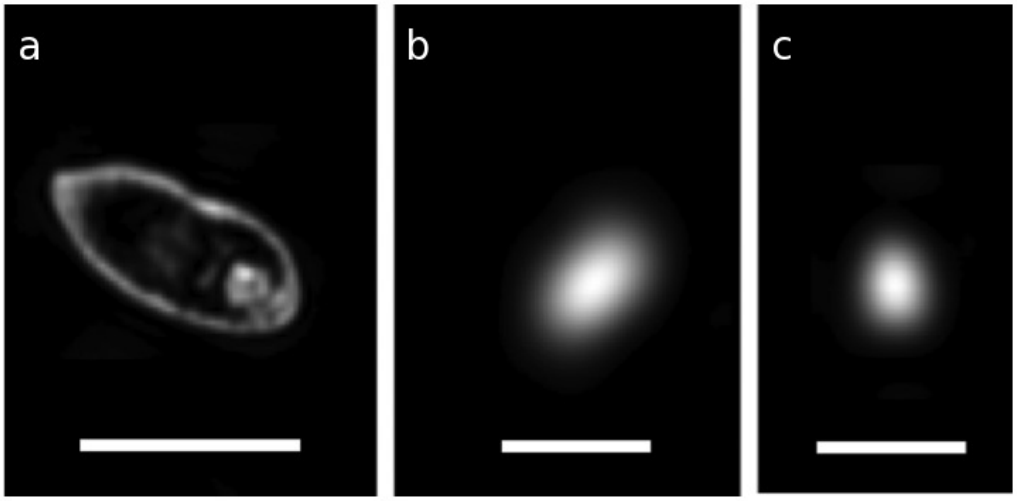

Figure 2.15: Reconstruction detail - (a) *Tetrahymena thermophila*, scale bar 40 μm, (b) *C. reinhardtii*, scale bar 5 μm, (c) *Escherichia coli*, scale bar 5 μm. Contrasts adjusted to show detail; the signal in (b) is 40 times brighter than in (c).

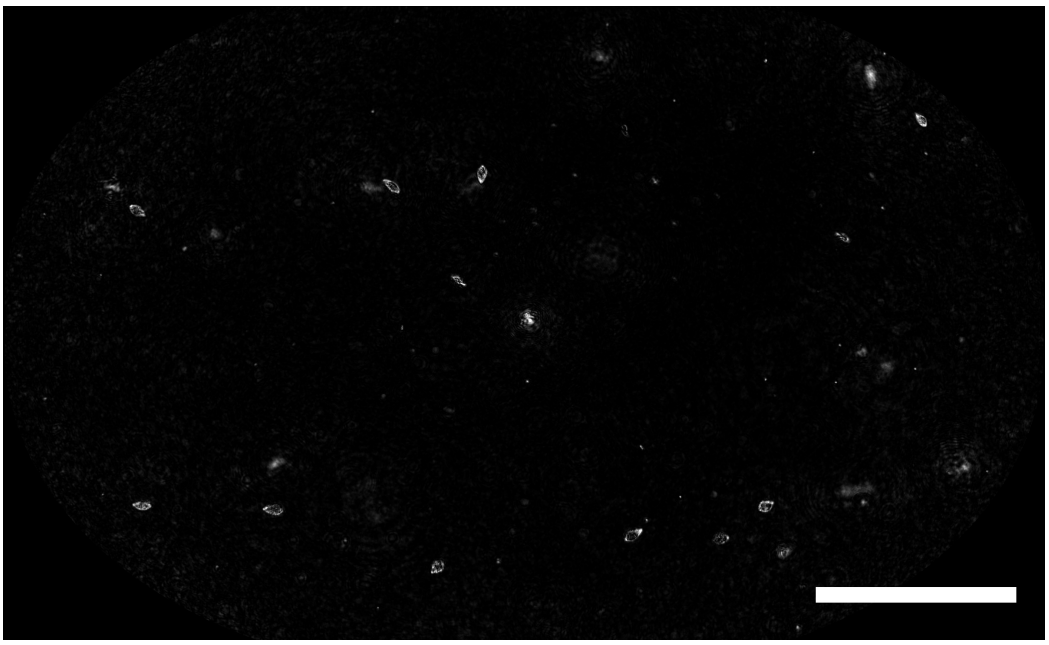

Figure 2.16: Reconstructed field of view - Plane reconstructed from hologram in Figure 2.14, located near the distal cuvette wall. Scale bar is 500 μm.

2.5 Image analysis

With 10 microscopes, hundreds of holograms per day, 90 day experiments, and tens to hundreds of organisms per hologram, the amount of data acquired during a typical ecological experiment necessitates automatic image analysis to identify and describe all individuals present in the reconstructed volume. Individuals are well separated from background up to a limiting density, suggesting that a simple intensity threshold can be used to identify organisms with high fidelity. Since only morphological data are available, analysis of two species holograms is more difficult and can only succeed when the two species are sufficiently different in size or shape.

Few schemes for automated image analysis for digital holograms have been proposed. This may be due to two difficulties inherent to the technique: reconstructed intensities have strong spatial dependence, and out of focus light can resemble in focus objects. Sheng et al. used a segmentation procedure with a spatially varying intensity threshold, determined by estimating the local signal to noise ratio(20). To estimate the signal to noise ratio in a volume V the object density must be higher than $1/V$ so that several objects are present on average. This technique is therefore not applicable to population dynamics measurements, in which the cell density is expected to vary by orders of magnitude. Moon and Javidi employed a method of randomly sampling continuous segments of complex amplitudes from reconstructions of extended objects, and used statistical tests to distinguish two species(17). The technique was shown to distinguish two individuals of very similar filamentous morphologies with an error rate of about 13%. The technique was not tested on populations of organisms, nor was it clear that the technique could be adapted to smaller objects such as bacteria or algae. Both of these techniques were applied to setups with plane wave illumination and a microscope objective for fringe magnification. To our knowledge no analysis method has been demonstrated for the lensless setup. We propose a novel technique involving

normalization for intensity variation followed by iterative subtraction of the brightest signals.

2.5.1 Intensity variation

The reconstructed intensity of an object depends on its location for a number of reasons: the incident reference intensity varies some 10 fold in the imaged region, the scattering efficiency varies with angle, and aberrations introduced by the approximation (2.7) vary with object location. For identical objects, the reconstructed intensity varies some 80 fold over the imaged region in our setup. To simplify the image analysis, reconstructed intensities are normalized. This is accomplished in two steps - first by correcting for variation in the reference intensity analytically, then normalizing the remaining variation empirically.

2.5.2 Reference beam intensity

The intensity of the reference beam at the sensor is measured in each experiment. The incident reference intensity for a reconstructed object can be estimated by projecting from the source through the object location to the sensor, accounting for refraction, as shown in Figure 2.17. Let (x', y', z') be the coordinates of the reconstructed point from the source; the point on the sensor which intersects the ray from the source to (x', y', z') is given by

$$\begin{aligned} x &= \left(\ell_1 + \frac{n_1}{n_2}\ell_2 + \frac{n_1}{n_3}\ell_3\right)\frac{x'}{z' + (\frac{n_1}{n_2} - 1)\frac{\ell_2}{2}} \\ y &= \left(\ell_1 + \frac{n_1}{n_2}\ell_2 + \frac{n_1}{n_3}\ell_3\right)\frac{y'}{z' + (\frac{n_1}{n_2} - 1)\frac{\ell_2}{2}} \end{aligned} \tag{2.22}$$

The reference beam's intensity also varies along the optical axis. Let $I(x', y', z')$ be the reconstructed intensity at (x', y', z') and $I_r(x, y, z_{sensor})$ be the intensity of the reference at the point on the sensor projected using (2.22); the intensity of the reference

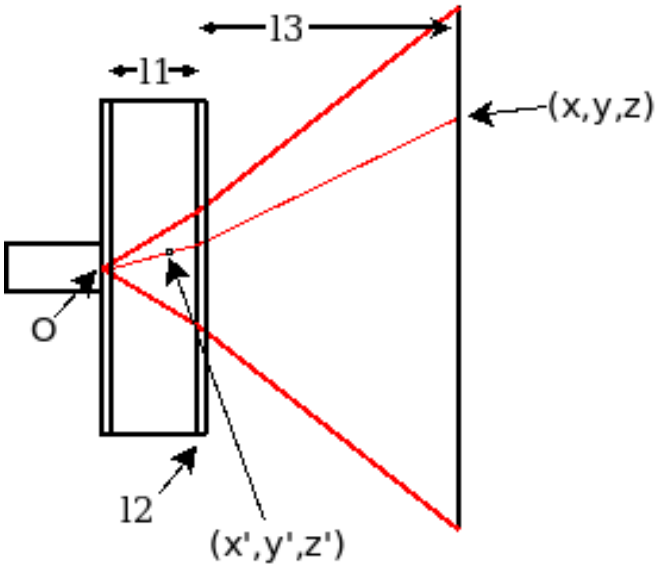

Figure 2.17: Schematic of refraction of scattered wave - a scatterer is located at (x', y', z'), and the ray from the source at the origin O through this point is projected to the sensor at (x, y, z). The depths of water, glass and air are labeled ℓ_1,ℓ_2 and ℓ_3.

wave at the reconstructed point is given by

$$I_r(x', y', z') = I_r(x, y, z_{sensor}) \frac{z_{eff}^2}{\left(z' + \left(\frac{n_1}{n_2} - 1\right)\frac{\ell_2}{2}\right)^2} \tag{2.23}$$

where z_{eff} is the optical path length along the optical axis. A reconstructed intensity normalized for reference beam intensity is calculated for each reconstructed point:

$$\tilde{I}(x', y', z') = \left(z' + \left(\frac{n_1}{n_2} - 1\right)\frac{\ell_2}{2}\right)^2 \frac{I(x', y', z')}{I_r(x, y, z_{sensor})} \tag{2.24}$$

2.5.3 Other factors affecting intensity

The remaining variation in reconstructed intensity with position was considered empirically. 30 holograms from an experiment with *Chlamydomonas reinhardtii* in Sager-Granick medium at a density of $\sim 4.3 \times 10^4$ /mL were reconstructed, and reconstructions were normalized by reference intensity as described above. Several rounds of reconstruc-

tion were employed, using a decreasing series of intensity thresholds for global segmentation. After each segmentation, signals above the current threshold were subtracted in the object's focal plane (see 2.5.5) so that the lower threshold could be applied at subsequent reconstructions without isolating the already analyzed object (see section 2.5.4 for more details of signal subtraction). For each of the 4315 identified blobs, the maximum intensity was measured, as this characteristic was robust to segmentation threshold and the details of signal subtraction. Since there was some 20 fold spatial dependence in maximum intensity, a function was fit to the logarithm of I_{max}:

$$f(x,y,z) = c_1 + c_2|x| + c_3x^2 + c_4|y| + c_5y^2 + c_6z + c_7z^2 + c_8z\sqrt{x^2+y^2} \qquad (2.25)$$

by linear least squares (see Table 2.1).

coefficient	value	standard error
c_1	18.1	0.02
c_2	3.09e-4	0.70e-4
c_3	-3.34e-6	0.09e-6
c_4	4.12e-4	1.03e-4
c_5	-4.91e-6	0.17e-6
c_6	-2.58e-4	0.12e-4
c_7	-7.32e-8	0.52e-8
c_8	1.21e-6	0.04e-6

Table 2.1: Coefficients for intensity normalization - coefficients from equation 2.25 empirically fit to I_{max}. RMS of residuals is 0.346

The fit of (2.25) is used to normalize intensities in all analyses, so that on average I_{max} does not exhibit spatial dependence and image analysis is simplified. In regions where the normalization multiplier reaches large values, the signal to noise ratio is proportionally lower. The signal to noise ratio also depends on the cell density of the sample, since the predominant noise comes from out of focus light scattered from neighboring objects. Thus higher cell densities can be measured in regions with smaller normalization factor; in practice, most analyses are performed by restricting the imaged

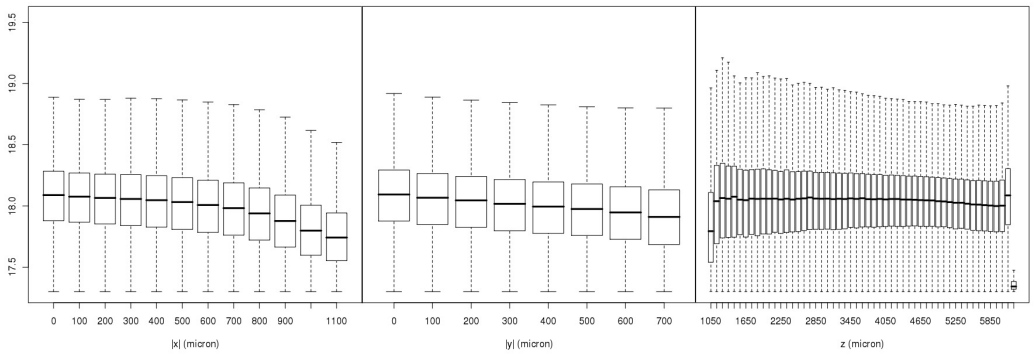

Figure 2.18: Spatial variation of $\log(I_{max})$ after normalization, as functions of x, y and z, respectively. Data taken from an experiment with *C. reinhardtii*. Boxes show upper and lower quartiles, whiskers show extrema and bars show medians for 100 μm bins.

volume to regions where the normalization factor is less than a threshold value. This value is chosen as the largest multiplier which allows analysis of holograms at high cell densities ($\sim 1 \times 10^5$ cells/cm^3) without significant contribution (<5%) from counts due to background.

2.5.4 Signal subtraction

Reconstructed intensity oscillates strongly as a function of distance from focus for a given object, so that applying an intensity threshold to a single object can result in several disconnected blobs, only one of which corresponds to the actual object in the focal plane. This is especially problematic when out of focus light from two nearby objects interferes constructively to form small, bright blobs, as seen in Figure 2.19. Objects of heterogeneous intensities present a difficulty for automatic analysis; very bright objects give rise to out of focus light in planes over 1 mm away which can pass the intensity threshold as blobs resembling focused objects in the same focal plane. Because the intensity has strong spatial dependence, heterogeneity is always present, even for a population of identical particles. When multiple species of different sizes or scattering efficiencies are present, the problem becomes even harder.

Our solution to this problem is to start the analysis with an intensity threshold

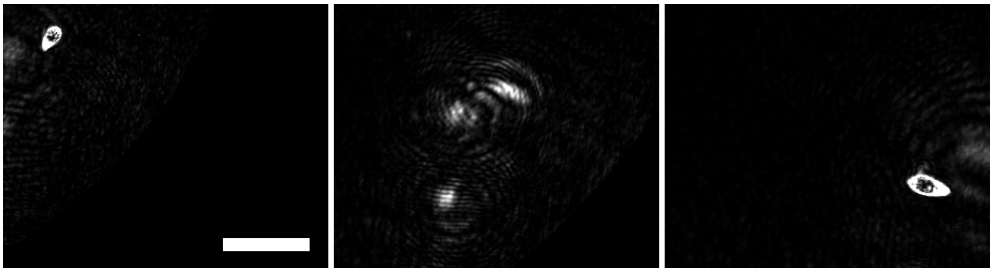

Figure 2.19: Interference between nearby objects - in the first and last panel, two *T. thermophila* reconstruct 2 mm apart in z. The central panel shows the interference of out of focus light from both cells in a plane reconstructed halfway between them. The small, bright fringes cannot be distinguished from smaller cells such as *C. reinhardtii*. This problem is solved by subtracting bright signal as described in section 2.5.4. Scale bar is 100 μm.

high enough to pass only true, focused signal from the brightest objects. For each blob passing the intensity threshold, a filter is applied which ensures that the blob contains enough voxels for subsequent analysis. The focal plane is determined (as described in section 2.5.5) for blobs passing the size filter, and a final filter is applied in the focal plane, so that most of the signal from the object is set to zero intensity. The complex values of the filtered reconstruction are propagated back to the hologram plane, and this filtered hologram is used for subsequent analysis. Once all planes have been analyzed at the first intensity threshold, the process is repeated at a lower intensity threshold. In this way, the out of focus light from the brightest objects is removed before dimmer signals are considered. Example images produced during this process are presented in Figure 2.20.

2.5.5 Focal plane determination

It is crucial to accurately determine the focal plane before subtracting signal to avoid attenuating signal originating from nearby objects. Every pixel which is filtered contains some signal from all other focal planes, and the focal plane is by definition the plane in which the fewest pixels can be filtered while removing most of the intense signal. Automatic determination of the focal plane is not trivial, and various methods

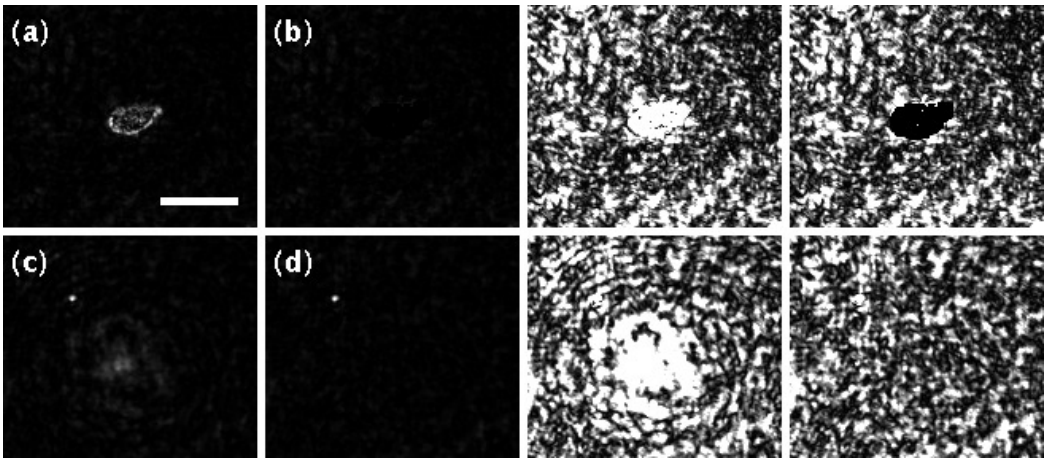

Figure 2.20: Detail of signal subtraction - (a) reconstructed *T. thermophila* in plane of focus, (b) same region as (a) but reconstructed after signal subtraction, (c) reconstructed plane 1 mm from (a), showing in focus *C. reinhardtii* and out of focus light from *T. thermophila*, (d) region shown in (c), but reconstructed after subtraction. The four panels on the right are duplicated from (a)-(d) but displayed with much higher contrast to show detail in dimmer signals. Scale bar is 50 μm.

have been proposed for digital holography(4, 10, 15, 22, 27). These methods all dealt with images from Fresnel-type setups, using plane wave illumination and microscope objectives for fringe magnification, and probably for this reason were not found to be useful for our setup. Rather, a gradient based method is used: for each plane z in which blob B_i is represented, the following sum is calculated over all voxels passing the current threshold:

$$L_z(B_i) = \sum_{\{x,y|(x,y,z)\in B_i\}} \frac{1}{\Delta_x}\big(-A(x-1,y,z) + 2A(x,y,z) - A(x+1,y,z)\big) + \frac{1}{\Delta_y}\big(-A(x,y-1,z) + 2A(x,y,z) - A(x,y+1,z)\big) \qquad (2.26)$$

where Δ_x and Δ_y are the lateral dimensions of the reconstructed voxel and $A(x,y,z) = \sqrt{I(x,y,z)}$ is the unnormalized amplitude of the reconstruction at voxel (x,y,z). The focal plane is chosen as the plane z which maximizes L_z subject to a constraint on the number of voxels per plane, imposed to avoid spurious maxima. The calculation of L_z

was superior to other gradient based methods such as the Sobel filter, and calculations based on amplitudes outperformed those based on intensities. The scheme described found the focal plane of over 100 *C. reinhardtii* and *T. thermophila* to within the sampling interval of 17 μm.

2.6 Software performance

The counts within the imaged region should be proportional to the average density of the entire sample, assuming the fluid is well mixed and there is no interaction with the walls. The constant of proportionality is the effective volume of the measurement. The calculated volume of the imaged region was 6.86 mm^3 for analysis of single species. The imaged volume was calibrated by imaging suspensions of 5.2 μm diameter polystyrene beads (Spherotech) at densities also measured by flow cytometry. Three densities were used in all ten microscopes, revealing variability in the effective volume of 4% ($6.76 \pm 0.13\,mm^3$). A single microscope was used to measure four bead densities in triplicate, yielding an effective volume of $6.65 \pm 0.14\,mm^3$. Data are presented in Figure 2.21 and Table 2.2. Initial attempts to calibrate directly with algae failed, presumably due to rapid establishment of strong spatial heterogeneity within the cuvette. The difference between the calculated volume and the measured volume is likely due to boundary effects, in that a cell with its brightest voxels just outside the imaged volume and only one or a few bright voxels lying inside the imaged volume may by counted as background. The geometry of the analyzed volume is shown in Figure 2.22: it is the intersection of the pyramid representing the projection of the image sensor back to the reference beam focus and the cone determined by the normalization threshold which lies between the cuvette walls.

At densities higher than the 10^5 /mL limit, analysis can still be performed in regions with high signal to noise ratio - namely, the lateral center of the reference beam. By

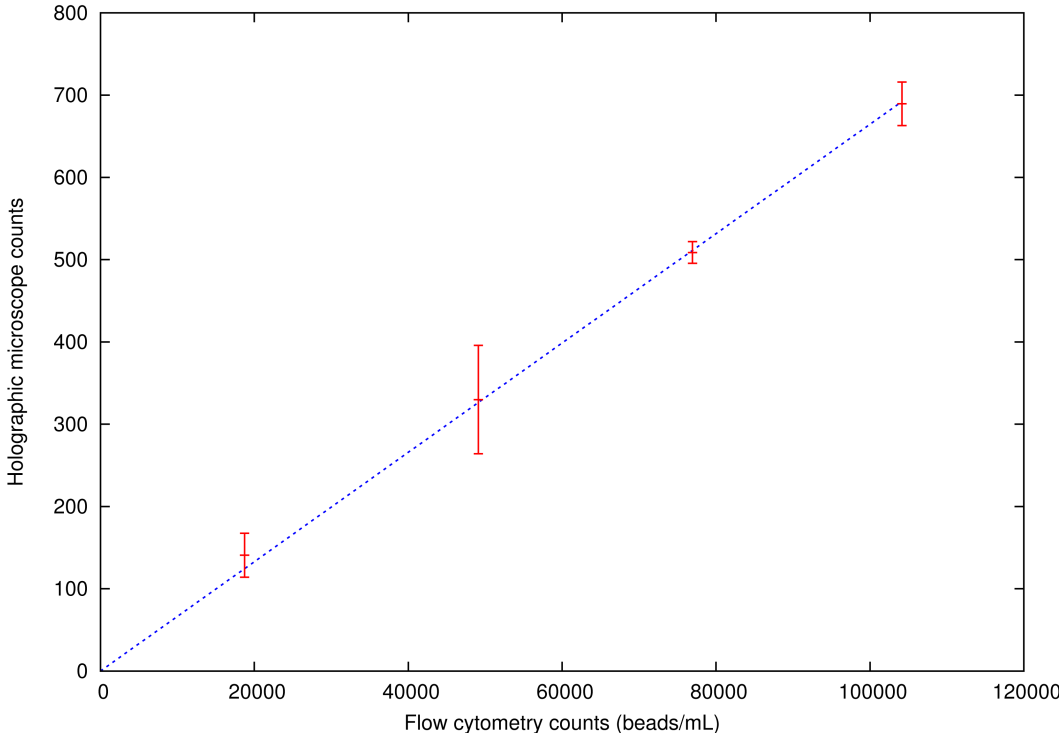

Figure 2.21: Imaged volume of DIH microscopy calibrated by flow cytometry with triplicate measurements of bead densities. The line shows the best least squares linear fit with zero intercept, giving $V_{eff} = 6.65 \pm 0.14\,\mathrm{mm}^3$, $R^2 = 0.9995$. Error bars are ± 2 standard errors.

restricting the analysis to the $\sim$1 μL closest to the beam axis, accurate counts can be extracted up to a cell density of $\sim 5 \times 10^5$ /mL for *C. reinhardtii*.

The method of subtracting signal from bright objects before considering dimmer ones was found to increase the maximum cell density threshold by at least a factor 2 for algae. For two species experiments with *C. reinhardtii* and *T. thermophila*, out of focus signal from large ciliates which reconstructed either outside of or just at the periphery of the reconstructed volume was not possible to subtract properly and interfered with analysis at dimmer thresholds. By removing a portion of the periphery from consideration and therefore reducing the effective volume to 5.5 mm^3, this problem was avoided.

The spatial variation in intensity remaining after normalization is shown in Figure

system	V_{eff} (mm^3)	standard error (mm^3)
1	6.67	0.38
2	6.68	0.04
3	6.73	0.02
4	6.77	0.23
5	6.89	0.09
6	6.85	0.06
7	6.49	0.05
8	6.89	0.10
9	6.87	0.05
10	6.74	0.09

Table 2.2: DIHM effective volumes - effective volume of each DIH microscope from measuring suspensions of beads at three densities between 9,000 cm^{-3} and 45,000 cm^{-3}, independently verified with flow cytometry. The mean volume is $6.76 \pm 0.13\,mm^3$.

2.18 for an experiment with *C. reinhardtii*. Signal subtraction is not necessary for populations of *C. reinhardtii* below cell densities of $10^5\,cm^{-3}$, rather a single intensity threshold suffices. The distribution of maximum intensity per blob from an experiment with *C. reinhardtii* is shown in Figure 2.23.

Several hundred rounds of hologram filtering can be performed without noticeable attenuation of signal for unfiltered objects. When the current implementation is applied to mixtures of *C. reinhardtii* and *T. thermophila*, some dim objects which are neither species remain after signal subtraction. Some of these may be cell parts brought into the imaged volume by convection currents - these are often found in analysis of ecosystems containing *T. thermophila* via flow cytometry. Some of the dim signal is certainly due to scattering from large, bright objects which is not subtracted. Objects which are large compared to the resolution of the microscope are often surrounded by a dim, diffuse ring of intensity. These "halos" are likely due to artifacts resulting from the small numerical aperture of the microscope. They are not subtracted due to their large size and separation from the focused object. Instead, they appear as a background signal in the analysis. Classification of blobs by lateral size and maximum intensity into classes representing background, *C. reinhardtii* and *T. thermophila* is shown in

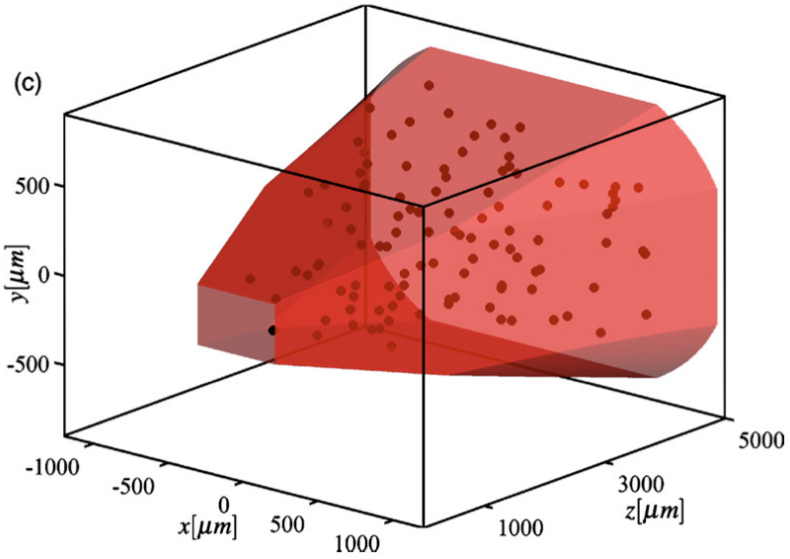

Figure 2.22: Geometry of analyzed regions - three dimensional view of the analyzed region shown in red, with the locations of 110 identified algae plotted as points.

Figure 2.24. The classification model is 3 Gaussian distributions with variable volumes and covariance matrices and was fit using the MCLUST package for R (`http://www.stat.washington.edu/mclust/`)(5, 6). At densities of *C. reinhardtii* below $10^5\,\mathrm{cm}^{-3}$, the classification error was less than 5%.

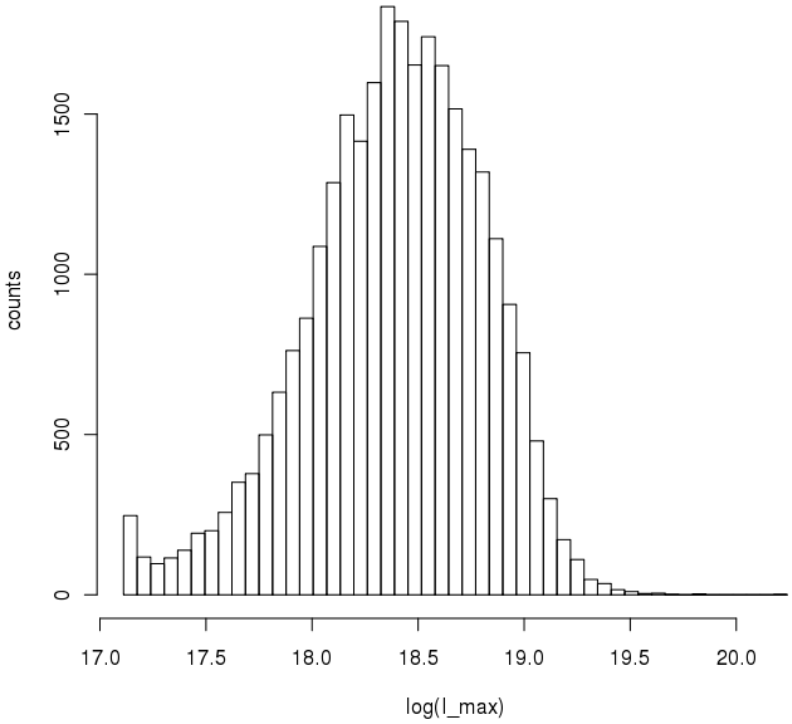

Figure 2.23: Histogram of $\log(I_{max})$ after normalization, from an experiment with *C. reinhardtii* at densities below the threshold.

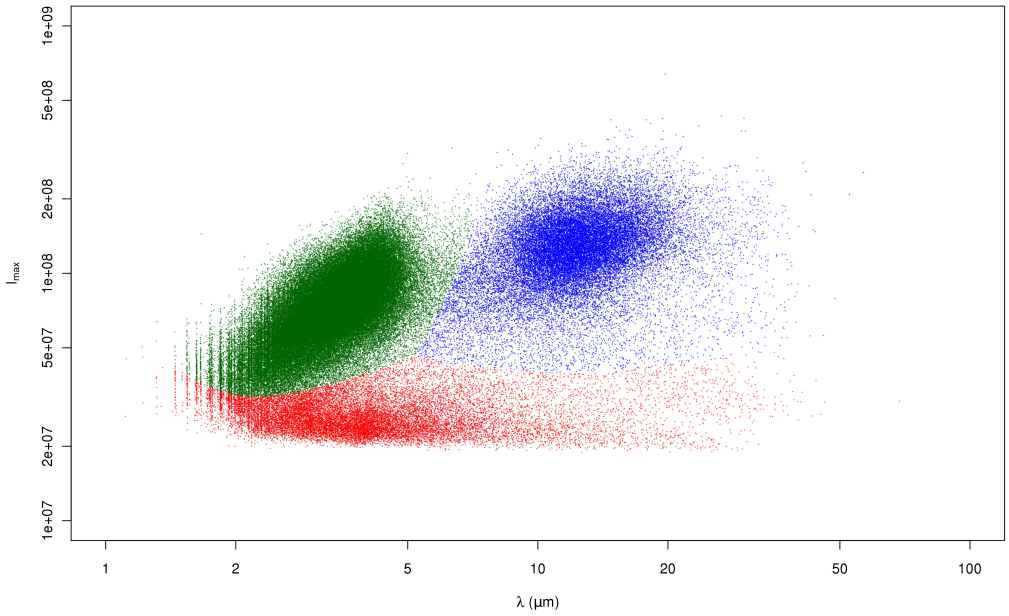

Figure 2.24: Scatter plot of I_{max} vs. lateral size λ from an experiment with *C. reinhardtii* and *T. thermophila*. The background class is plotted in red, the *C. reinhardtii* class in green and the *T. thermophila* class in blue.

Bibliography

[1] Max Born and Emil Wolf. *Principles of optics: Electromagnetic theory of propagation, interference and diffraction of light*. Cambridge University Press, Cambridge, U.K., seventh edition, 1999. 14, 30, 35

[2] J. M. Cowley and D. J. Walker. Reconstruction from in-line holograms by digital processing. *Ultramicroscopy*, 6:71–75, 1981. 15

[3] Etienne Cuche, Patrick Poscio, and Christian D. Depeursinge. Optical tomography at the microscopic scale by means of a numerical low-coherence holographic technique. In Hans-Jochen Foth, Renato Marchesini, and Halina Podbielska, editors, *Proceedings of the SPIE - Optical and Imaging Techniques for Biomonitoring II*, volume 2927, pages 61–66, 1996. 15

[4] Frank Dubois, Cédric Schockaert, Natcaha Callens, and Catherine Yourassowsky. Focus plane detection criteria in digital holography microscopy by amplitude analysis. *Optics Express*, 14:5895–5908, 2006. 47

[5] C. Fraley and A. E. Raftery. Model-based clustering, discriminant analysis and density estimation. *Journal of the American Statistical Association*, 97:611–631, 2002. 51

[6] C. Fraley and A. E. Raftery. MCLUST version 3 for R: Normal mixture modeling and model-based clustering. Technical Report 504, University of Washington, Department of Statistics, 2006 (revised 2009). 51

[7] Dennis Gabor. A new microscopic principle. *Nature*, 161:777–778, 1948. 13, 14

[8] Dennis Gabor. Microscopy by reconstructed wave-fronts. *Proceedings of the Royal Society of London. Series A, Mathematical and Physical Sciences*, 197:454–487, 1949. 13

[9] David Garber. Digital holography using a laser pointer and consumer digital camera. Technical report, Johns Hopkins University, Baltimore, MD, 2004. Also available as
`http://www.me.jhu.edu/lefd/shc/LPholo/lphindex.htm`. 15, 16

[10] John Gillespie and R. A. King. The use of self-entropy as a focus measure in digital holography. *Pattern Recognition Letters*, 9:19–25, 1989. 47

[11] J. W. Goodman and R. W. Lawrence. Digital image formation from electronically detected holograms. *Applied Physics Letters*, 11:77–79, 1967. 15

[12] Mats Gustafsson, Mikael Sebesta, Bengt Bengtsson, Sven-Göran Pettersson, Peter Egelberg, and Thomas Lenart. High resolution digital transmission microscopy - a Fourier holography approach. *Optics and Lasers in Engineering*, 41:553–563, 2004. 13, 16

[13] M. E. Haine and T. Mulvey. The formation of the diffraction image with electrongs in the Gabor diffraction microscope. *Journal of the Optical Society of America*, 42:763–769, 1952. 14

[14] Paul Horowitz and Winfield Hill. *The art of electronics*. Cambridge University Press, Cambridge, U.K., second edition, 1989. 19

[15] Michael Liebling and Michael Unser. Autofocus for digital Fresnel holograms by use of a Fresnelet-sparsity criterion. *Journal of the Optical Society of America A*, 21:2424–2430, 2004. 47

[16] J. D. Maynard, E. G. Williams, and Y. Lee. Nearfield acoustic holography: I. Theory of generalized holography and the development of NAH. *Journal of the Acoustical Society of America*, 78:1395–1413, 1985. 15

[17] Inkyu Moon and Bahram Javidi. Shape tolerant three-dimensional recognition of biological microorganisms using digital holography. *Optics Express*, 13:9612–9622, 2005. 41

[18] Lord Rayleigh. On the passage of waves through apertures in plane screens, and allied problems. *Philosophical Magazine*, 43:259–272, 1897. 30

[19] U. Schnars and W. Jüptner. Direct recording of holograms by a CCD target and numerical reconstruction. *Applied Optics*, 33:179–181, 1994. 15

[20] Jian Sheng, Edwin Malkiel, and Joseph Katz. Single beam two-views holographic particle image velocimetry. *Applied Optics*, 42:235–250, 2003. 41

[21] Jian Sheng, Edwin Malkiel, and Joseph Katz. Digital holographic microscope for measuring three-dimensional particle distributions and motions. *Applied Optics*, 45:3893–3901, 2006. 15, 16

[22] Jian Sheng, Edwin Malkiel, Joseph Katz, Jason Adolf, Robert Belas, and Allen R. Place. Digital holographic microscopy reveals prey-induced changes in swimming behavior of predatory dinoflagellates. *Proceedings of the National Academy of Sciences of the United States of America*, 104:17512–17517, 2007. 47

[23] Arnold Sommerfeld. *Optics*. Academic Press, New York, NY, 1954. 30

[24] Miklós Tegze and Gyula Falgel. X-ray holography with atomic resolution. *Nature*, 380:49–51, 1996. 14

[25] Joseph T. Verdeyen. *Laser electronics*. Prentice Hall, Englewood Cliffs, NJ, third edition, 1994. 17

[26] Wenbo Xu, M. H. Jericho, I. A. Meinertzhagen, and H. J. Kreuzer. Digital in-line holography for biological applications. *Proceedings of the National Academy of Sciences of the United States of America*, 98:11301–11305, 2001. 13, 15, 16

[27] Yan Yang, Bo-seon Kang, and Yeon-jun Choo. Application of the correlation coefficient method for determination of the focal plane to digital particle holography. *Applied Optics*, 47:817–824, 2008. 47

Chapter 3

Model ecosystems

This chapter describes the ecosystems studied in this thesis. These are composed of one or two species and liquid media maintained in well defined boundary conditions. Protocols followed before and after hologram acquisitions in the microscopes are described.

3.1 Requirements for a model closed ecosystem

The technique of DIHM is necessarily limited to distinguishing organisms of different species by morphology, since it does not employ fluorescence. Early in the development of the technique we decided to focus on simple ecosystems composed of a single species. Since the sample volume is not vigorously mixed by stirring, we sought a swimming microbial species which could persist for long times in a closed aquatic environment. We attempted measurements with the cyanobacteria *Synechococcus elongatus* and the green algae *Chlamydomonas reinhardtii*. Both species are photosynthetic, well characterized, genetically tractable, capable of growth in defined media and small enough ($\sim$5 μm diameter) for simple analysis based on intensity. Both of these were amenable to measurement by DIHM. However, the cyanobacteria are motilite through gliding along solid surfaces, so that cells were observed only on the cuvette walls and not in the fluid bulk. Thus we chose *C. reinhardtii* as our first model organism.

For two species ecosystems, we sought a second species of motile microbe which could coexist for long times with *C. reinhardtii*. Kawabata et al. used *Tetrahymena thermophila* in conjunction with the larger motile algae, *Euglena gracilis*, and the swimming bacteria *Eschirichia coli* for long term ecosystem experiments(12). The medium found to be compatible with these species for long term experiments was 1/2× Taub #36 supplemented with proteose peptone(12, 23). Hekstra replaced *E. gracilis* with *C. reinhardtii* for the advantages mentioned above as well as its shorter doubling time (5-6 hours)(9). Preliminary experiments were conducted showing long term coexistence of *T. thermophila* and *C. reinhardtii*(9), leading us to select *T. thermophila* as a second species.

3.2 *Chlamydomonas reinhardtii*

C. reinhardtii is a single-celled, eukaryotic green algae commonly found in soil and fresh-water (Figure 3.1). The organism is roughly spherical, 5-10 μm in diameter, and swims by beating its two flagella, reaching sustained speeds as fast as 200 μm/s(18). It can grow photoautotrophically by fixing carbon dioxide or in total darkness when supplemented with acetate as a carbon source, with a doubling time as short as 5 hours(8). Its nuclear, mitochondrial and chloroplast genomes have been sequenced; the nuclear genome is 121 Mb, containing some 15,000 genes(3, 4, 5, 15, 16).

The species has two mating types, called mt+ and mt-, which can fuse sexually to form a diploid. The diploid cell can then divide meiotically to form haploid offspring, or in rare cases divides mitotically to form a diploid cell which grows vegetatively(8). In the absence of the opposite mating type, the organisms exist as haploids which grow vegetatively. Prior to mating, *C. reinhardtii* cells differentiate into a state known as the gamete, which can then agglutinate and fuse with the opposite mating type(8). Gametogenesis requires conditions of nitrogen deprivation (<375 μM ammonium ions)

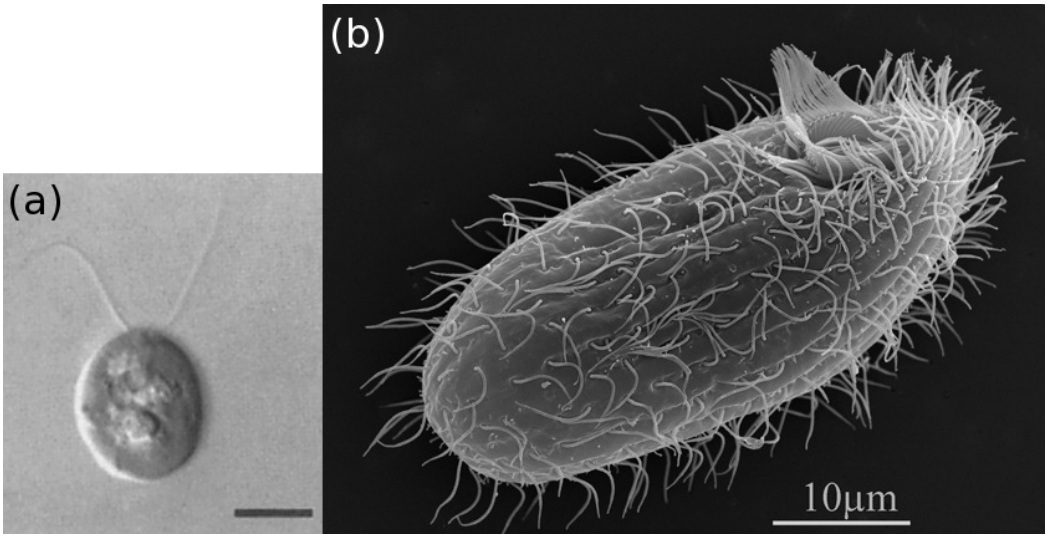

Figure 3.1: Images of *C. reinhardtii* and *T. thermophila* - (a) differential interference contrast image of *C. reinhardtii*, taken from Sanders et al. 1994(21), scale bar 5 μm, (b) scanning electron micrograph of *T. thermophila* taken by Aswati Subramaniam, scale bar 10 μm.

and does not occur in the dark(20), but does not require the presence of both mating types(8). Once differentiated, cells remain in the gametic state until either illumination in removed or nitrogen is added to the medium, and can survive nitrogen starvation for several weeks(14). To our knowledge, determining the gametic state of a cell requires transcriptional or biochemical analysis, or investigation of fine structure, none of which we attempted. However, in many of our long term experiments, especially those initiated with media containing low levels of nitrogen, many *C. reinhardtii* cells were probably in a gamete-like state.

C. reinhardtii has a sophisticated system of responses to light. At low intensities cells swim towards the origin of the light and at high intensities swim away from it, by modulating their direction rather than their swimming speed(7), although the rate of phototaxis for a population depends on the culture conditions, the age of the culture and the phase of the circadian cycle(6, 22).

A high proportion of cells (typically 10-20% but sometimes as much as 80%) were

observed to be in doublet or quadruplet states when cultured in the standard growth medium TAP - these are groups of two or four cells within the same cell wall, distinct from the "palmelloid" state described in the literature(8), which was rarely observed in any media. Because these doublets and quadruplets displayed reduced motility, we switched culture medium to Sager-Granick medium, modified to enhance motility(19), as described in section 3.6.1. This medium was found to consistently yield high proportions of swimming cells in singlet form (>95%). Ecosystems which had been sealed for several months usually contained a significant number of sessile and dead cells or cell parts; the viability dye Sytox Green was useful in distinguishing live and dead cells using flow cytometry.

Populations of *C. reinhardtii* grown in TAP or Sager-Granick media with illumination reach densities around 1×10^7 /mL, or $\sim 70,000$ counts in the volume imaged by DIHM, which exceeds the optical density limit for inline holography (section 4.1). Eventually the cell density in a completely sealed ecosystem decreases, often to densities which can be imaged by DIHM, although this can take several weeks. In attempts to find a system with suitable cell densities for short term experiments, we measured population dynamics of *C. reinhardtti* in conditions of limited manganese, phosphate or nitrogen in the form of ammonium. Of these, only nitrogen concentrations at or below 25 μM were found to significantly lower the maximum density while maintaining long term survival - a 450 fold reduction from the 11.2 mM ammonium concentration of Sager-Granick medium.

3.3 *Tetrahymena thermophila*

T. thermophila is a 30-50 μm long elliptical or flaxseed shaped ciliate, found in bodies of fresh-water (Figure 3.1). It swims as fast as 1 mm/s through coordinated beating of its hundreds of cilia, and subsists through ingestion and degradation of other microbes

by phagocytosis(1, 10). Its genetic structure, like most ciliates, is complicated; the cell has two nuclei, called the macronucleus and micronucleus. The former is highly polyploid, with each of its over 100 chromosomes present in ∼45 copies, while the latter is diploid and gives rise to a new macronucleus upon conjugation(17). Conjugation occurs between distinct pairs of members of at least 7 mating types, and the mating type alleles require some 60 generations of segregation between matings(2), although conjugation of cells of the same mating type has been observed(1). The mechanism for controlling macronuclear assortment over the many generations between conjugations is not known. Due to the diversity of the macronuclear genome, it is not possible to obtain clonal populations.

T. thermophila has some convenient features for laboratory study - large populations can be grown quickly (<2 hour doubling time), and genetic techniques including DNA-mediated transformation and inducible gene expression have been developed(24). Soybean culture is typically used to propagate *T. thermophila* over long intervals, while a rich culture medium called SPP(1) is often used for rapid growth.

We found that *T. thermophila* was not viable in modified Sager-Granick medium at several concentrations of ammonium in the presence of *C. reinhardtii*. Both algae and ciliates persisted for over one month in 1/2× Taub #36 supplemented with 0.03% proteose peptone (PP), as described in section 5.1. In this medium, sealing of the ecosystem cuvettes with epoxy led to rapid extinction of *C. reinhardtii*, presumably due to lack of accessible carbon, competition with *T. thermophila* for another resource affected by gas exchange with the atmosphere, or shifts in acid-base chemistry. By supplementing this medium with acetate and Tris buffer, we achieved coexistence of *T. thermophila* and *C. reinhardtii* for ∼35 days, at which point each ecosystem exhibited extinction of *T. thermophila*. These results are presented in section 5.2.

3.4 Boundary conditions

Our conception of the ecosystem boundary conditions consists of the light and temperature profile of the cuvette walls, and the rate of gas exchange through the cuvette port. To separate extrinsic driving by the environment from intrinsic fluctuations, the system is designed so that all boundary conditions can be maintained constant with high precision. The light profile and temperature can be altered precisely in order to apply perturbations. The metal box containing the cuvette is grounded, to eradicate electrostatic fields. There are no obvious sources of strongly localized electromagnetic fields in the room housing the microscopes, so that any fields should be consistent from one system to the next. Mechanical isolation provided by foam pads dampens vibrational perturbations.

The light profile is an important variable for ecosystem dynamics, since the main route for energy transfer from the environment is almost certainly photosynthesis by algae, and because the phototactic response for algae can lead to pronounced heterogeneities of cell density. We chose bright white LEDs as the illumination source for their longevity, stability over time, and simple modulation electronics. Two different varieties of white LEDs were used, with different color spectra ("blue" for 6000 K color temperature and "red" for 3200K). The illumination spectrum was found to have strong effects on population dynamics of algae under conditions of nitrogen starvation, as shown in sections 4.3 and 5.1. To achieve a homogeneous light profile, two wide beam LEDs were used, above and below the sample, and two layers of diffusive screens were placed between each LED and the sample cuvette. The highest illuminance possible was 2400 lux with the 6000 K LEDs and 1200 lux with the 3200 K LEDs.

Temperature can have strong effects on population dynamics and behavior of microorganisms. Our microscopes incorporated independent temperature control, accurate to 20 mK and precise to 4 mK; all experiments were performed at 25 C following

the work of Hekstra and Kawabata et al.(9, 12). The temperature gradient within cuvettes filled with water held at 25 C was measured between the horizontal ends of the cuvette as 50 mK in total, or 12.5 mK/cm, although the difference from either holder to the water may be significantly greater due to the relatively low air temperature (typically 23.5 C). The temperature at the feedback thermistor does not depend on the LED power, although the water temperature in the cuvette can change by as much as 40 mK with the LED power.

Temperature gradients were sufficient to drive convection in the cuvette. The Rayleigh number for the sample at 25 C is about 18,000 K^{-1} ΔT. For the Bénard configuration of two infinite horizontal plates, the critical Rayleigh number is 1700(13), while for a closed rectangular prism like the cuvette the critical value should be somewhat higher. Thus we see that temperature differences of 0.1 K can put the system very near or beyond the instability, and we expect convection due to temperature differences between the cuvette holder and the air. Convection currents were measured using DIHM by imaging 600 nm diameter polystyrene beads as tracer particles at the highest acquisition frequency possible (0.25 Hz). The density of beads was 9×10^4 /mL. The estimated vector field is shown in Figure 3.2 and the speed profile along the optical axis is shown in Figure 3.3. The vector field was consistent with two rolls pointing down in the center of the cuvette, with speeds reaching a maximum of 20 μm/s at the cuvette center and declining to zero at the cuvette walls.

Similar convection currents were observed at different bead concentrations, mean temperatures and with LEDs on and off. Convection currents in closed ecosystems with organisms present were not measured. Convection currents have been observed to change with spatial distributions of cell density (Doeke Hekstra, unpublished results); for our purposes, we accept convection as one of many potentially complicating factors.

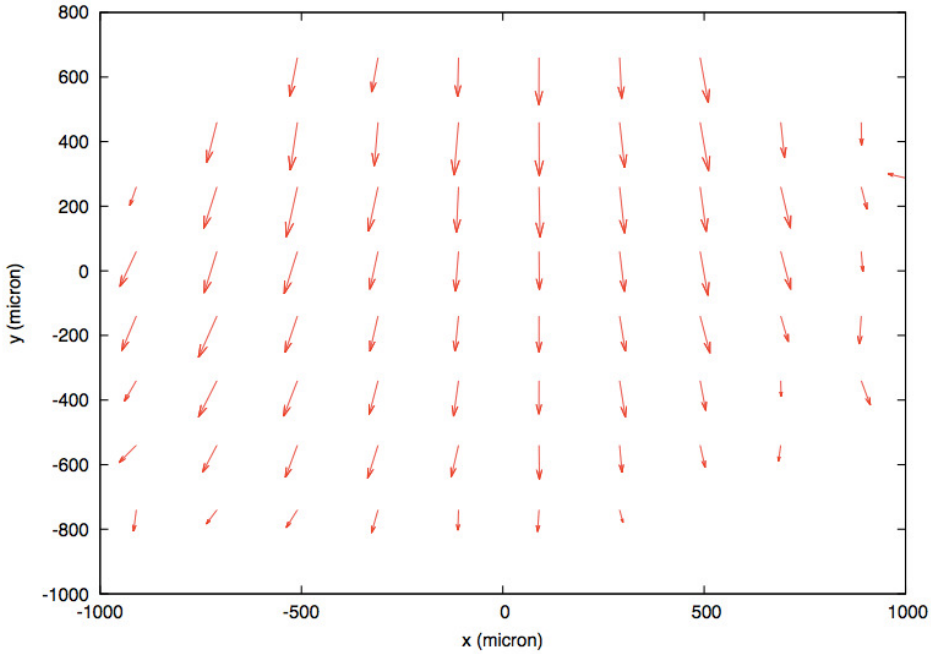

Figure 3.2: Vector field of convection currents - estimated by measuring polystyrene beads at high frequency. Only lateral components are shown, as no bin had significant motion in the z dimension, and data are averaged over axial position. Velocity arrows are scaled 10×. Regions near the periphery of the imaged region have small volume due to the pyramidal tapering and so the corresponding estimates are noisier.

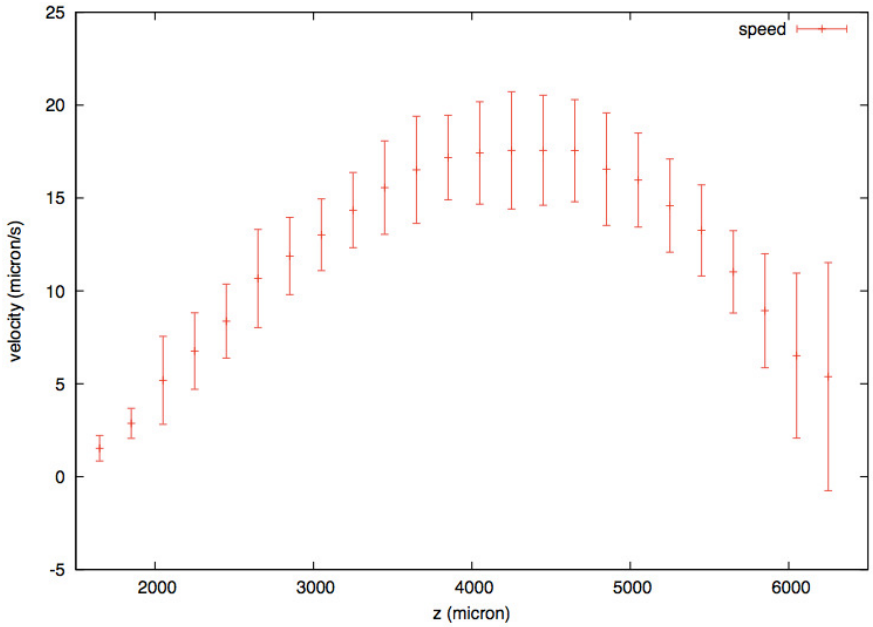

Figure 3.3: Speed profile of convection currents - estimated by tracking polystyrene beads. The magnitude of measured velocity is plotted as a function of position along the optical axis, combining data from all lateral positions. Error bars include plus and minus one standard error.

3.5 Protocols

3.5.1 Cultures

The UTEX 2244 mt+ (University of Texas culture collection) strain of *Chlamydomonas reinhardtii* was used in all experiments. Cultures were initiated from frozen stocks and grown in Sager-Granick medium under ∼7000 lux at 25 C, in 20 mL aliquots in 125 mL Erlenmeyer flasks. Cells were harvested from these cultures at mid-log phase to start experiments (cell density $\sim 4 \times 10^4$ /mL).

The *Tetrahymena thermophila* strain used in all experiments was a histone-yellow fluorescent protein fusion (H3.2::EYFP) described previously(9). Populations were kept as soybean stock cultures at 23 C, at a relatively constant density of 1000 /mL. A 50 μL aliquot from soybean stocks was used to start 50 mL cultures in SPP growth medium, grown at room temperature to mid-log phase (1-2 $\times 10^5$ /mL) for starting experiments.

To start experiments, cells were washed twice in the experimental medium. After washing, population density was measured by haemocytometry or flow cytometry and a master mix dilution was prepared in the experimental medium. For all experiments the starting densities were 5000 /mL for *C. reinhardtii* and 500 /mL for *T. thermophila*. For most experiments, cuvettes were loaded with 1.6 mL of master mix, leaving an air bubble of approximately 400 μL.

3.5.2 Cuvette cleaning

Cuvette cleaning is crucial, as any scattering dust or debris will effect the reconstruction quality. The following protocol was found to remove all detritus from previous experiments while leaving cuvettes optically clear. Before each experiment, cuvettes are rinsed several times with deionized (DI) water. All rinsing steps with water are performed with a cuvette washer (Sigma-Aldrich).

1. Fill cuvette with DI water and Starna cells surfactant cuvette cleaner (`http:`

//www.starna.com/ukhome/faqdatasheet/MSDS-CellClean.htm). Scrub interior of cuvette with dust free Q-tip, and exterior with Pec-Pad (Photographic Solutions, Hallandale, FL) soaked in isopropyl alcohol (IPA).

2. Rinse with 50 mL DI water.
3. Fill cuvette with 50% nitric acid and soak for 2-4 hours.
4. Rinse with 300 mL DI water.
5. Rinse with 6 mL IPA.
6. Dry with nitrogen gas.
7. Cap cuvettes with PTFE stoppers and place in sterile Petri dishes.

3.5.3 Sterilization

Autoclaving was found to deposit a residue on the glass surface which interfered with holographic imaging and was difficult to remove. For this reason, sterilization of sample cuvettes is accomplished by UV illumination from a transilluminator (Fisher Scientific). The four sides of the stopper-sealed, washed cuvettes are exposed to the UV lamp for a minimum of 30 minutes each.

3.5.4 Sealing

The quality of cuvette sealing as measured by evaporation rates was found to correlate with the total biomass in the three species ecosystems studied by Hekstra(9). In our two species ecosystems, the sealing quality was found to have an effect on population dynamics and phenotypic changes, as detailed in chapter 5. Two methods were used to seal cuvettes in our experiments. The first method was simply to push the PTFE stopper into the ground glass port of the cuvette, which resulted in an evaporation rate of 3.6±1.6 mg/day. The second method was to coat the sides of the PTFE stopper

lightly with Apiezon M grease (M&I Materials Ltd., Manchester, UK), push it into the port of the cuvette, then cut the PTFE flush to the cuvette with a razor blade. The cuvette top was wiped with ethanol and allowed to air dry in a sterile hood for 10 minutes. A specialized epoxy (P/N T905, Epoxy Technology, Billerica, MA) was then used to seal over the PTFE stopper to cuvette junction. To allow the epoxy to cure, the cuvettes were placed in a 25 C incubator with 7000 lux illumination for approximately 18 hours before loading into DIH microscopes. The evaporation rates measured using this method of sealing averaged 0.02 mg/day, with examples shown in Figure 3.4.

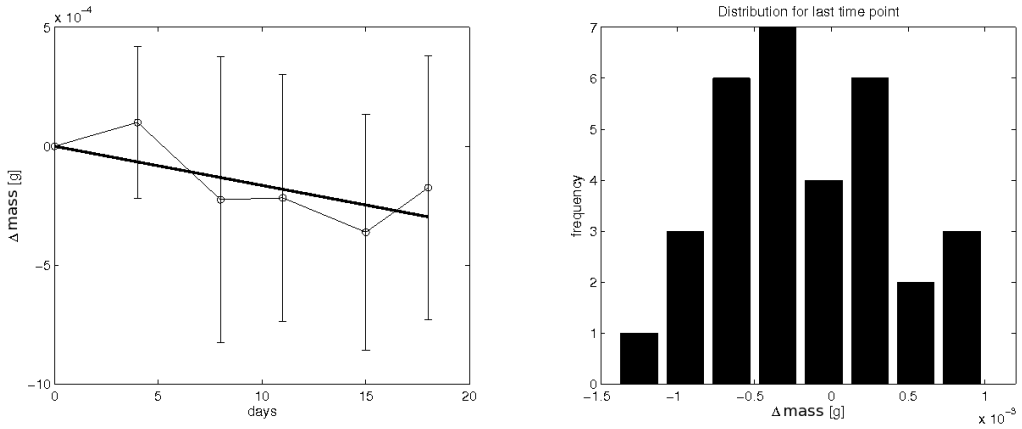

Figure 3.4: Example evaporation rate measurements - 32 cuvettes were sealed with grease and epoxy then stored in a 25 C incubator and weighed over 18 days. An additional 3 cuvettes were outliers with evaporation rates that exceeded the mean by 10 fold (not shown). The time series on the left has mean slope equal to 0.016 mg/day. The right panel shows the histogram of losses after 18 days.

3.5.5 Microscope loading

Cuvettes were loaded serially into microscopes to begin acquisitions. The time between removal from the incubator and establishment of boundary conditions and hologram acquisitions was typically less than 5 minutes but could be as long as 20 minutes when slight realignments of the laser beam or additional cleanings of cuvette outer windows were necessary. At the beginning of each acquisition, 30-60 holograms were acquired

in rapid succession to median project as an estimate of the reference beam intensity. This projection yielded good estimates up to cell densities of 4×10^4 /mL.

3.5.6 Flow cytometry

Flow cytometry was used to estimate total cell density at the end of DIHM acquisitions. Aliquots of mixed suspensions from ecosystems were mixed with Spherotech AccuCount 5.2 μm diameter fluorescent beads (ACFP-50-5, Spherotech, Lake Forest, IL), fluorescing in green, orange and red, to a bead concentration of 10^5 /mL. Sytox Green (Invitrogen, Carlsbad, CA) at 10 nM was used to assess viability after incubation with cells in the dark for 5 minutes prior to flow cytometry - this dye is excluded by intact, live cells and emits in the green.

The cell, bead and stain suspension was vortexed in the flow cytometry tube and loaded into the machine (BD LSRII-1 cytometer). To minimize the effect of phototaxis, the tube was covered in foil. The cytometer flow rate was $\sim$ 50 μL/s ("medium" setting). Typical fluorescence data is shown in Figure 3.5 - the signal from beads was easily isolated and the counts are used to estimate the sample volume from the initial bead density, from which the cell density was inferred. Data from viability assay is shown in the central panel of Figure 3.6. The channel from the flow cytometer most analogous to the intensity reconstructed in DIHM is foward scattering peak area, although the wavelength used for this channel was 488 nm, and orientation of cells within the flow focus occasionally produced spurious bimodal distributions not observed with DIHM (Figure 3.6, right panel).

3.5.7 Experiment termination

At the end of experiments, cuvettes were weighed and inspected manually with a fluorescence microscope, then unsealed by soaking the epoxy end in dichloromethane for 10 minutes, permitting removal of epoxy with a razor blade. Cuvette tops were wiped with

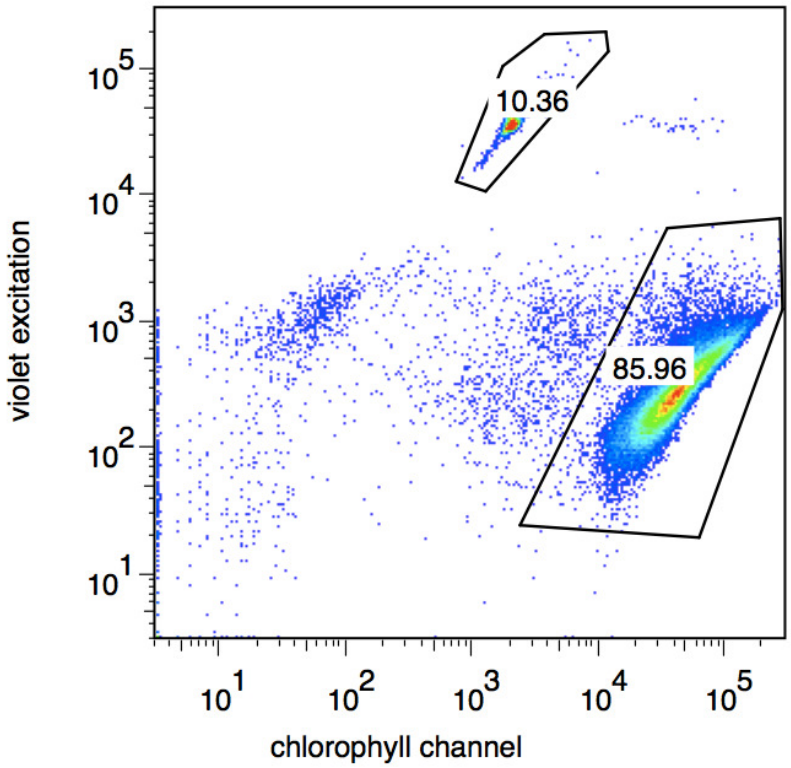

Figure 3.5: Example flow cytometry data - sample contained a late exponential phase culture of *C. reinhardtii*. Two gates are shown, one containing fluorescent beads (upper, 10%), the other containing cells (right, 86%), separated in two fluorescence channels.

water then ethanol, and the PTFE stoppers were removed. 400 μL from each cuvette was used for the contamination assay, which consisted of plating 50 μL on four nutrient conditions, in duplicate. The plate conditions were nutrient broth, thioglycolate broth, Luria-Bertani (LB) broth and yeast extract peptone dextrose medium (YPD). Plates were stored at room temperature and inspected 7 days after plating. Flow cytometry was performed on a 400 μL aliquot from each cuvette to estimate total cell density and viable cell counts, pH was measured with pH paper, and a 400 μL aliquot from each cuvette was diluted into 5 mL of SPP growth medium to subculture viable cells.

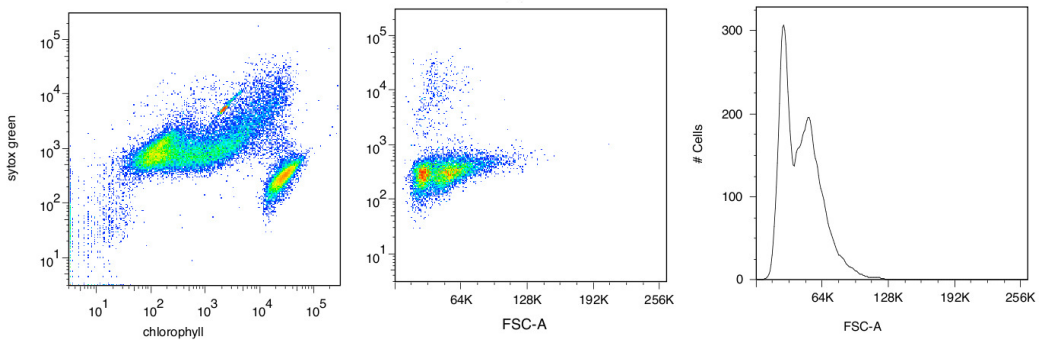

Figure 3.6: Flow cytometry data from *C. reinhardtii* growth experiment - data from FACS run performed after termination of acquisition. Left panel - no gating; small upper peak is fluorescent beads, lower right peak corresponds to cells. Middle panel - forward scattering peak area (FSC-A) vs. Sytox Green signal, showing viable population (bottom) and dead cells (top). Right panel - histogram of FSC-A for viable population, showing bimodal distribution.

3.6 Media

3.6.1 Modified Sager-Granick

Recipe from *Chlamydomonas* center (`http://www.chlamy.org/SG.html`), with trace elements component replaced by Hutner's trace elements (`http://www.chlamy.org/trace.html`)(11, 19):

Make the following separate stock solutions:

1. Hutner's trace elements

For 1 L final mix, dissolve each compound in the volume of water indicated. The EDTA should be dissolved in boiling water, and the $FeSO_4$ should be prepared last to avoid oxidation.

compound	mass	water volume
EDTA disodium salt	50 g	250 mL
$ZnSO_4 \cdot 7\,H_2O$	22 g	100 mL
H_3BO_3	11.4 g	200 mL
$MnCl_2 \cdot 4\,H_2O$	5.06 g	50 mL
$CoCl_2 \cdot 6\,H_2O$	1.61 g	50 mL
$CuSO_4 \cdot 5\,H_2O$	1.57 g	50 mL
$(NH_4)_6Mo_7O_{24} \cdot 4\,H_2O$	1.10 g	50 mL
$FeSO_4 \cdot 7\,H_2O$	4.99 g	50 mL

Mix all solutions except EDTA. Bring to boil, then add EDTA solution. The mixture should turn green. When everything is dissolved, cool to 70 C. Keeping temperature at 70 C, add 85 mL hot 20% KOH solution. Do NOT use NaOH to adjust the pH.

Bring the final solution to 1 L total volume. It should be clear green initially. Stopper the flask with a cotton plug and let it stand for 1-2 weeks, shaking it once a day. The solution should eventually turn purple and leave a rust-brown precipitate, which can be removed by filtering through two layers of Whatman #1 filter paper, repeating filtration if necessary until the solution is clear. Store refrigerated or frozen convenient aliquots. The formation of precipitate can be catalyzed by bubbling the solution with filtered air.

If not precipitate forms, the solution is still usable. However, the pH may need to be adjusted to 7.0 using either KOH or HCl as needed.

2. sodium citrate

$\text{sodium citrate} \cdot 2\,H_2O$	500 g
water to 1 L	

3. iron chloride

$FeCl_3 \cdot 6\,H_2O$	10 g
water to 1 L	

4. calcium chloride

$CaCl_2 \cdot 2\,H_2O$ 53 g
water to 1 L

5. magnesium sulfate

$MgSO_4 \cdot 7\,H_2O$ 300 g
water to 1 L

6. ammonium salt

NH_4Cl 600 g
water to 1 L

7. potassium phosphate, monobasic

$KH_2PO_4 \cdot 7\,H_2O$ 200 g
water to 1 L

8. potassium phosphate, dibasic

$K_2HPO_4 \cdot 7\,H_2O$ 200 g
water to 1 L

To make final medium, mix 1.0 mL each of solutions 1-6, and 0.5 mL of solutions 7 and 8. For nitrogen deprivation experiments, reductions were made in the volume of ammonium chloride solution added. The final pH should be 6.9.

3.6.2 1× Taub #36

Recipe from Hekstra 2009(9), for 1 L 1× Taub #36:

Part A (final mixture)

Bring volume to 998 mL with double-distilled H_2O. Filter sterilize and store at room temperature for up to one month, at which point a precipitate forms.

Part B

NaCl	175.3 mg
part B	2.0 mL
part C	2.0 mL
part D	6.67 mL
part F	125 μL
part G	1.0 mL

Dissolve 12.35 g $MgSO_4 \cdot 7\,H_2O$ in 500 mL double-distilled H_2O and autoclave.

Part C

Dissolve 6.80 g KH_2PO_4 and 1.60 g NaOH in 500 mL double-distilled H_2O, adjust pH to 7.5 and autoclave.

Part D

Dissolve 3.33 g $CaCl_2$ (anhydrous, hygroscopic) in 100 mL double-distilled H_2O and autoclave.

Part E

Not used

Part F

Dissolve 26.1 g EDTA in 268 mL 1 M NaOH.

Add 24.9 g $FeSO_4 \cdot 7\,H_2O$ and adjust volume to 1 L with double-distilled H_2O.

Aerate overnight in chemical hood.

Filter sterilize and store at room temperature shielded from light. The solution should be stable in the dark for at least 1 year.

Part G

Dissolve in this order in 1 L double-distilled H_2O:

H_3BO_3	1.854 g
$ZnSO_4 \cdot 7\,H_2O$	0.287 g
$MnCl_2 \cdot 4\,H_2O$	1.36 g
$Na_2MoO_4 \cdot 2\,H_2O$	0.242 g
$CuSO_4 \cdot 5\,H_2O$	0.0499 g
$Co(NO_3)_2 \cdot 6\,H_2O$	0.291 g

Filter sterilize and store at room temperature, shielded from light. The $MnCl_2 \cdot 4\,H_2O$

can be replaced with 1.98 g $MnCl_2 \cdot 9\,H_2O$.

Bibliography

[1] David J. Asai and James D. Forney, editors. *Methods in Cell Biology*, volume 62: *Tetrahymena thermophila*. Academic Press, San Diego, CA, 2000. 61

[2] Lea K. Bleyman, Mary P. Baum, Peter J. Bruns, and Eduardo Orias. Mapping the mating type locus of *Tetrahymena thermophila*: Meiotic linkage of *mat* to the ribosomal RNA gene. *Developmental Genetics*, 13:34–40, 1992. 61

[3] Poppo H. Boer, Linda Bonen, Robert W. Lee, and Michael W. Gray. Genes for respiratory chain proteins and ribosomal RNAs are present on a 16-kilobase-pair DNA species from *Chlamydomonas reinhardtii* mitochondria. *Proceedings of the National Academy of Sciences of the United States of America*, 82:3340–3344, 1985. 58

[4] Poppo H. Boer and Michael W. Gray. The URF 5 gene of *Chlamydomonas reinhardtii* mitochondria: DNA sequence and mode of transcription. *The EMBO Journal*, 5:21–28, 1985. 58

[5] Poppo H. Boer and Michael W. Gray. Nucleotide sequence of a protein coding region in *Chlamydomonas reinhardtii* mitochondrial DNA. *Nucleic Acids Research*, 14:7506–7507, 1986. 58

[6] Victor G. Bruce. The biological clock in *Chlamydomonas reinhardi*. *Journal of Eukaryotic Microbiology*, 17:328–334, 1970. 59

[7] Mary Ella Harman Feinleib and George M. Curry. The relationship between stimulus intensity and oriented phototactic response (topotaxis) in *Chlamydomonas*. *Physiologia Plantarum*, 25:346–352, 1971. 59

[8] Elizabeth Harris, editor. *The* Chlamydomonas *source book*. Academic Press, San Diego, CA, second edition, 2009. 58, 59, 60

[9] Doeke Hekstra. *Population dynamics in a model closed ecosystem*. PhD thesis, The Rockefeller University, New York, New York, 2009. 58, 63, 66, 67, 73

[10] Per Hellung-Larsen, Vagn Leick, and Niels Tommerup. Chemoattraction in *Tetrahymena*: on the role of chemokinesis. *The Biological Bulletin*, 170:357–367, 1986. 61

[11] S. H. Hutner, L. Provosoli, Albert Schatz, and C. P. Haskins. Some approaches to the study of the role of metals in the metabolism of microorganisms. *Proceedings of the American Philosophical Society*, 94:152–170, 1950. 71

[12] Z. Kawabata, K. Matsui, K. Okazaki, M. Nasu, N. Nakano, and T. Sugai. Synthesis of a species-defined microcosm with protozoa. *Journal of Protozoology Research*, 1995:23–26, 1995. 58, 63

[13] L. D. Landau and E. M. Lifshitz. *Fluid Mechanics - Course of Theoretical Physics*, volume 6. Butterworth-Heinemann, Oxford, UK, second edition, 1987. 63

[14] Nancy C. Martin and Ursula W. Goodenough. Gametic differentiation in *Chlamydomonas reinhardtii*. I. Production of gametes and their fine structure. *The Journal of Cell Biology*, 67:587–605, 1975. 59

[15] Jude E. Maul, Jason W. Lilly, Liying Cui, Claude W. dePamphilis, Webb Miller, Elizabeth H. Harris, and David B. Stern. The *Chlamydomonas reinhardtii* plastid chromosome: islands of genes in a sea of repeats. *The Plant Cell*, 14:1–21, 2002. 58

[16] Sabeeha S. Merchant, Simon E. Prochnik, Olivier Vallon, Elizabeth H. Harris, Steven J. Karpowicz, George B. Witman, Astrid Terry, Asaf Salamov, Lillian K. Fritz-Laylin, Laurence Maréchal-Drouard, Wallace F. Marshall, Liang-Hu Qu, David R. Nelson, Anton A. Sanderfoot, Martin H. Spalding, Vladimir V. Kapitonov, Qinghu Ren, Patrick Ferris, Erika Lindquist, Harris Shapiro, Susan M. Lucas, Jane Grimwood, Jeremy Schmutz, *Chlamydomonas* Annotation Team, JGI Annotation Team, Igor V. Grigoriev, Daniel S. Rokhsar, and Arthur R. Grossman. The *Chlamydomonas* genome reveals the evolution of key animal and plant functions. *Science*, 318:245–251, 2007. 58

[17] J. R. Preer. Epigenetic mechanisms affecting macronuclear development in *Paramecium* and *Tetrahymena*. *Journal of Eukaryotic Microbiology*, 47:515–524, 2000. 61

[18] T. J. Racey, R. Hallett, and B. Nickel. A quasi-elastic light scattering and cinematographic investigation of motile *Chlamydomonas reinhardtii*. *Biophysical Journal*, 35:557–571, 1981. 58

[19] Ruth Sager and S. Granick. Nutritional studies with *Chlamydomonas reinhardi*. *Annals of the New York Academy of Sciences*, 56:831–838, 1953. 60, 71

[20] Ruth Sager and S. Granick. Nutritional control of sexuality in *Chlamydomonas reinhardi*. *The Journal of General Physiology*, 37:729–742, 1954. 59

[21] M. A. Sanders and J. L. Salisbury. Centrin plays an essential role in microtubule severing during flagellar excision in *Chlamydomonas reinhardtii*. *The Journal of Cell Biology*, 124:795–805, 1994. 59

[22] Robert L. Stavis and Rona Hirschberg. Phototaxis in *Chlamydomonas reinhardtii*. *The Journal of Cell Biology*, 59:367–377, 1973. 59

[23] Frieda B. Taub and Alexander M. Dollar. A *Chlorella*-daphnia food-chain study - the design of a compatible chemically defined culture medium. *Limnology and Oceanography*, 9:61–74, 1964. 58

[24] Aaron P. Turkewitz, Eduardo Orias, and Geoffrey Kapler. Functional genomics: the coming of age for *Tetrahymena thermophila*. *TRENDS in Genetics*, 18:35–40, 2002. 61

Chapter 4

Single species ecosystems

This chapter describes the dynamics of ecosystems consisting of a single species - either *Chlamydomonas reinhardtii* or *Tetrahymena thermophila*. A short term experiment with 9 replicates of an exponentially growing population of *C. reinhardtii* in rich medium demonstrates the acquisition of data at high temporal frequency. A long term experiment with 7 replicate ecosystems of *C. reinhardtii* under conditions of nitrogen starvation and exposed to perturbations of light intensity is presented in detail. Weeks into the experiment the variance of single time point measurements across replicates was of comparable magnitude to the sampling noise for all systems, indicating a surprising degree of repeatability. The amplitude of the perturbation did not have an effect on the repeatability, which also extended to observed spatial heterogeneities in population density. Additional experiments were conducted to test the response of *C. reinhardtii* ecosystems to perturbations in light intensity. An experiment with *T. thermophila* in isolation is presented, consisting of 12 replicates. Extinction was observed in 11 of 12 systems within 20 days, and the observed dynamics were repeatable both across replicates and across repetitions of the experiment.

4.1 *Chlamydomonas* in rich medium

An experiment was conducted in rich medium to measure the initial growth phase at high temporal frequency. Nine replicates were prepared with Sager-Granick medium with Hutner's trace metals and data was acquired for 60 hours at a frequency of 800 seconds. A 12 hour period of darkness was imposed at the beginning of the acquisition to partially synchronize the populations, followed by constant illumination at 1100±60 lux symmetrically from above and below by the 3200 K LEDs. The volume of cell suspension for this experiment was 2 mL, which left only a very small air bubble from inserting the PTFE stopper. All other experimental parameters were typical, as described in chapter 3.

4.1.1 Repeatability

Population dynamics for individual systems are shown in Figure 4.1 and mean dynamics and fluctuations are shown in Figure 4.2. Roughly one doubling occurs during the 12 hour dark interval, followed by a rapid response to the increase in illumination, presumably due to migration. There follows an increase in the population density by a factor of 30 over the next 48 hours, corresponding to a doubling time of 9.6 hours. The differences in counts between systems are remarkably small, as shown in Figure 4.2 - from hour 40 to 60, the coefficient of variation (CV) does not exceed 20%. This variation includes sampling noise, and no temporal filter is applied to reduce its contribution. To compare the measured variation to that expected from sampling noise alone, we took the mean density across replicates as the rate of a Poisson distribution for each time point, and considered the ratio of the CV observed to the CV from the Poisson distributed counts (Figure 4.2). This ratio is seen to increase with time, possibly reflecting differences across systems in carrying capacity.

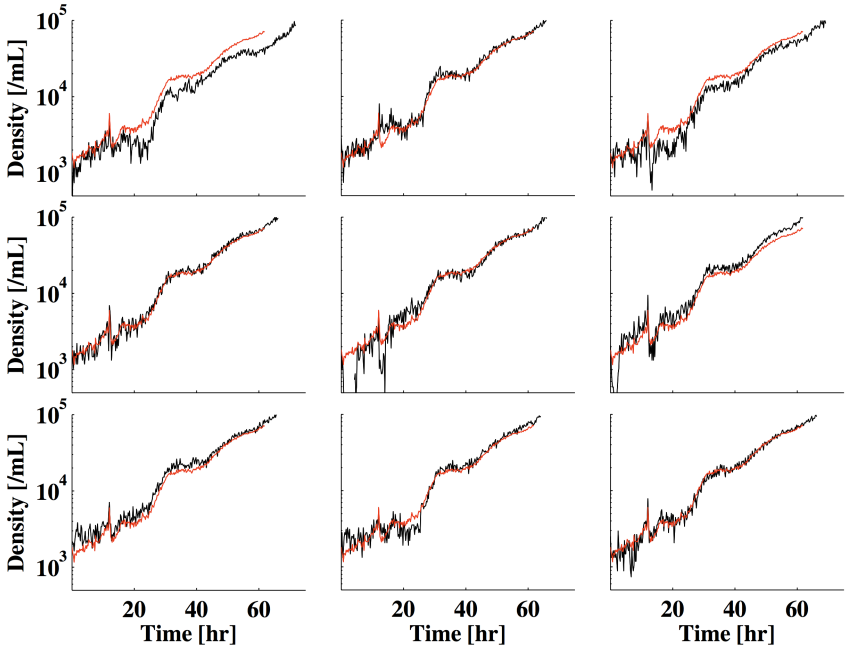

Figure 4.1: Growth dynamics from individual *Chlamydomonas* systems - Population densities measured in 9 systems are plotted versus time in black, with the mean plotted in red.

4.1.2 Sampling noise

A portion of the observed fluctuations are due to sampling noise, which adds a variance equal to the mean. To quantify the temporal fluctuations, we isolated an interval of 21 time points around 30 hours in which the population density was fairly constant. To increase the effective number of measurements, we partitioned the analyzed volume into 9 subvolumes. These were each 150 μm wide in x, extending from -675 to 675 μm in y and 3,600 to 6,200 μm in z, and spanning from -675 to 675 μm in x. This resulted in 189 measurements, which are displayed as a histogram in Figure 4.3, along with the best fit Poisson distribution (rate $\lambda = 8.35$). The χ^2 test fails to reject the null hypothesis that the measured counts were drawn from the Poisson distribution (p=0.6).

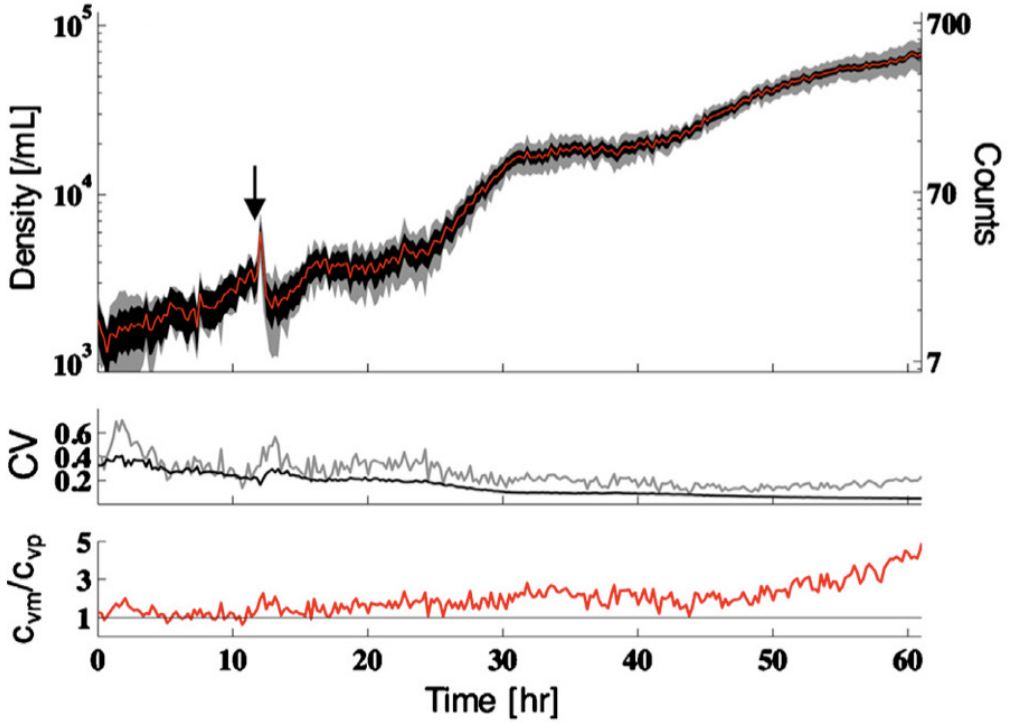

Figure 4.2: Statistics of growth dynamics from 9 *Chlamydomonas* systems - The top panel shows mean dynamics (line) with empirical standard error (gray) and standard deviation expected from Poisson statistics with rate equal to the empirical mean (black). The LED illumination was turned on at 12 hours as indicated by the arrow. The middle panel shows the coefficient of variation (CV) measured (CV_m, gray) and the mean CV assuming Poisson statistics (CV_P, black). The bottom panel shows the ratio of CVs CV_m/CV_P. The black line indicates $CV_m/CV_P = 1$, where variation is equal to that expected from sampling statistics.

4.1.3 Spatial distribution

The spatial distribution contained reproducible gradients. We estimated the spatial distribution of cell density by dividing the counts into 150×150×332 μm^3 bins in x, y and z, respectively. Counts from all time points were included, resulting in an estimate of the temporally averaged spatial distribution. The ratio of individual bin densities to mean bin density is shown in Figure 4.4. We observed spatial gradients in the y and z dimensions which were reproducible across systems and stable in time. No gradient along the x axis was detected. The magnitude of the y gradient was 50% over 1.5 mm,

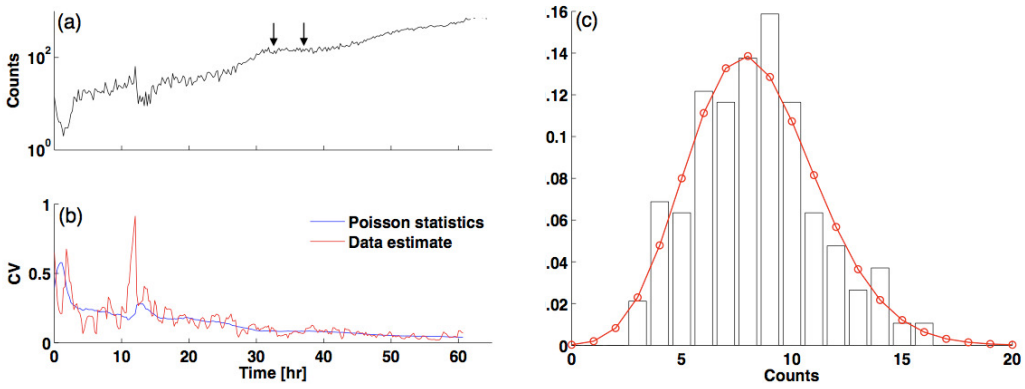

Figure 4.3: Poisson distribution of high frequency fluctuations - (a) Time series from a single system during short term growth experiment with *Chlamydomonas*. Arrows indicate an interval of relatively constant density used to construct the histogram of counts in (c), (b) coefficient of variation estimated in a moving window of 5 time points (red line) plotted with the expected coefficient of variation assuming Poisson distributed fluctuations with rate given by the empirical mean (blue line), (c) probability density of counts within 9 sub-volumes across 21 measurements from the interval indicated in (a), comprising 189 observations. The best fit Poisson distribution is shown in red (rate $\lambda = 8.35$). Similar results were observed in all experiments considered.

while the gradient in z was approximately 25% over 5 mm.

No sign of contamination was found on plates from any replicate. Flow cytometry measured a total cell density from stirred samples of 1.62×10^5 /mL, with 3.2% dead cells.

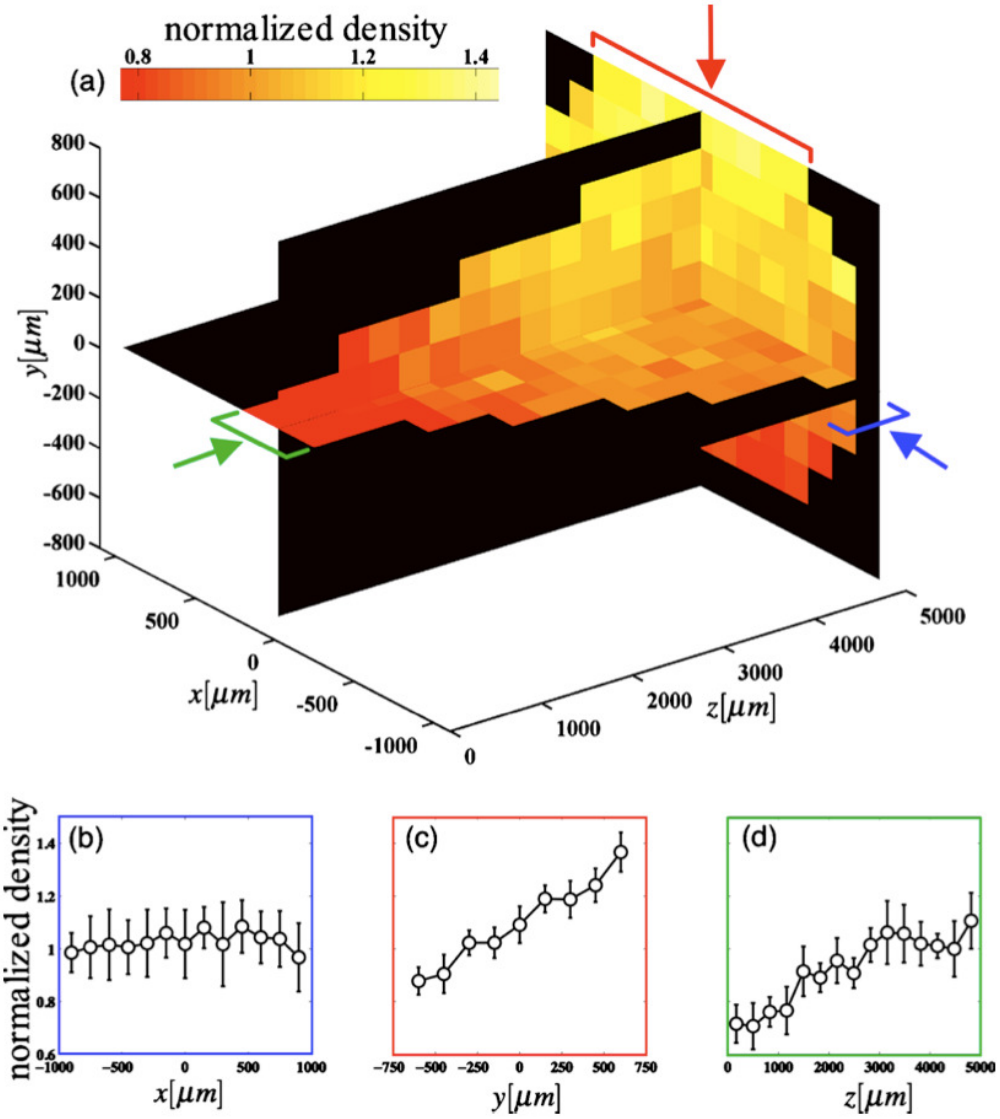

Figure 4.4: Spatial distribution from short term experiments with 9 *Chlamydomonas* systems in growth conditions - For each microscope, the imaged volume was divided into 150 × 150 × 332 μm^3 bins in x, y and z, respectively. The counts within each bin were summed across the entire 60 hour acquisition shown in Figure 4.2, resulting in an average of ∼50 counts/bin in each microscope. For each bin we compute the normalized density, which is the ratio of the number of counts to the number of counts expected for a spatially uniform distribution. (a) average normalized density across systems for three planes within the imaging volume, (b)-(d) profiles in x, y and z, respectively, in bins indicated by arrows and bars in (a). Gravity points in the $-y$ direction. Error bars represent 1 standard error.

4.2 *Chlamydomonas* in low nitrogen medium

A long term experiment was conducted in low nitrogen medium, with . Our preliminary search for conditions which would yield densities sufficiently low for DIHM measurements supported limiting nitrogen concentrations in the media. Seven replicates were prepared in Sager-Granick medium with Hutner's trace metals, modified to contain 25 μM ammonium - the only accessible nitrogen source. The mean illuminance from the white LEDs was 800±40 lux, symmetric from above and below. Fluctuations about the mean of amplitudes 0%, 10% and 30% were imposed in the form of uniform white noise to 1 Hz for the duration of the experiment. Each noise amplitude was applied to two replicates. Measurements were made every 1600 seconds for 30 days. All other parameters were typical, as described in chapter 3.

The dynamics were highly repeatable across systems for the duration of the experiment (Figures 4.5 and 4.6). An initial rapid increase in counts by a factor 50, corresponding to a doubling time of 13 hours, was followed by drop by a factor 5, followed by a second sharp increase, and a gradual decrease sustained for the remainder of the experiment. From hour 420 until the end of the experiment, the rate of change in population density was very small, corresponding to a half life of roughly 20 days. The amplitude of the noise in illuminance did not have an effect on the measured population dynamics.

As for the previous experiment, we considered the CV as a function of time as well as the ratio of the measured CV (CV_m) to that expected from a Poisson distribution (CV_P). After an initial period of relatively large fluctuations, the CV was below 0.2 after about 10 days. The mean CV_m/CV_P ratio was 1.45 during the latter interval, indicating that the variability across systems exceeded the counting noise by only 45%. In one replicate, the LEDs were turned off at 600 hours[1], and a rapid and large response was observed in the population density, which declined to only a few counts per hologram

[1]Counts from this ecosystem were omitted from statistical analysis.

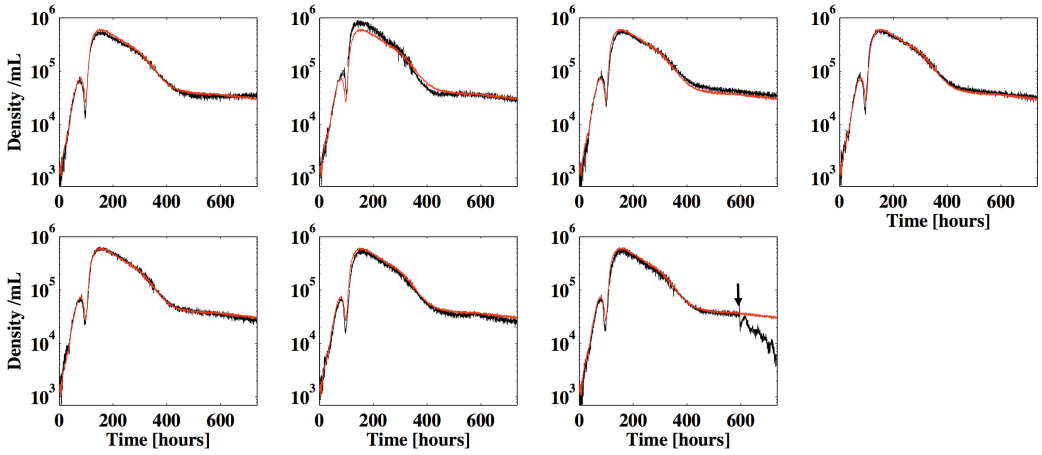

Figure 4.5: Long term nitrogen depravation dynamics from individual *Chlamydomonas* systems - Population densities measured in 7 systems are plotted versus time in black, with the mean of the first 6 systems plotted in red. In the top row, fluctuations in the LED illumination intensity were applied at the following amplitudes, from left to right (as fractions of the mean intensity): 30%, 30%, 10% and 10%. Illumination intensity for the bottom row was constant. In the lower right panel, the LEDs were turned off at 600 hours as indicated by the black arrow.

by the end of the acquisition. This response shows that the nearly constant cell density and striking repeatability across systems are sensitive to the environmental conditions.

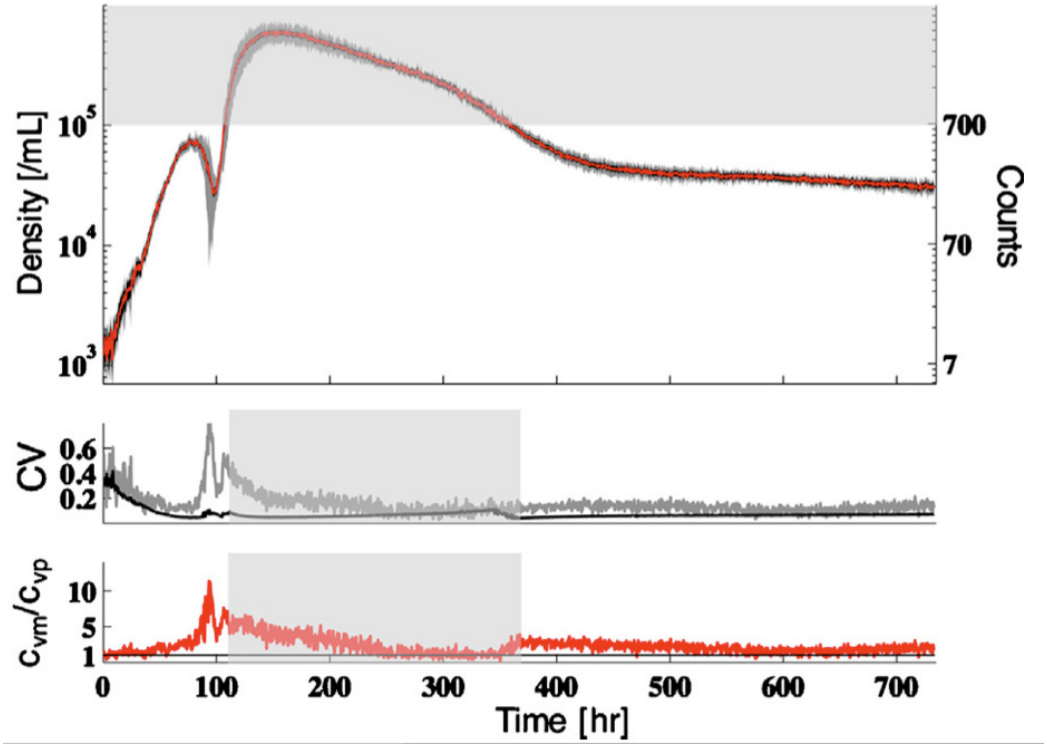

Figure 4.6: Statistics of long term nitrogen deprivation dynamics from 6 *Chlamydomonas* systems - The top panel shows mean dynamics (line) with empirical standard error (gray) and standard deviation expected from Poisson statistics with rate equal to the empirical mean (black). The middle panel shows the coefficient of variation (CV) measured (CV_m, gray) and the mean CV assuming Poisson statistics (CV_P, black). The bottom panel shows the ratio of CVs CV_m/CV_P. The black line indicates $CV_m/CV_P = 1$, where variation is equal to that expected from sampling statistics. Points within the shaded region are above the maximum algal density of 10^5 /cm^3, so densities as high as 5×10^5 /cm^3 were determined from counts within a $\sim 1\,\text{mm}^3$ volume as described in section 2.6.

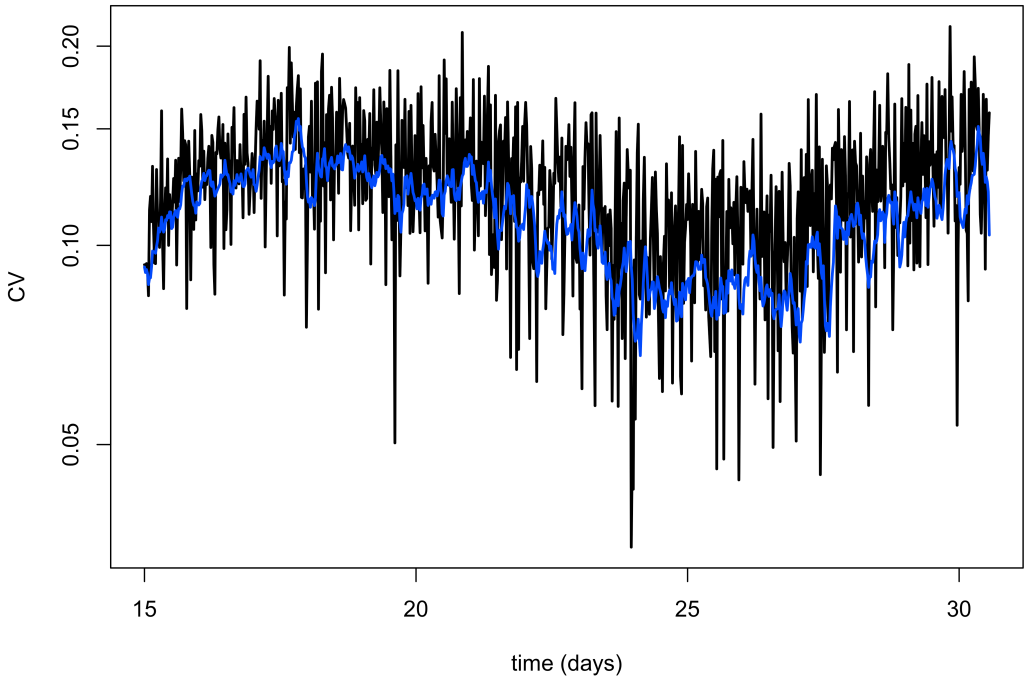

Figure 4.7: Comparison of CV for smoothed counts and raw counts - the coefficient of variation is plotted in black for raw counts from the 6 replicates presented in Figure 4.5. A uniform moving average over 67 minutes (10 measurements) was calculated for each system, and the resulting coefficient of variation is plotted in blue.

The spatial distribution was similar to that measured in the short term growth experiment described above. No evidence of contamination was found after terminating acquisitions. Flow cytometry results were similar to those from the growth experiment - most importantly, a large proportion of cells were viable.

4.3 Nitrogen starvation and illumination spectrum

A long term experiment was performed in nitrogen free medium with illumination of different spectra. The initial conditions were also varied: cultures were starved of nitrogen for 1, 2, 3 or 4 days prior to starting the experiment. Each initial starvation period was tested with "blue" (6000 K) and "red" LEDs (see section 3.4) at constant illuminance.

The dynamics varied little with initial starvation time, indicating insensitivity to this initial condition (Figure 4.8). The LED spectrum had a strong effect on dynamics. The redder spectrum resulted in an increase in density of over 10 fold over the first 6 days, followed by a decline to a minimum around 20 days, then a small increase to steady levels. The systems illuminated with the bluer spectrum reached a maximum density about 24 hours sooner than those with the red spectrum, and this maximum was approximately half as dense. Slow fluctuations occurred around this density in each system for the rest of the experiment, with a stereotypical "dip" with very fast dynamics lasting approximately 2 days which occurred in each system. The timing of this dip varied across systems by 5 days, and included an almost 10 fold reduction in population density in less than 1 day.

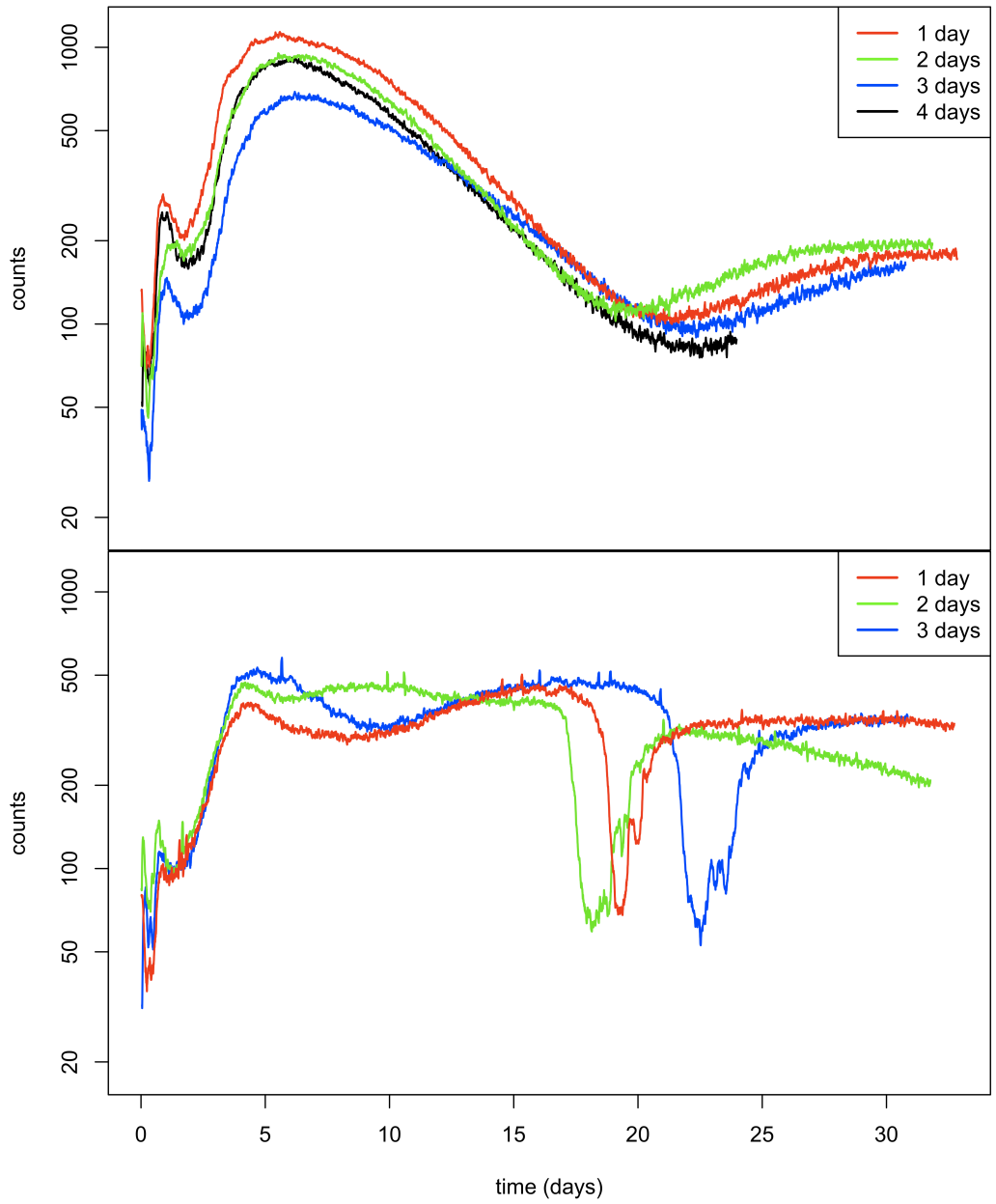

Figure 4.8: Nitrogen starvation dynamics with two illumination spectra - top panel shows *C. reinhardtii* population dynamics for four systems with "red" LED spectrum, bottom panel shows dynamics under illumination with "blue" spectrum. Cultures had been starved for 1, 2, 3 or 4 days prior to starting the experiment; the acquisition of data failed for the 4 day starvation period with "blue" LEDs. Counts are smoothed by a uniform moving average over 67 minutes.

4.4 Perturbation experiments

To probe long term population dynamics, we performed experiments with stronger perturbations in illuminance. Since no response was seen to small amplitude white noise, we chose perturbations taking the form of complete darkness, with the duration and timing of the dark interval as parameters. The dynamics under nitrogen starvation with blue illumination spectrum were fairly steady, excepting the dip beginning at 17-22 days. We reasoned that the quasi-steady state between 5 and 17 days was a convenient regime for applying perturbations.

As we had no information regarding the time scales of perturbations which would produce measurable responses, we chose a geometric series starting at 1 minute and increasing by factors of 9, with each duration applied to duplicate systems: 1 minute, 9 minutes, 80 minutes, and 720 minutes. We also lacked information regarding the history dependence of perturbation responses, so we chose to apply only a single period of darkness to 8 replicates, and for a 9th replicate we applied 1 minute intervals of darkness every 7 hours (period chosen to avoid potential complications with circadian rhythms). Cells were starved of nitrogen for 1 day prior to the acquisition and the blue spectrum LEDs were used. Ecosystems were inoculated at a higher initial cell density of 25,000 /mL.

The measured population dynamics are shown in Figure 4.9, 4.10 and 4.11. Darkness intervals of 1 minute produced no obvious response, while in all other cases, a rapid rise in densities was measured following the onset of darkness. The interpretation of the dynamics as responses to perturbations is complicated by the significant variability from system to system. An approximate 10 fold decrease in density lasting 3-5 days is observed around day 7 in all systems, although the timing and structure of this phenomenon are variable. It should be pointed out that this "dip" in the population densities was not particular to perturbed boundary conditions, as a qualitatively simi-

lar feature was observed in several preliminary experiments with nitrogen free medium and 6000 K LEDs. The temporal average of the spatial distribution was similar to that observed in the other two experiments.

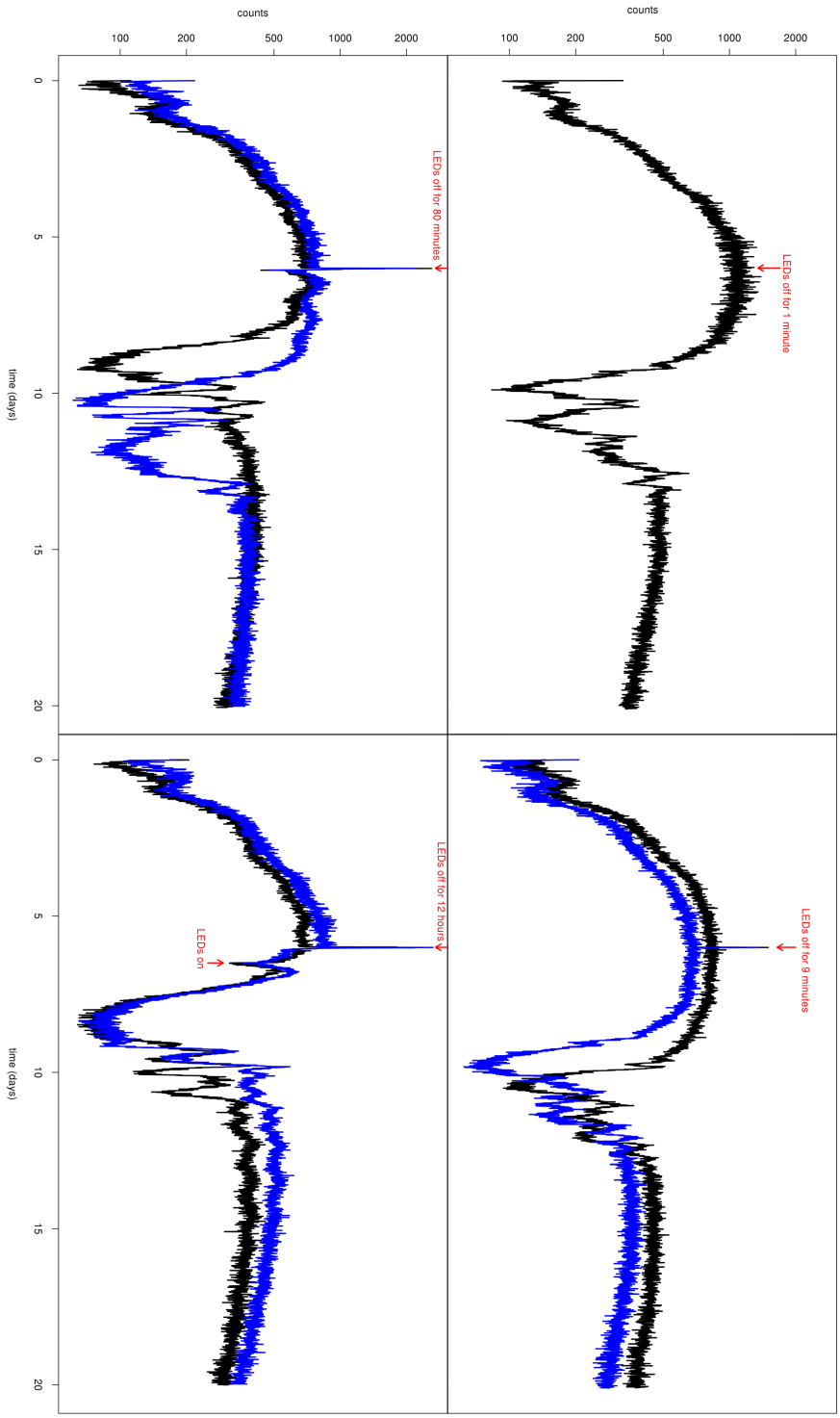

Figure 4.9: Dynamics from individual systems under perturbations to light intensity - perturbations consisted of intervals of darkness of duration 1, 9, 80 and 720 minutes, applied at day 6 to duplicate systems, as shown by the red arrows. Experiments were performed in nitrogen-free medium. Only one system's dynamics are plotted for the 1 minute perturbation due to acquisition failure.

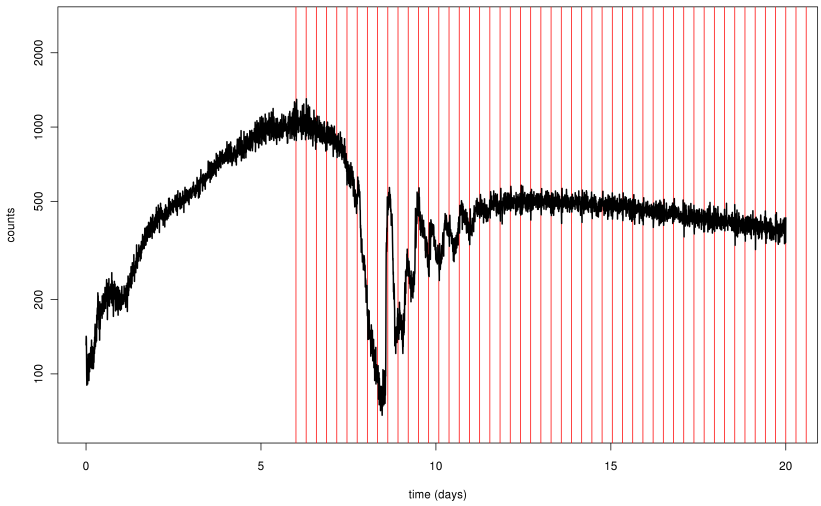

Figure 4.10: Dynamics from individual system under periodic perturbations to light intensity - perturbation consisted of 1 minute intervals of darkness applied every 7 hours, as indicated by the red lines. Experiment was performed in nitrogen-free medium.

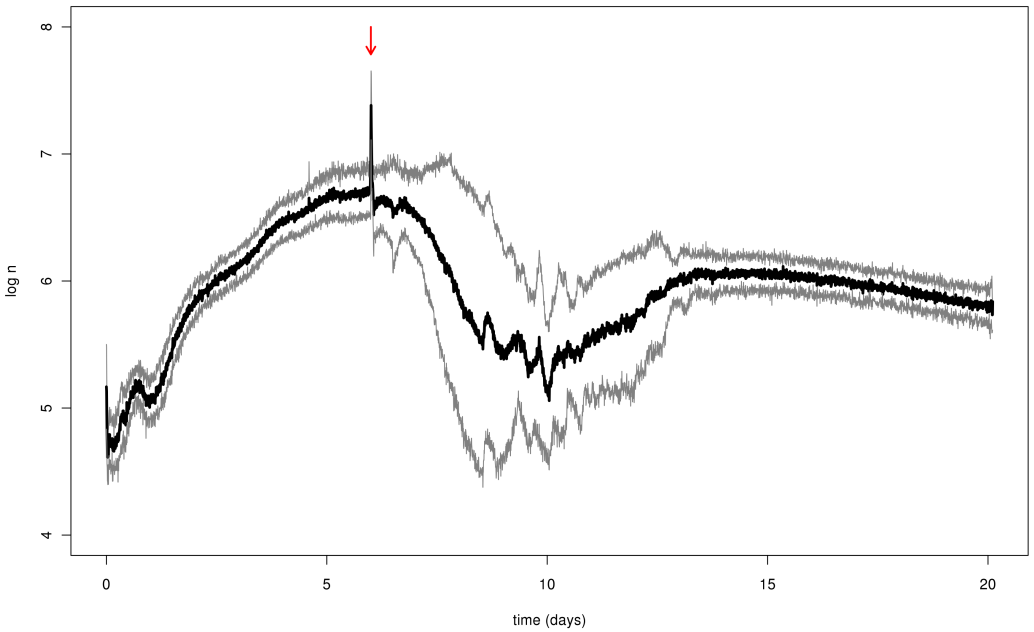

Figure 4.11: Mean dynamics under perturbations to light intensity - geometric mean of counts from 8 systems in Figures 4.9 and 4.10 plotted in black, with 1 standard error of $\log n$ on either side of the mean plotted in gray. Red arrow indicates the initial application of perturbations at day 6. The interval of large deviations between 7 and 13 days is apparently a feature of the dynamics under nitrogen starvation and not purely due to perturbations in the boundary condition.

4.5 *T. thermophila* in compatibility medium

To compare the repeatability observed in ecosystems composed of *C. reinhardtii* in isolation, we conducted two repetitions of a single species experiment with *T. thermophila*. The medium was 1/2× Taub #36 with 0.03% proteose peptone, supplemented with 3 mM acetate and 20 mM Tris, and cuvettes were sealed with PTFE stoppers, vacuum grease and epoxy as described in chapter 3. This medium was used for consistency with two species experiments, for which the supplementation with acetate and Tris was necessary for persistence of algae in well-sealed cuvettes (see section 5.2). The measured dynamics are shown in Figures 4.12 and 4.13: counts rose from 2.5 to 10 over 3 days, then declined to 0 in all systems. One system was found to contain viable *T. thermophila*, as a population was successfully subcultured from the ecosystem sample after terminating the experiment. Signs of bacterial contamination were found in both experiments, but the plating protocol is prone to false positives and there was no obvious effect on population dynamics. The ratio of the measured CV to that expected from Poisson statistics reached a maximum of 1.6 around 3 days.

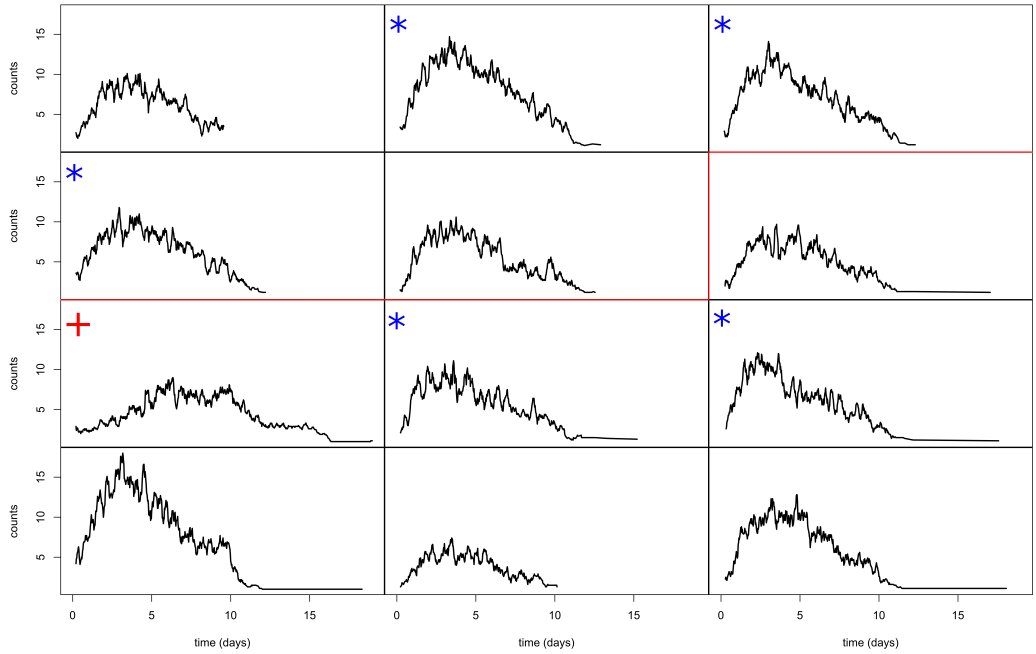

Figure 4.12: Population dynamics from individual *T. thermophila* systems - Population densities measured in 12 systems from two experiments, as moving averages over 5.7 hours due to the low counts. The medium was 1/2× Taub #36, supplemented with 0.03%proteose peptone, 3 mM acetate and 20 mM Tris, and cuvettes were sealed using PTFE stoppers, vacuum grease and epoxy. The red line separates results from the two separate experiments, blue asterisks indicate possibly contaminated systems and the red plus indicates the only system in which *T. thermophila* persisted, as tested by subculturing after termination of the experiment.

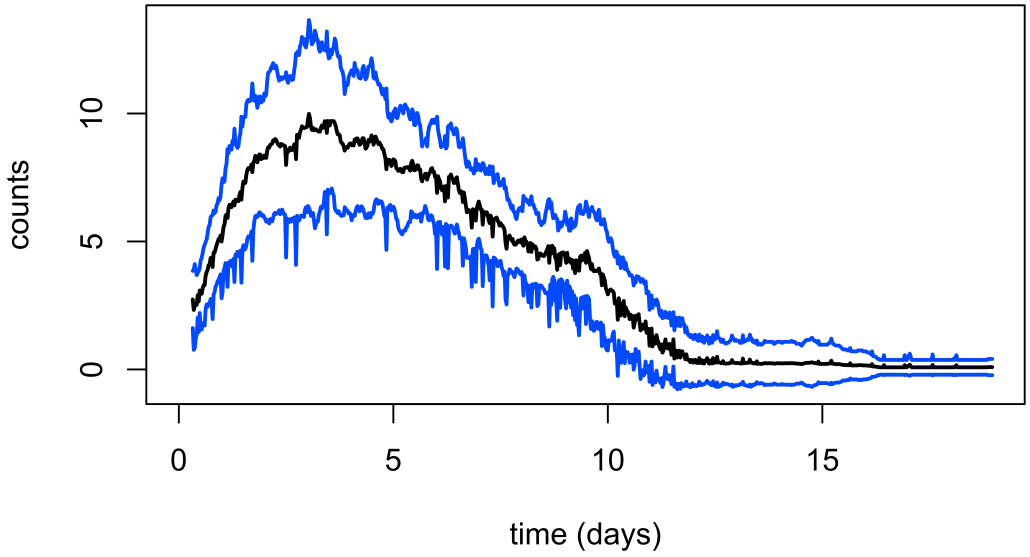

Figure 4.13: Mean dynamics from *T. thermophila* systems - the mean across the 12 systems from Figure 4.12 is plotted in black, with 1 standard deviation on either side plotted in blue.

4.6 Conclusions

Experiments with single species show that our implementation of DIHM is a useful tool for measuring population dynamics in closed ecosystems. The spatial resolution and sensitivity are sufficient to count individual microbes, the temporal resolution seems sufficient for sampling dynamics in constant boundary conditions, the analyzed region measures roughly 7 mm^3, orders of magnitude larger than non-holographic techniques, and the dynamic range extends from 1 count per imaged volume to about 1,000. The device is quite simple, and alignment is automatic.

The construction of 10 replicate instruments allows statistical characterization of a single experiment run in parallel, and the boundary conditions of temperature and light are well controlled. These features were used to measure a surprising degree of repeatability in population dynamics of *C. reinhardtii* as a function of time and space, showing that there exist closed ecosystems which require extremely precise measurements in order to resolve differences. In this case, even random fluctuations in the boundary condition with amplitudes measuring 30% of the mean did not produce measurable differences across systems. The dynamics of *T. thermophila* were similarly repeatable, although in this case counts were low and extinction was observed within two weeks.

In all cases the dynamics were insensitive to variation in the initial conditions. The variation in initial cell densities is determined by pipetting error, which determines the total initial volume, and sampling noise. Other sources of variation have not been quantified, such as the life histories of the individuals comprising each inoculant. The pipette error is approximately 1%, while sampling noise for the initial inoculant of 10,000 cells yields a standard deviation of 100 cells, or 1%.

The variation at later times in all experiments is comparable, although larger in magnitude. For example, in the long term experiment described in section 4.2, the

variation in counts was about 10% from 15-30 days. Even if the total densities in all systems were identical at all times, sampling noise would add variation in measurements across systems. To separate the contribution from sampling noise, a moving average of the counts from each system was considered, with a uniform window of 10 time points, equal to 67 minutes. The 6 minute interval between measurements is assumed to yield independent samples of the overall density. The CV for the moving average is some 12% smaller compared to the CV for the raw counts in the interval considered, as shown in Figure 4.7. This suggests that most of the variation reflects true differences in population densities across systems, so that in this experiment the variation at 30 days was approximately 5 times the magnitude of the initial variation due to pipetting error and sampling noise.

The initial conditions were deliberately varied in the experiments involving nitrogen starvation. The initial period of nitrogen starvation was varied from 1 to 4 days and no large effect was observed over the 30 day acquisition. Replicates with identical initial conditions were not studied, precluding quantitative statements. Nevertheless, the observed dynamics are qualitatively similar for all initial conditions. In contrast, the population dynamics were quite sensitive to the spectrum of the boundary conditions.

To probe further the observed repeatability, we applied perturbations of total darkness of various durations to ecosystems under conditions of nitrogen starvation. When perturbations were applied, large changes in cell density were observed, presumably due to the perturbations themselves. However, an additional interval of large differences was seen around day 7, similar to the dip described in nitrogen starvation, which was probably unrelated to the applied perturbations. The inherent variability of these systems made the interpretation of the perturbation response difficult.

This complication points out a common difficulty encountered in our experiments - namely, the separation of spatial heterogeneity and migration from dynamics due to birth and death. In principle this ambiguity can be addressed by imaging the entire

ecosystem volume - a possibility discussed in chapter 6. The question remains - what can we learn from measuring in an open subvolume within a closed system? Even the "well-behaved" *C. reinhardtii* systems described in sections 4.1 and 4.2 present the same difficulties of spatial heterogeneity and migration.

Restricting measurements of population dynamics to an open subvolume is important for choosing proper perturbations to the ecosystem. Perturbations can be loosely defined as changes which are small with respect to the mean, and in our experimental setup include light and temperature as boundary conditions, and medium composition, starting density, strain history and genotype as the most obvious initial conditions. Although the space of perturbations is huge, it may be difficult to find appropriate perturbations for algal systems and for measurement with our device. As shown, white noise with amplitude as large as 30% of the mean had no measurable effect, while intervals of darkness as short as 9 minutes resulted in large and rapid changes in cell density due to migration. These extremes make sense as just-so stories - algae probably encounter high frequency fluctuations of less than 100% amplitude constantly, and it is unlikely than any adaptive difference exists between strictly constant intensity and fluctuating intensity with identical mean. The extreme sensitivity of *C. reinhardtii*'s system of phototaxis shows that abrupt changes in the direction or intensity of light have ecological consequences for the organism.

Random perturbations in light intensity of small amplitude can still be studied with our devices. It is possible that the spectrum of fluctuations has an effect on the dynamics - in the extreme case, the mean intensity can be varied, which is known to influence population dynamics(1). This could be extended by choosing perturbations of constant total power but with various amounts of power in low frequencies.

The small differences between systems in our experiments suggest pursuing more general questions. The three species ecosystems studied by Hekstra demonstrated differences which increased in magnitude with time, with a roughly linear increase in

the measure of divergence $(\det \Sigma_{ij})^{1/6}(2)$. By 30 days, this measure of divergence had reached a value of roughly 0.75, from an initial value of less than 0.25. In our single species systems, the value of $\sigma(\log n)$ was less that 0.2 from 6 to 30 days, and showed no sign of linear increase with time (Figure 4.14). It is possible that this difference stems from some experimental difference between the measurement techniques; for example, the repeated transfer of samples to the microscope from the incubator could be a significant perturbation to three species ecosystems. However, it is also possible that the stability of one system and the divergence of the other reflects a fundamental difference between their dynamics, possibly due to the relatively simpler species composition of the single species ecosystems. This possibility motivated the experiments described in the next chapter, in which a second species was introduced.

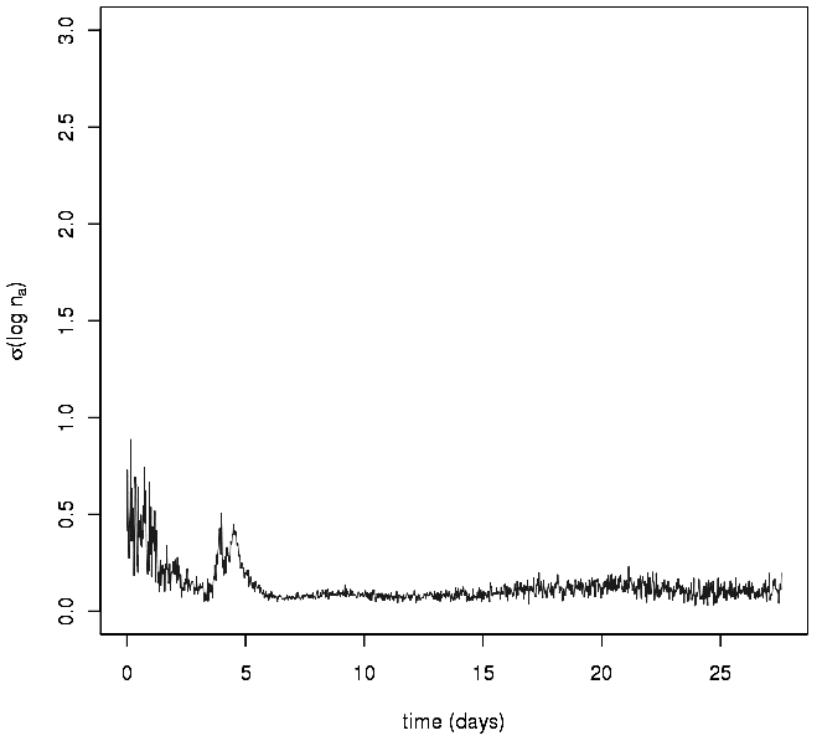

Figure 4.14: Divergence versus time - the standard deviation of $\log n$ is plotted versus time. This metric of divergence is the single species analogue of $(\det \Sigma_{ij})^{1/6}$ for three species systems.

Bibliography

[1] Elizabeth Harris, editor. *The* Chlamydomonas *source book*. Academic Press, San Diego, CA, second edition, 2009. 100

[2] Doeke Hekstra. *Population dynamics in a model closed ecosystem*. PhD thesis, The Rockefeller University, New York, New York, 2009. 101

Chapter 5

Two species systems

Two long term experiments with both *C. reinhardtii* and *T. thermophila* were conducted. In the first, three concentrations of the proteose peptone supplement to the medium were used in an attempt to find conditions yielding densities suitable for DIHM. The dynamics showed a strong correlation in counts between the two species, with a ratio that varied with proteose peptone concentration. The second experiment involved a superior method of sealing cuvettes, as well as an additional supplement to the medium. In this case, population dynamics seemed to fall into one of two categories, correlating with a phenotypic change in the algae observed by DIHM.

5.1 *C. reinhardtii* and *T. thermophila* in compatibility medium

Two experiments were conducted with ecosystems consisting of *C. reinhardtii* and *T. thermophila*. Both experiments used 1/2× Taub #36 medium. In the first experiment, we varied the concentration of proteose peptone (PP) from 0.01% to 0.03% to find good conditions for measurement via DIHM. The cuvettes were sealed by inserting PTFE stoppers into the cuvette ports, a method which we know to produce average evaporation rates of 1-10 mg/day. Eight systems used LEDs with 3200 K spectrum while one used LEDs with 6000 K spectrum. The population dynamics are shown

in Figure 5.1. The strong correlation between counts of the two species struck us as possibly artifactual; however, manual examination of reconstructions from multiple systems from holograms acquired during these intervals confirmed the accuracy of the automatic analysis. No systems tested positive for contamination.

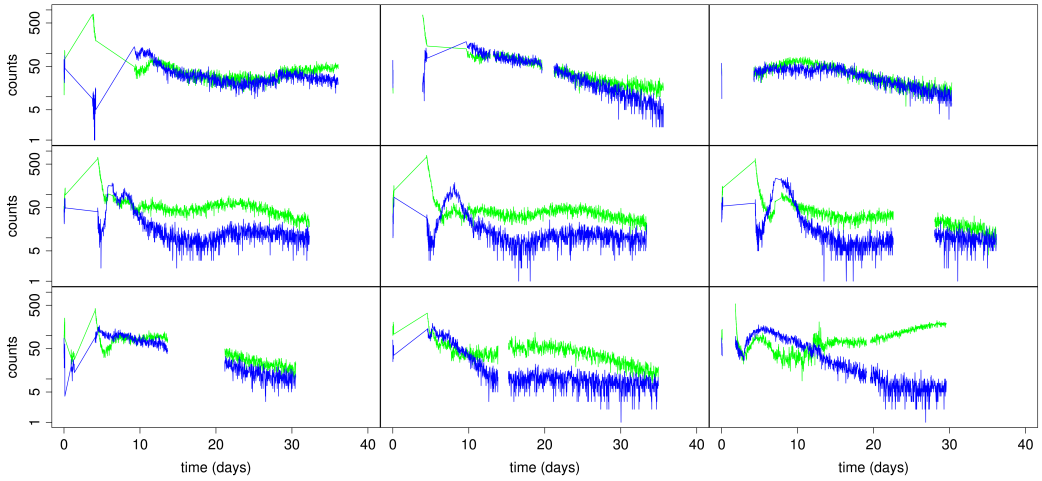

Figure 5.1: Population dynamics from individual two species systems - Population densities measured in 9 systems, with *C. reinhardtii* in green and *T. thermophila* in blue. The medium was 1/2× Taub #36, supplemented with proteose peptone at various concentrations. The proteose peptone concentration was 0.03% for the top row, 0.02% for the second row and 0.01% for the third row. The LED spectrum was 3200 K for all systems except the bottom right, which had 6000 K LEDs. Cuvettes were sealed with PTFE stoppers, allowing evaporation rates over 1 mg/day. Gaps are due to densities exceeding the analysis limit or interruptions in hologram acquisitions.

The correlation between $\log n_{TT}$ and $\log n_{CR}$ was significant for all systems with 3200 K LEDs, as shown in Figure 5.2. For this analysis, a moving average of 10 data points (67 minutes) was considered. The analysis was restricted to the later part of the data, where the counts changed more slowly over time. This included all points after day 3 for 0.03% PP and after day 11 for 0.02% and 0.01% PP. The values of $\mathrm{cor}(\log n_{TT}, \log n_{CR})$ over these intervals were 0.89 for 0.03% PP, 0.41 for 0.02% PP, and 0.59 for the two systems with 0.01% PP and 3200 K LEDs.

T. thermophila cells were seen to increase in size over the later portion of the experiment. Figure 5.4 shows histograms of lateral cell diameter for *T. thermophila*

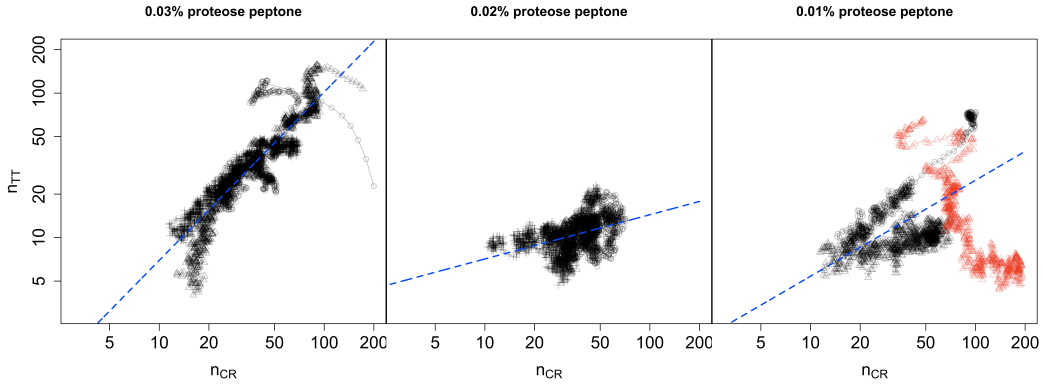

Figure 5.2: Correlation between species - a moving average of counts of *T. thermophila* is plotted against a moving average of counts of *C. reinhardtii* for each of the three concentrations of proteose peptone (PP). The range of the data is restricted to times after day 3 for 0.03% PP, and after day 11 for 0.02% and 0.01% PP. The LED spectrum was 3200 K for all systems except one with 6000 K spectrum, which is plotted in red (not included in fit). Blue lines show the linear fits of $\log n_{TT}$ to $\log n_{CR}$. 0.03% PP: slope 1.16±0.01, intercept -0.742±0.037, $R^2 = 0.79$; 0.02% PP: slope 0.306±0.013, intercept 1.258±0.046, $R^2 = 0.17$; 0.01% PP: slope 0.664±0.023, intercept 0.157±0.084, $r^2 = 0.352$.

over subsequent time intervals for one of the ecosystems. A distinct subpopulation of much larger cells (diameter ∼60 μm) was observed after day 30; these were fused cells, as shown in Figure 5.3. These cells were motile, although it was not clear whether their motion was active or driven by convection. These may be dividing cells or cells attempting to mate. No significant change was observed in size of *C. reinhardtii*.

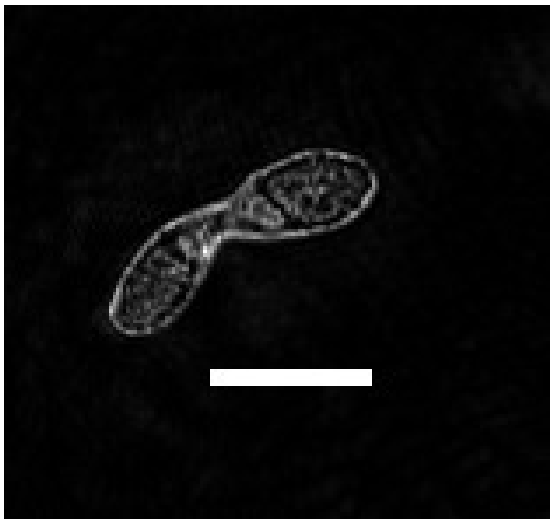

Figure 5.3: Detail of fused *T. thermophila* - two fused cells from day 35 of a system with 0.03% proteose peptone. Cells are located within 100 μm of the proximal cuvette wall. The cells were moving 40 μm/s as measured by reconstructing holograms taken 5 s apart. Scale bar is 50 μm.

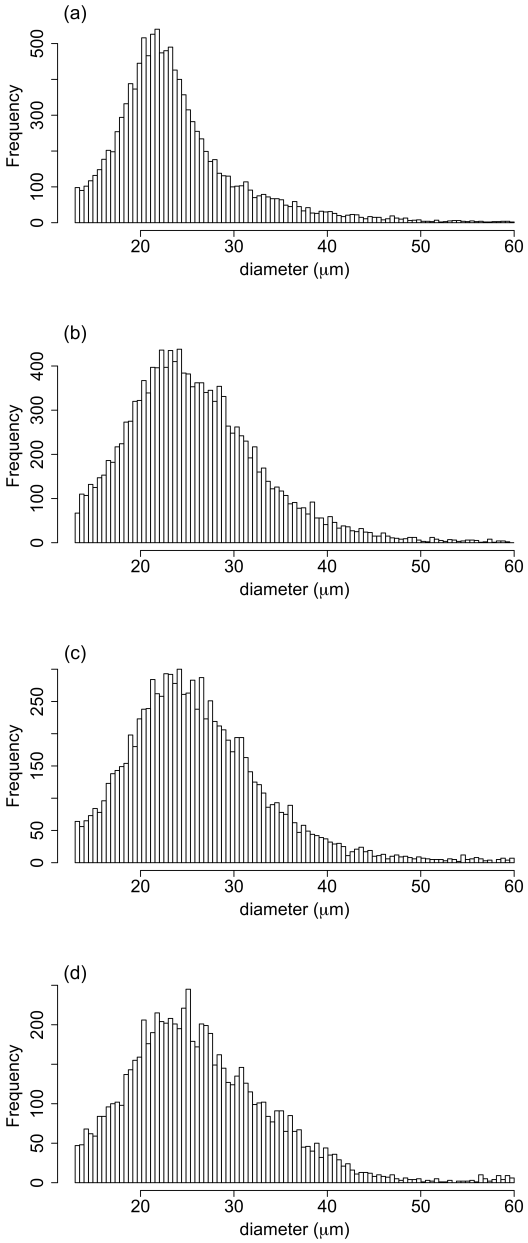

Figure 5.4: *T. thermophila* increase in size - histograms of cell diameter: (a) 9-12 days, (b) 12-21 days, (c) 21-30 days, (d) after 30 days. Proteose peptone supplement was 0.03%. Cuvettes were sealed with PTFE stoppers only.

5.2 *C. reinhardtii* and *T. thermophila* in well-sealed cuvettes

Since all concentrations of proteose peptone resulted in acceptable densities for analysis after a short initial transient, for subsequent experiments we chose 0.03% PP for consistency with the previous experiments of Hekstra(1). We also employed a superior method of cuvette sealing, as we had learned that rates of gas exchange as low as 0.1 mg/day could have a measurable influence of population dynamics(2). However, in the well-sealed conditions, *C. reinhardtii* was seen to decline to very low counts within 4 days. Sealing seemed the most likely culprit, and we reasoned that a major effect of sealing was to reduce the carbon input to the system via CO_2 influx from the atmosphere. To avoid rapid extinction of *C. reinhardtii*, we supplemented the medium with 3 mM acetate, which the algae are known to metabolize. Since acetate metabolism tends to raise the pH, we also added Tris at 20 mM as pH buffer. Note that this is the same medium used for single species experiments with *T. thermophila* described in section 4.5.

The population dynamics measured in this experiment are shown in Figure 5.5. After an initial rapid increase in density of both species, three of the nine systems remained at cell densities above the analysis limit until day 10, while the other six declined to suitable densities around day 4. The three systems with high densities at early times were found to contain large mats or sheets of cells, located in the center of the cuvette and measuring tens to hundreds of micron in lateral dimension (Figure 5.6). These clumps moved very slowly, taking almost 10 days to pass through the imaged volume. After the clumps left the imaged volume, the counts from all 9 systems were comparable: *T. thermophila* counts declined to zero around day 30, and during this decline *C. reinhardtii* counts increased from a minimum of about 30 around day 16 to a maximum of over 100 around day 30. After this interval the *C. reinhardtii* counts

declined by less than a factor 2 over 20 days, followed by an interval of more rapid decrease. No systems tested positive for contamination.

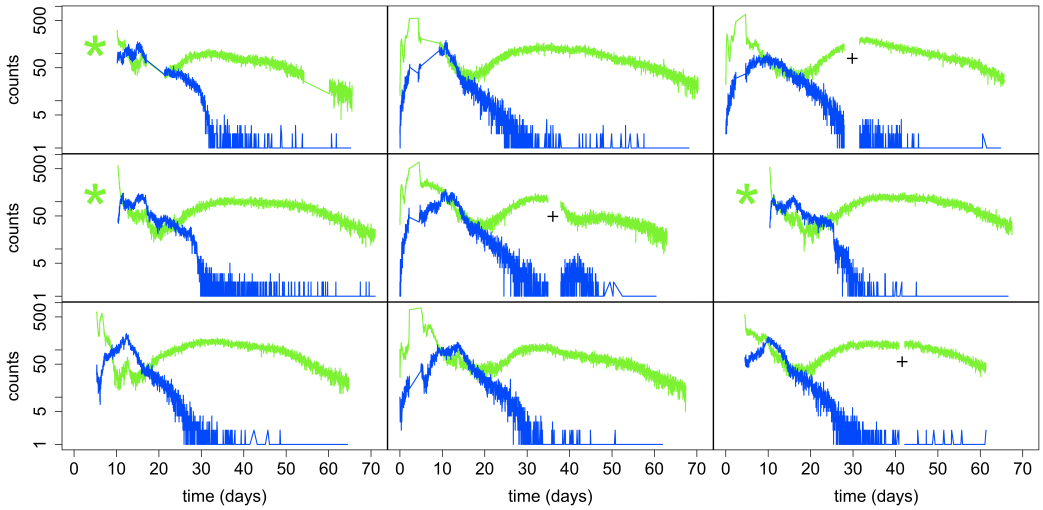

Figure 5.5: Population dynamics from individual well-sealed two species systems - Population densities measured in 9 systems, with *C. reinhardtii* in green and *T. thermophila* in blue. The medium was 1/2× Taub #36, supplemented with 0.03% proteose peptone, 3 mM acetate and 20 mM Tris. Cuvettes were sealed with PTFE stoppers, vacuum grease and epoxy, resulting in evaporation rates typically less than 0.1 mg/day. The presence of large sheets of algae complicated the analysis - 3 systems indicated with green asterisks had large sheets present from day 19.5-28.7, which may interfere with counts of both species in these systems. 3 additional systems briefly had small clumps of 10-100 algae at later times, indicated by black pluses. Remaining gaps are due to densities exceeding the analysis limit.

The correlations observed in the previous experiment were apparently disrupted by sealing or the modifications to the medium. The data after day 9 were considered, since large and rapid changes were observed at early times. Figure 5.7 shows a scatter plot of *T. thermophila* counts against *C. reinhardtii* counts after day 9; the two species are weakly anti-correlated. The correlation of $\log n_{TT}$ and $\log n_{CR}$ after day 9 was -0.44.

T. thermophila cells decreased in size during the experiment. Figure 5.8 shows histograms of lateral cell diameter for *T. thermophila* over subsequent time intervals for one of the ecosystems which did not exhibit clumping of *C. reinhardtii*. The decrease in size may indicate starvation; a similar decrease was observed in single species systems

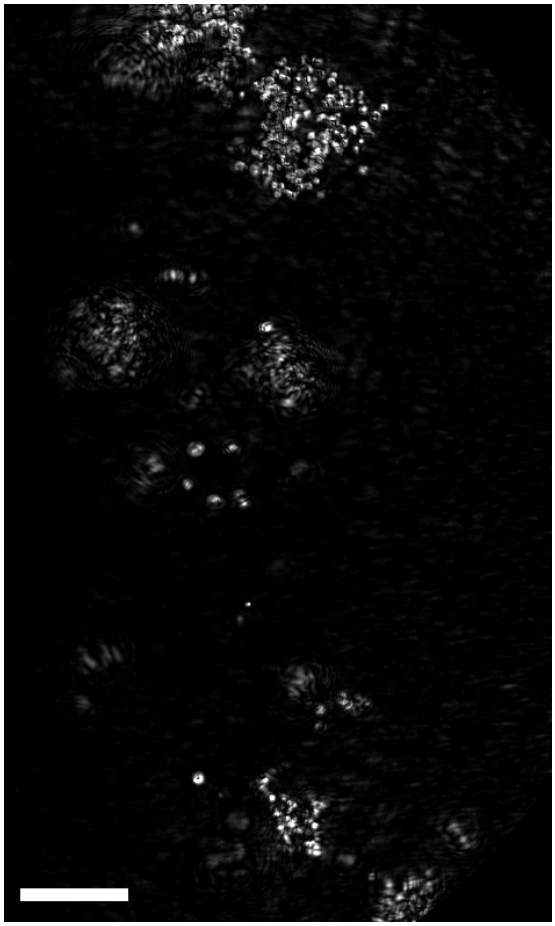

Figure 5.6: Clump of algae from two species ecosystem - reconstruction of clump of algae from experiment with well-sealed ecosystems of *C. reinhardtii* and *T. thermophila*. Hologram was taken at 25.5 days, and reconstruction plane is 2.4 mm from the proximal cuvette wall, almost directly in the cuvette's center along z. Scale bar is 100 μm.

prior to extinction. No significant change was observed in size of *C. reinhardtii* for systems which did not include clumps of cells.

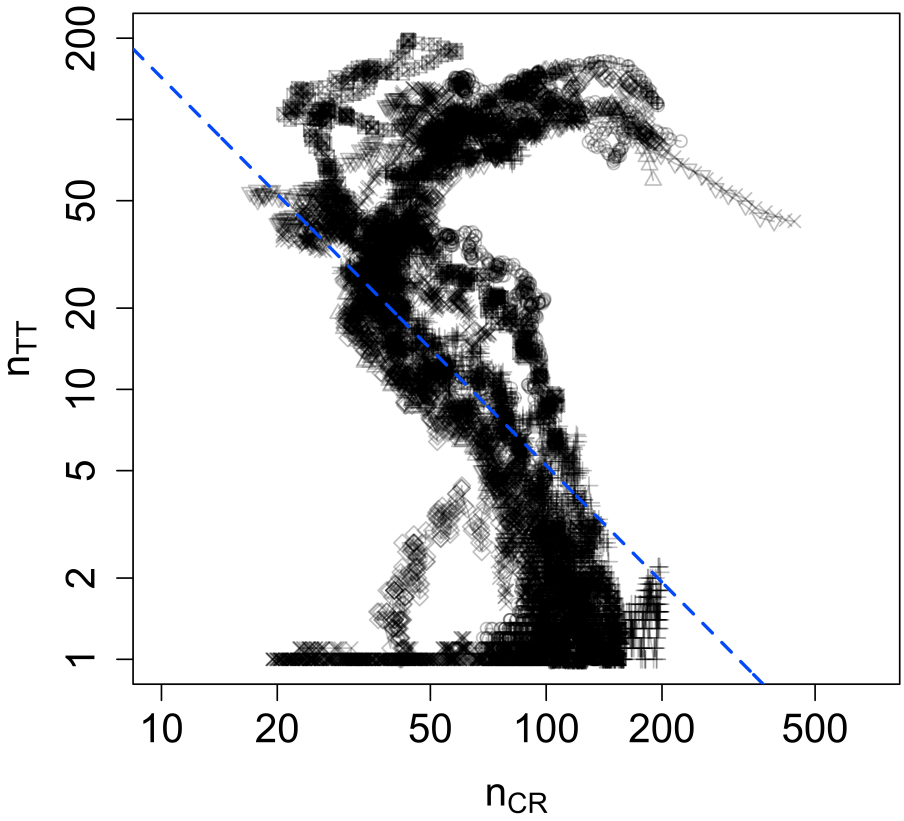

Figure 5.7: Correlation between species in well-sealed cuvettes - a moving average of counts of *T. thermophila* is plotted against a moving average of counts of *C. reinhardtii* for the 9 well-sealed systems in Figure 5.5. The range of the data is restricted to times after day 9. The LED spectrum was 3200 K for all systems. Blue lines show the linear fit of $\log n_{TT}$ to $\log n_{CR}$: slope -1.44±0.03, intercept 8.27±0.12, $R^2 = 0.19$.

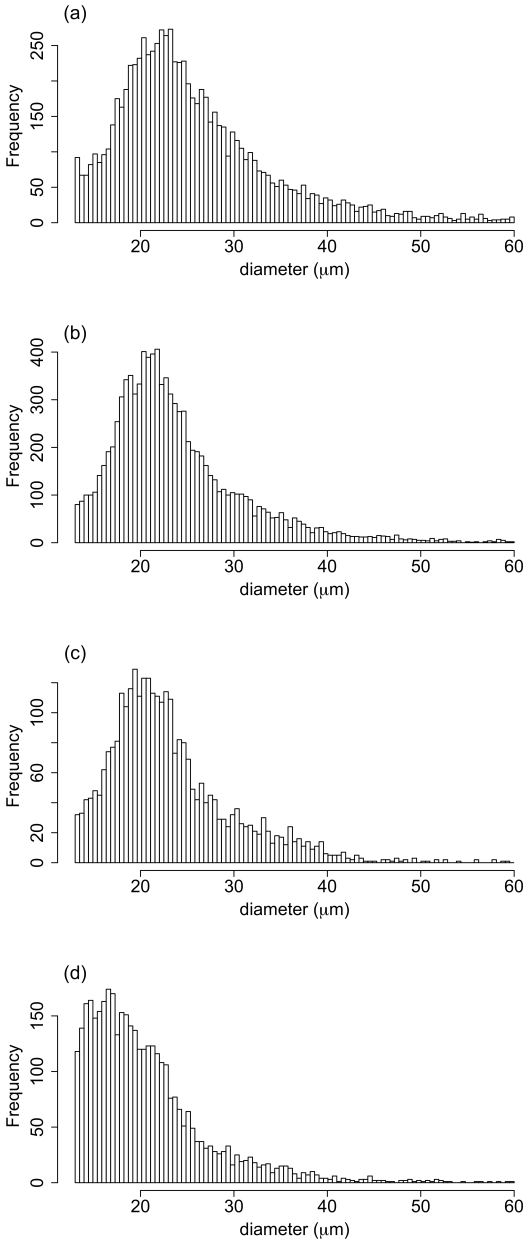

Figure 5.8: *T. thermophila* decrease in size in well-sealed ecosystems - histograms of cell diameter: (a) 9-11 days, (b) 11-14 days, (c) 14-17 days, (d) after 17 days. Medium was supplemented with 0.03% proteose peptone, 3 mM acetate and 20 mM Tris.

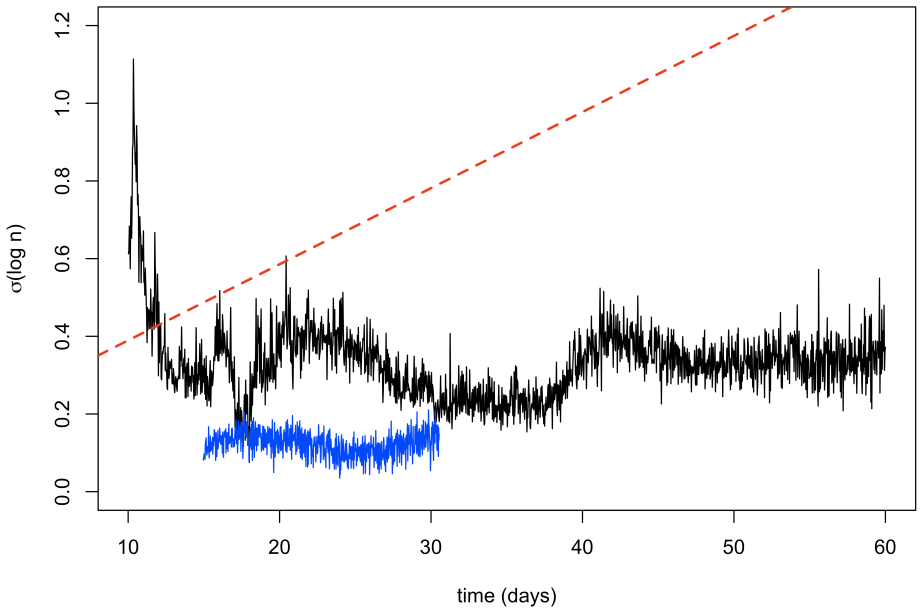

Figure 5.9: Divergence compared between one, two and three species ecosystems - $\sigma(\log n)$ is plotted versus time, in black for *C. reinhardtii* in our two species experiment, and in blue for *C. reinhardtii* in isolation. Counts of *T. thermophila* are not incorporated in this metric due to their disappearance around day 30 in the two species experiment. The red line shows the divergence rate measured by Hekstra for three species ecosystems between days 5 and 70(1). The quantity calculated for three species ecosystems was $(\det \Sigma_{ij})^{1/6}$, which is analogous to $\sigma(\log n)$ for one species.

5.3 Conclusions

The advantages of DIHM for measuring population dynamics extend to ecosystems containing two species. Reconstructed *T. thermophila* and *C. reinhardtii* had similar intensities, with good separation in lateral size.

The repeatability in both experiments for each species was similar to that for single species systems. Since *T. thermophila* counts remained essentially at zero after the first third of the experiment, no attempt was made to measure a two species divergence. The divergence was measured for *C. reinhardtii* alone; $\sigma(\log n_{CR})$ fluctuated between 0.2 and 0.4 after the disappearance of *T. thermophila* (Figure 5.9). While this value is larger than that observed in all single species experiments with constant mean boundary conditions, the divergence does increase with time. It is tempting to speculate that the divergence may increase on average from one to two species systems and increase temporally for three species systems simply due to the increase in the number of species present; however, much work remains to be done to investigate these differences.

Phenotypic differences arose in two species systems, in contrast to the single species systems. Mats of algae appeared in 3 of the 9 replicates with superior sealing. The clumping behavior of *C. reinhardtii* may result directly from the presence of *T. thermophila*, as this phenomenon has been observed in our lab in shaken flasks of Sager Granick medium as well as in microfluidic chambers (ZSF, John Chuang, Seppe Kuehn; independent, unpublished observations). The ramifications of the clumping phenotype are not clear, although observations via brightfield microscopy of samples from flasks containing two species revealed that *T. thermophila* seem to remain in the vicinity of algal clumps, repeatedly passing through them and presumably eating the algae.

A distinct large phenotype of *T. thermophila* has been observed in the presence of *C. reinhardtii* in multiple conditions. In the three species systems of Hekstra, a subpopulation of large *T. thermophila*, roughly twice the linear dimension of the average

cell, were observed in a subset of ecosystems, and these cells tended to be positive for chlorophyll emission, suggesting that the large ciliates are capable of consuming whole algae(1). A subpopulation of large cells, up to ∼80 μm long, full of tens of intact algae were found in samples from shaken flasks containing both species in Sager Granick. In our first experiment, a subpopulation of *T. thermophila* some 50% larger than typical was observed within two weeks, while at later times fusions of these large cells were observed. The larger *T. thermophila* may be capable of consuming *C. reinhardtii*.

In experiments conducted in identical media, the presence of *C. reinhardtii* extended the persistence of *T. thermophila* from 12 days to over 30 days, which may relate to predation and to chemical alterations to the environment by the algae. The strong correlations in population density for the stopper-sealed cuvettes suggest an additional type of interaction between these two species. The ratio of $\log n_{CR}$ to $\log n_{TT}$ was nearly constant over 20 days and an order of magnitude in cell density. In addition, this ratio varied with proteose peptone concentration, while sealing the ecosystems and supplementing with acetate reversed the correlation.

The simple relationship between species in the first experiment is striking. If *T. thermophila* consumed algae in this experiment, we would expect the counts to be anti-correlated. Instead, the strong correlation may indicate a constraint on cell density imposed by the stoichiometry of the metabolism of the two species.

Bibliography

[1] Doeke Hekstra. *Population dynamics in a model closed ecosystem.* PhD thesis, The Rockefeller University, New York, New York, 2009. 108, 113, 115

[2] Doeke Hekstra and Stanislas Leibler. Ecology in replicate: repeatability of population dynamics in closed microbial ecosystems. 2011. In preparation. 108

Chapter 6

Conclusions and future directions

6.1 Conclusions

Closed ecosystems are a convenient model from which high quality spatiotemporal data can be collected at high resolution over time scales of months. Our results demonstrate the importance of precise and statistical characterizations of ecosystem dynamics over long time scales. In single species systems, population dynamics were repeatable in time and space, with barely resolvable differences at ecosystem ages of 30 days. The mechanisms of this repeatability remain unclear, but without making measurements from many replicates for long times the phenomenon could not have been observed. It is likely that the precise control of boundary conditions in these experiments also contributed to the repeatability; although we imposed fluctuations in light intensity, the mean intensity and the temperature were tightly controlled, and both of these parameters influence the population dynamics of algae(3).

Two species systems with identical initial and boundary conditions showed large differences at times of about 1 week, related to an apparently random phenotypic switch of algae from freely swimming to a clumping state. This observation required measurements from a large field of view, as the algal clumps reached several hundred micron in lateral extent, and measuring multiple replicates was crucial to this observation, since only 3 of the 9 systems demonstrated the clumping phenotype at early times. Neither

the clumping phenotype of *C. reinhardtii* nor the long term repeatability of population dynamics of single species systems could have been observed in short experiments.

Spatial heterogeneities were measured as large as 50% across the imaged subvolume, while very high densities are known to be present on the cuvette bottoms from manual inspection. This nonuniformity combined with rapid migration of algae in response to changes in illumination made experiments with perturbations in light intensity difficult to interpret. Perturbations which are localized in time are useful for linear systems, as the impulse response relationship can be directly extracted. Closed ecosystems of motile organisms are not nearly so simple - responses to temporally localized perturbations should be studied by measuring the entire volume, so that by characterizing the spatial reorganization of the population and measuring total population size, several complications are removed and responses may be simpler to interpret. A combination of temporally local perturbations and spectral perturbations to estimate the Wiener kernel were used to characterize the light growth response system of the fungus *Phycomyces*(2, 6, 12), demonstrating the feasibility of such an approach. The shortcomings of our device in this respect motivate the development of techniques for measuring an even larger field of view and the construction of ecosystems of smaller volumes. This approach may also necessitate higher acquisition rates, since responses may be fast - *C. reinhardtii* shows a change in direction in response to a change in light intensity after a lag of less than 1 second(1).

6.2 Future directions

6.2.1 Repeatability

From a dynamical systems perspective, the repeatability we observed in single species systems is a surprising phenomenon. These ecosystems possess many degrees of freedom and several potential sources of nonlinearity in their population dynamics. Such

dynamical systems, when parameterized randomly, often exhibit unstable dynamics(7). From a biological perspective, the interactions determining population dynamics are unlikely to be random, as natural selection may favor certain types of interactions over others. In fact, ecosystem stability itself may be a target of natural selection, and in this case synthetic ecosystems offer the opportunity to observe the transition from the dynamical systems point of view to the biological: ecosystems can be prepared consisting of species which have likely never "seen" each other over evolutionary time scales. These naive systems (Hekstra's three species CES are an example due to their long cultivation as lab strains in isolation) may exhibit instability, as their interspecies interactions are somewhat random and have not been selected. By co-culturing these systems for long times in replicate, we can select any systems which demonstrate long-term coexistence, and use organisms from these systems to initiate replicate CES. If selection acts on ecosystem stability, we expect the population dynamics of these co-cultured strains to be more repeatable relative to those of the naive ancestors.

The mechanism and relevance of the repeatability we observed for single species ecosystems remain unknown. The repeatablity could indicate a dynamical system which, at the times studied, is either convergent, or neither convergent nor divergent, i.e. conservative (Hamiltonian). These possibilities can be tested experimentally by altering the initial conditions by expanding the initial phase space occupied by the systems. For example, one source of initial differences in our experiments is in the number of organisms at time zero - fluctuations which are governed by sampling noise and pipetting error. Assuming it induces no changes in the organisms, a sorting device could be used to prepare ecosystems with exact initial densities, so that in principle replicate ecosystems could be started with exactly equal cell densities, or with controlled amounts of variation. In the latter case, not only the extent of initial variation across systems but also the individual initial densities would be known, allowing the correlation with later differences in population dynamics to be considered.

Besides initial densities, genotype can also be perturbed to investigate repeatability. In our experiments the populations were clonal (*C. reinhardtii*) or at least grown from a single cell (*T. thermophila*). Instead, ecosystems can be prepared from mixtures of various mutants or strains of a single genetically tractable species, and the repeatability of their dynamics measured to test the effect of genetic similarity.

6.2.2 Three component systems

The fluctuations in the three species closed ecosystem studied by Hekstra et al. were shown to grow linearly in time and to undergo a geometric random walk about the mean, with characteristic modes of covariance dubbed "eco-eigenmodes"(5). In our studies of one species ecosystems, no temporal increase in divergence was observed; rather, the differences between systems tended to decrease to remarkably small magnitudes at long times. Two species ecosystems, although not supporting both species for long times, similarly showed no sign of increasing divergence. Nevertheless, the coefficient of variation in these systems was larger than for single species systems, and in one set of experiments, individual systems seemed to find one of two distinct solutions in phenotype space. Together these observations suggest that the number of microbial species may determine qualitative differences in the complexity of population dynamics and adaptation. The relationship between ecosystem composition and richness of population dynamics has been repeatedly studied theoretically(10). This relationship is central to the original motivation for this thesis: namely, that ecological interactions can strongly determine evolutionary paths, and since few populations of organisms evolve in isolation from other species, understanding the population dynamics of multiple species systems is crucial for extending evolutionary theory.

To explore the effects of species composition on population dynamics experimentally, the three species ecosystems studied by Hekstra et al. can be measured using DIHM, which offers two relevant advantages. First, the construction of multiple microscopes

allows replicates to be studied with minimal undesired perturbations imposed by the experimenter, which may play a role in the form and magnitude of observed fluctuations. Second, three species ecosystems exhibited significant spatial heterogeneity, including phenotypic variation with location especially on surfaces; thus measurements of spatial distributions will constitute quantitation of variables which were essentially hidden in previous experiments and are likely to be relevant to overall population dynamics(4).

A major disadvantage of the DIHM technique described here for its application to three species ecosystems is the difficulty identifying multiple species in a single hologram. Using the methods described in this thesis, it is possible to analyze the largest species *T. thermophila* and *C. reinhardtii*, while ignoring the dimmer signal from *E. coli*. Although it is currently possible to measure *E. coli* in isolation, measuring three species simultaneously will require superior filtering of more intense signals or employing an optical technique to enhance scattering from *E. coli*, such as using a shorter wavelength laser(9) or shortening the sample along the optical axis. For the purpose of studying species composition, the lack of fluorescence channels in DIHM may be considered an advantage, since in principle it can be used to measure population dynamics in ecosystems containing species which are not genetically tractable, fluorescently labeled or even uniquely identified.

6.2.3 Evolutionary dynamics

In our single species experiments, we have seen surprisingly long and stable persistence of populations after transition from one medium to another, including conditions with limited nitrogen or carbon. In two species experiments involving putative predator and prey species, phenotypic changes were observed in both species, with the size increase of *T. thermophila* allowing consumption of algae and the large scale clumping of *C. reinhardtii* potentially protecting from predation. In both types of experiment, adaptations to novel environments are apparent within days. Selection of adaptive mu-

tations is unlikely, given the relatively small population sizes and deterministic nature of the populations dynamics. Many mechanisms for phenotypic plasticity are possible, but phenomenological evolutionary and ecological questions remain open. Are ecological adaptations heritable, and do they continue over long time scales? Given the enormous space of possible interspecies interactions and their variability with time, natural selection may have favored general adaptive responses. These issues can be explored by measuring population dynamics of closed ecosystems formed from strains with different histories. For example, lab strains of *T. thermophila* and *C. reinhardtii* can be co-cultured, and at various times after the initial mixing used to initiate closed ecosystems. To study the generality of adaptive responses, one species can be held constant while several choices can be made for the second species.

6.2.4 Whole volume acquisitions

Our implementation of DIHM is limited to measuring in an open subvolume within a larger closed ecosystem. The repeatability in population dynamics and spatial profiles are observed within the subvolume, even in the absence of mixing due to surface growth and sessile subpopulations. Nevertheless, extending observations to cover all or most of the total ecosystem volume would yield several advantages. First, it would allow the separation of net population changes from migrations. This would be especially useful for probing the ecosystem through perturbations in the boundary conditions, which tend to induce migrations on short time scales but may also cause changes in population density on longer time scales. Second, if organisms cannot exit the imaged volume, they can be tracked over their lifetimes. This would in principle allow individual birth and death rates to be measured, as well as provide a microscopic record of physical interactions between individuals. The conic region illuminated with lensless DIHM is not ideal for whole ecosystem measurements, as it is very difficult to create a sample chamber which will be wholly illuminated by the diverging beam without creating

reflections. It may be possible to image most of a cylindrical volume by illuminating with an expanded, circular beam of diameter very close to the ecosystem diameter, and magnifying the resulting fringes with a lens(8).

Tracking individuals requires much faster rates of acquisition than we employed; at a uniform cell density of 10^5 cm^3, the typical intercellular distance is 130 μm, comparable to the distance many microbes swim in 1 second, so that reliable tracking requires acquisition rates faster than 1 Hz at relatively low cell densities. While acquisition of data at these rates is straightforward, the computational requirements for hologram reconstruction and cell tracking are nontrivial. With current graphics cards, entire volumes can be reconstructed in about 1 minute, which is about two orders of magnitude slower than 1 Hz and makes the real time analysis of long term and rapid acquisitions from entire ecosystems in the near future challenging but not impossible.

6.2.5 Large ensembles

Our project increased the number of simultaneous measurement systems to ten. While we emphasize that statistical characterizations of ecosystem dynamics are necessary, the underlying distributions of outcomes are not known. Due to the stochastic nature and very high dimensionality of the mutational process, it may be the case that a huge number of significantly different outcomes are possible from essentially identical initial conditions. Many of these outcomes may be rare. Given the simplicity of the lensless DIHM and the continuing price decrease for high quality image sensors and lasers, it may be possible to construct a very large number of a simplified version of the microscope for studying an ensemble of closed ecosystems. Such a system would offer many opportunities beyond superior statistical sampling of outcomes for fixed conditions; for example, to study the sensitivity of the dynamics to the initial conditions, ecosystems could be prepared with single clones from a large mutant library.

6.2.6 Theory

In chapter 1 I argued that popular theories of ecological population dynamics are either unrealistic or not predictive. The predominant models are based on differential equations for the number of various species comprising an ecosystem, typically containing a specified form for coefficients. These models are often extended to include stochastic effects in the form of additive or multiplicative noise(11). Such models may apply well to certain ecosystems, especially those which fluctuate around an equilibrium state or have strong direct interactions like predator-prey systems. The phenomena observed in our experiments with closed ecosystems do not support this type of description: the dynamics were non-stationary, multiple phenotypes were observed and large scale migrations occurred.

It could be argued that these phenomena are unique to closed ecosystems. For example, non-stationarity can be explained by changes in the chemical environment which accumulate over time, and thus may be strongly dependent on the closure of the ecosystem. However, organisms are in principle capable of influencing their environment whether its boundaries are open or closed. Moreover, by altering the closure conditions of the model ecosystem, the effects of closure can be systematically studied.

"Natural" ecosystems cannot be studied in replicate, their chemical and species compositions are uncertain, their boundaries are difficult to control precisely, and measurements of their population dynamics are typically onerous and disruptive. This is not to say that these systems are irrelevant: the dynamics of specific natural ecosystems may have great importance in an applied sense. For example, fishery management has direct economic importance for industry and food supply, while conservation efforts can influence the extinction of rare species. Regardless, finding general lessons in natural ecosystems remains extremely difficult. If general laws exist in ecology, they must be uncovered by studying replicate model systems which can be easily manipulated.

Bibliography

[1] James S. Boscov and Mary Ella Feinleib. Phototactic response of *Chlamydomonas* to flashes of light - II. Response of individual cells. *Photochemistry and Photobiology*, 30:499–505, 1979. 118

[2] K. W. Foster and Edward D. Lipson. The light growth response of *Phycomyces*. *The Journal of General Physiology*, 62:590–617, 1973. 118

[3] Elizabeth Harris, editor. *The* Chlamydomonas *source book*. Academic Press, San Diego, CA, second edition, 2009. 117

[4] Doeke Hekstra. *Population dynamics in a model closed ecosystem*. PhD thesis, The Rockefeller University, New York, New York, 2009. 121

[5] Doeke Hekstra and Stanislas Leibler. Ecology in replicate: repeatability of population dynamics in closed microbial ecosystems. 2011. In preparation. 120

[6] Edward D. Lipson. White noise analysis of *Phycomyces* light growth response system. *Biophysical Journal*, 15:989–1011, 1975. 118

[7] Robert M May. Will a large complex system be stable? *Nature*, 238:413–414, 1972. 119

[8] Jian Sheng, Edwin Malkiel, and Joseph Katz. Digital holographic microscope for measuring three-dimensional particle distributions and motions. *Applied Optics*, 45:3893–3901, 2006. 123

[9] Dariusz Stramski and Dale A. Kiefer. Optical properties of marine bacteria. In Richard W. Spinrad, editor, *Proceedings of the SPIE - Ocean Optics X*, volume 1302, pages 250–268, 1990. 121

[10] David Tilman. The ecological consequences of changes in biodiversity: a search for general principles. *Ecology*, 80:1455–1474, 1999. 120

[11] Peter Turchin. *Complex population dynamics: a theoretical / empirical synthesis*. Princeton University Press, Princeton, NJ, 2003. 124

[12] Norbert Wiener. *Nonlinear problems in random theory*. John Wiley & Sons, New York, NY, 1958. 118

Chapter 7

Introduction to patterning in *Arabidopsis* roots

The organization of multicellular organisms poses a question for a naive physicist: how is order established and maintained in an organism? Much of developmental biology has investigated this question by studying the transformation of the egg into an adult, and suggests a partial answer: regulatory networks convert simple asymmetries to complex patterns. For example, in *Drosophila*, the most popular model for embryogenesis, maternal cells establish gradients of several morphogens in the developing oocyte, which initiate expression of genes whose regulatory logic results in a segmented pattern governing the body plan of the larva(13, 15).

Patterning does not always depend on the parent; adult organisms can regenerate damaged limbs or organs in species such as *Planaria*, *Hydra*, axolotl and many plants. The phenomenon of regeneration shows that the information specifying pattern persists to the adult stage of development. A range of physical perturbations can induce regeneration, yielding replaced organs essentially indistinguishable from the originals. This generally contrasts with embryogenesis, in which minor perturbations at early developmental stages can lead to gross changes in the mature organism. The convergent nature of regeneration opens many experimental possibilities useful for studying organogenesis; in Waddington's picture of the epigenetic landscape(22), wounding can

be considered a displacement of the organism in a direction orthogonal to time which places the organism in a region of the landscape it would not normally explore in embryogenesis. Regeneration represents the path back to the original equilibrium, and as the magnitude and direction of the displacement can be varied by controlling the physical perturbation, many such paths can be studied experimentally.

The root of the *Arabidopsis thaliana* plant is an attractive model for studying patterning - it is a multi-functional and essential organ with a simple structure, it contains a stem cell niche, and it exhibits total regeneration following excision.

Arabidopsis is a small flowering plant which has become the predominant model organism in plant biology and presents several advantages for laboratory study compared to other organisms exhibiting regeneration. The genome is small for a plant (125 megabases, 25,500 genes) and has been sequenced(6). Transformation is simple and many mutant libraries are available. The generation time of six weeks is relatively short, and adult plants can produce thousands of seeds and are small enough (less than 25 cm) to easily cultivate in the lab. Both the shoot and root of young plants are sufficiently transparent to allow light microscopy of the entire organs, while growing roots move very slowly (few micron per minute), permitting automated sample tracking.

The root system of *Arabidopsis* has been extensively studied as a model for organogenesis, cell biology, gene expression, phenotypic plasticity and ecology. Embryos display a single root, called the primary root, which branches laterally as the plant matures. The root system takes up nutrients and water from the soil or growth substrate, provides structural support, and adapts to the environment by regulating its branching architecture according to nutrient concentrations in the surroundings and within the plant itself.

Regions of the root are labelled geographically from the center of the plant, so that the tip is the most distal part of the root. The *Arabidopsis* root apical meristem, spanning the most distal 250 μm of the primary root, consists of longitudinal files

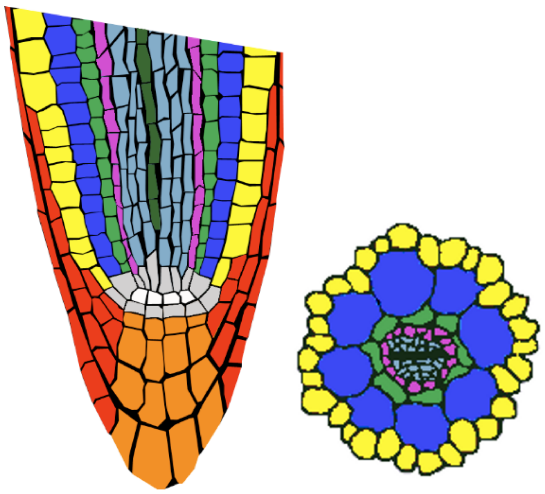

Figure 7.1: *Arabidopsis* root tissue organization - Cartoon showing longitudinal and cross sections. Color distinguishes tissue type: red - lateral root cap, orange - columella, yellow - epidermis, dark blue - cortex, green - endodermis, purple, light blue and dark green - stele, grey - initials, white - quiescent center. The root diameter is about 100 μm.

of cells of various tissues, organized in a radially symmetric pattern, as depicted in Figure 7.1. Six tissue types can be distinguished by histology, embryonic origin(17), and gene expression profile(2): columella, lateral root cap, stele, endodermis, cortex, and epidermis. The organization of the root apical meristem is consistent - for example, the number of cortical cells in a transverse section taken 1mm from the primary root tip was exactly 8 in 40 roots studied(5).

The files of cells of common tissue type converge on a group of cells called initials, located approximately 70 μm from the tip of the root. In general, the initials divide asymmetrically, with one daughter forming the distal edge of the corresponding column of differentiated tissues, and the other daughter replenishing the mother initial. Because plant cells do not migrate, the orientation of the divisions of the initials is sufficient to establish the root's pattern, and the distance of a cell along a file to its initial reflects the time since differentiation. The initials border 4 to 7 cells of much lower mitotic activity known as the quiescent center, which are thought to maintain the adjacent initials in an undifferentiated state(21). Initials do not divide indefinitely;

rather they eventually differentiate and are replaced by asymmetric divisions in the quiescent center(5). There is some disagreement in the literature over whether the initials or the cells in the quiescent center satisfy various definitions of stem cells(12). To avoid semantic controversies, the loose term "stem cell niche" can be applied to the initials together with the quiescent center.

The *Arabidopsis* plant exhibits several developmental processes related to regeneration. Postembryonic *Arabidopsis* plants form lateral roots - whole organs derived from a small group of differentiated cells(14). When transferred to certain media, single differentiated plant cells form an undifferentiated mass of proliferating cells called the callus, which can in turn be hormonally induced to produce roots, shoots, or whole plants(9, 19). Laser ablation of the quiescent center causes proximal, differentiated cells from the vasculature to invade and respecify the quiescent center(20). This suggests that position is more important than lineage in establishing cell fate, a conclusion reinforced by work showing that regeneration upon ablation requires transcription factors regulating expression of proteins involved in auxin transport(23). Upon surgical excision of the root tip, the majority of roots regenerate within 7 days - examples are shown in Figure 7.2(18).

The work in this thesis focused on developing a technique for making quantitative observations of root apical meristem regeneration following surgical excision, so this regenerative process will be reviewed here. In experiments involving hundreds of roots, competence for regeneration extended to excisions made as far as 200 μm from the distal tip, although the frequency of regeneration for such cuts was only 10%, and no regeneration was observed after cuts at 270 μm(18). Regeneration was blocked by inhibition of progression through the cell cycle, suggesting that cell divisions are required for regeneration(18). Global transcriptional analysis for cell type specific profiles(2) showed that transcriptional signatures of excised cell types reappeared by 5 hours after cutting, with total reversion by 7 days(18). Most cut roots regained the gravitropic

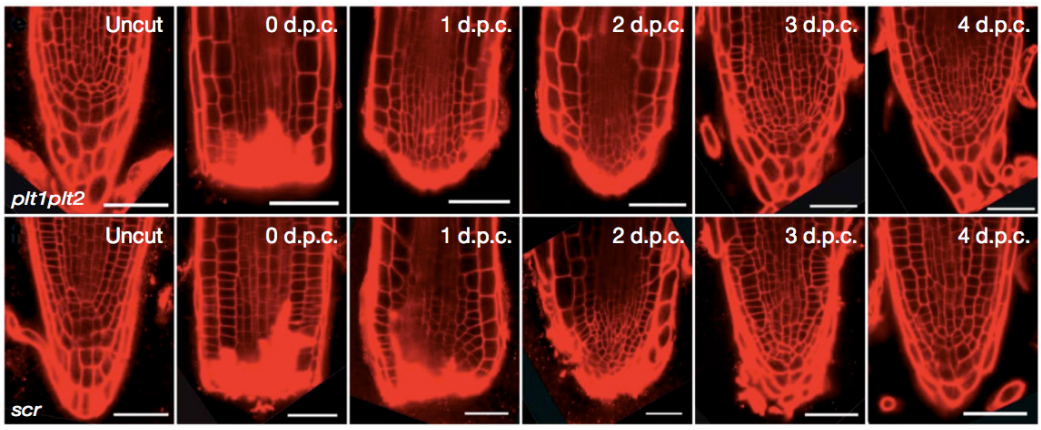

Figure 7.2: Confocal images of *Arabidopsis* root regeneration - Top row shows time series of regeneration in a *plt1plt2* double mutant before cut, immediately post cut, and at 1, 2, 3 and 4 days post cut (d.p.c.); bottom row shows regeneration of *scr* mutant. Membranes are stained with propidium iodide. Scale bars 50 μm. Figure taken from Sena et al. 2009(18)

response within 3 days of excision(18).

Several mutants exist in which the stem cell niche is not maintained yet roots are formed and grow very slowly(1, 16). Two sets of these, *plt1 plt2* and *scr* were capable of regeneration after cuts made 70 and 130 μm from the root tip, although at lower frequency than the wild type(18) (Figure 7.2). Despite its role in patterning the normally growing root, the stem cell niche is not required for repatterning after cutting. It is not clear whether regeneration requires reestablishment of a quiescent center before repatterning, and the lineages of cells forming distinct tissues in the regenerated root are not known. Although these questions could be addressed using genetic markers, it is possible that regeneration involves the entire meristem rather than specific cells. The goal of this thesis was to better understand the dynamics of regeneration by imaging the root apical meristem both before and after excision, at cellular resolution (microns) and temporal frequency sufficient to observe all cell divisions (<30 min) for duration sufficient to observe complete regeneration (7 days).

Several techniques involving time-lapse microscopy in plants have been developed for studies of organogenesis, mostly employing laser scanning confocal microscopy. Mea-

surements of PINFORMED1, a protein effecting auxin efflux, in the primordium of the shoot apical meristem every 2 hours for 40 hours were used to propose a mechanism for auxin transport to determine cell type(10). A method of acquiring 3D confocal scans at several angles was used to track cell lineages through several divisions during early flower development and quantitatively describe the patterns of growth of various tissues(7).

Cell divisions of initials in the root apical meristem were observed by acquiring 2D median sections every 10 minutes for up to 28 hours(3). This data showed that the rate of division in initials of the lateral root cap/epidermis and columella initials was significantly lower than that of cells in the proximal meristem. There was not significant synchrony on the cell divisions of the two types of tissue, indicating that the patterning of the root apical meristem does not solely result from simple coincident division of neighboring initials, but the data set was not sufficiently large to propose a specific mechanism. A small number of cell divisions conflicted with the proposed strict ordering of orientation by physical location.

3D confocal imaging of cell walls along with cell cycle markers for specific cell fates demonstrated that regeneration upon cutting did not depend on a stem cell niche(18). However, the temporal resolution of 1 day was insufficient to track cell lineages or observe all cell divisions.

Exposure of live samples to high intensity light for excitation in fluorescence microscopy causes photobleaching of dye molecules and phototoxicity by production of reactive oxygen species(4). At constant total irradiance per acquisition, shorter exposures at higher excitation intensity cause more damage. Avoiding excitation induced damage throughout an experiment constrains imaging frequency and duration. The constraints are particularly restrictive for laser scanning confocal microscopy, because to scan many points in a reasonable temporal interval, exposure times must be very short (typically μs), while every point in the sample along the optical axis is excited

per exposure.

An alternative method is to excite along an axis orthogonal to the collection axis, and focus the excitation beam into a thin sheet which coincides with the focal plane of the collection objective, variously known as selective plane illumination microscopy (SPIM) or thin light sheet microscopy (LSM)(8, 11). Samples can be imaged in three dimensions by scanning along the optical axis. This method avoids exciting regions of the sample outside of the focal plane, and therefore reduces the total light dosage by a factor equal to the number of slices per scan compared to confocal microscopy. Since LSM does not involve scanning laterally, exposure times can be increased by several orders of magnitude compared to confocal, allowing rapid acquisition of images at an irradiance some four orders of magnitude lower.

Bibliography

[1] Mitsuhiro Aida, Dimitris Beis, Renze Heidstra, Viola Willemsen, Ikram Blilou, Carla Galinha, Laurent Nussaume, Yoo-Sun Noh, Richard Amasino, and Ben Scheres. The *PLETHORA* genes mediate patterning of the *Arabidopsis* root stem cell niche. *Cell*, 119:109–120, 2004. 130

[2] Kenneth Birnbaum, Dennes E. Shasha, Jean Y. Wang, Jee W. Jung, Georgina M. Lambert, David W. Galbraith, and Philip N. Benfey. A gene expression map of the *Arabidopsis* root. *Science*, 302:1956–1960, 2003. 128, 129

[3] Ana Campilho, Bernardo Garcia, Henk v.d. Toorn, Henk v. Wijk, Aurélio Campilho, and Ben Scheres. Time-lapse analysis of stem-cell divisions in the *Arabidopsis thaliana* root meristem. *The Plant Journal*, 48:619–627, 2006. 131

[4] Ram Dixit and Richard Cyr. Cell damage and reactive oxygen species production induced by fluorescence microscopy: Effect on mitosis and guidelines for non-invasive fluorescence microscopy. *The Plant Journal*, 36:280–290, 2003. 131

[5] Liam Dolan, Kees Janmaat, Viola Willemsen, Paul Linstead, Scott Poethig, Keith Roberts, and Ben Scheres. Cellular organisation of the *Arabidopsis thaliana* root. *Development*, 119:71–84, 1993. 128, 129

[6] *Arabidopsis* Genome Initiative. Analysis of the genome sequence of the flowering plant *Arabidopsis thaliana*. *Nature*, 408:796–815, 2000. 127

[7] Romain Fernandez, Pradeep Das, Vincent Mirabet, Eric Moscardi, Jan Traas, Jean-Luc Verdeil, Grégoire Malandain, and Cristophe Godin. Imaging plant growth in 4D: Robust tissue reconstruction and lineaging at cell resolution. *Nature Methods*, 7:547–553, 2010. 131

[8] Eran Fuchs, Jules S. Jaffe, Richard A. Long, and Farooq Azam. Thin laser light sheet microscope for microbial oceanography. *Optics Express*, 10:145–154, 2002. 132

[9] Sean P. Gordon, Marcus G. Heisler, G. Venugopala Reddy, Carolyn Ohno, Pradeep Das, and Elliot M. Meyerowitz. Pattern formation during de novo assembly of the *Arabidopsis* shoot meristem. *Development*, 134:3539–3548, 2007. 129

[10] Marcus G. Heisler, Carolyn Ohno, Pradeep Das, Patrick Sieber, Gonehal V. Reddy, Jeff A. Long, and Elliot M. Meyerowitz. Patterns of auxin transport and gene expression during primordium development revealed by live imaging of the *Arabidopsis* inflorescence meristem. *Current Biology*, 15:1899–1911, 2005. 131

[11] Jan Huisken, Jim Swoger, Filippo Del Bene, Joachim Wittbrodt, and Ernst H. K. Stelzer. Optical sectioning deep inside live embryos by selective plane illumination microscopy. *Science*, 305:1007–1009, 2004. 132

[12] V. B. Ivanov. The problem of stem cells in plants. *Russian Journal of Developmental Biology*, 34:205–212, 2003. 129

[13] Edward B. Lewis. A gene complex controlling segmentation in *Drosophila*. *Nature*, 276:565–570, 1978. 126

[14] Jocelyn E. Malamy and Philip N. Benfey. Down and out in *Arabidopsis*: The formation of lateral roots. *Trends in Plant Sciences*, 2:390–396, 1997. 129

[15] Christiane Nüsslein-Volhard and Eric Wieschaus. Mutations affecting segment number and polarity in *Drosophila*. *Nature*, 287:795–801, 1980. 126

[16] Ben Scheres, Laura Di Laurenzio, Viola Willemsen, Marie-Therès Hauser, Kees Janmaat, Peter Weisbeek, and Philp N. Benfey. Mutations affecting the radial organisation of the *Arabidopsis* root display specific defects throughout the embryonic axis. *Development*, 121:53–62, 1995. 130

[17] Ben Scheres, Harald Wolkenfelt, Viola Willemsen, Maarten Terlouw, Emily Lawson, Caroline Dean, and Peter Weisbeek. Embryonic origin of the *Arabidopsis* primary root and root meristem initials. *Development*, 120:2475–2487, 1994. 128

[18] Giovanni Sena, Xiaoning Wang, Hsiao-Yun Liu, Hugo Hofhuis, and Kenneth D. Birnbaum. Organ regeneration does not require a functional stem cell niche in plants. *Nature*, 457:1150–1153, 2009. 129, 130, 131

[19] F. C. Steward, Marion O. Mapes, and Kathryn Mears. Growth and organized development of cultured cells. II. Organization in cultures grown from freely suspended cells. *American Journal of Botany*, 45:705–708, 1958. 129

[20] Claudia van den Berg, Viola Willemsen, Willem Hage, Peter Weisbeek, and Ben Scheres. Cell fate in the *Arabidopsis* root meristem determined by directional signalling. *Nature*, 378:62–65, 1995. 129

[21] Claudia van den Berg, Viola Willemsen, Giel Hendriks, Peter Weisbeek, and Ben Scheres. Short-range control of cell differentiation in the *Arabidopsis* root meristem. *Nature*, 390:287–289, 1997. 128

[22] Conrad Hal Waddington. *Principles of Embryology*. George Allen & Unwin, Ltd., London, 1956. 126

[23] Jian Xu, Hugo Hofhuis, Renze Heidstra, Michael Sauer, Jiří Friml, and Ben Scheres. A molecular framework for plant regeneration. *Science*, 311:385–388, 2006. 129

Chapter 8

Methodology for live imaging of *Arabidopsis* roots

This chapter describes the device used to image growing *Arabidopsis* roots in three dimensions at cellular resolution at a time scale of minutes for several days. Descriptions of the sample chamber and continuous perfusion chamber are included. The algorithms used to track the growing root, process the images and track identified nuclei through time are presented and evaluated. All source code is available as a SourceForge project called **qanneal-celltrk** at `http://qanneal-celltrk.sourceforge.net/`.

8.1 Thin light sheet microscopy

The principle of thin light sheet microscopy is to achieve optical sectioning by illuminating orthogonally to the collection axis. The use of light sheets goes back to at least the early 20^{th} century, when a light sheet was used to image colloidal particles in a device dubbed the ultramicroscope(26). Many extensions to fluorescence imaging of biological samples have been made. A simple setup involving an expanded laser beam and cylindrical lens was used to image dense suspensions of seawater(9). Separate implementations of this technique were used to measure population dynamics in closed microbial ecosystems in three fluorescence channels(11), and to image both fixed and live Medaka fish as well as live *Drosophila* embryos(14). By mounting the excitation

optics to the collection optics, Holekamp et al. were able to image calcium sensitive dyes in populations of neurons as fast as 200 Hz(12). All of these techniques benefit from the reduced photobleaching and faster acquisition rates compared to confocal fluorescence microscopy, as excitation is restricted to the focal plane and scanning is only necessary in the axial dimension.

The technique has been extended to achieve superior resolution and penetration depth. Buytaert and Dirckx achieved an axial excitation resolution of 2.6 μm (full width at half maximum) by using a large numerical aperture cylindrical lens(3). This can be considered a line rather than a sheet, and samples were scanned in two dimensions, along both optical axes. Keller et al. used a light line technique with scanning along the optical axis of the collection axis as well as along the vertical axis (perpendicular to both optical axes) to achieve much higher illumination efficiency compared to light sheet techniques and to reduce aberrations in the excitation profile(16). A laser scanner coupled to an f-theta lens and focused by a tube lens and objective was used to excite fluorescence from a line which was rapidly scanned through a developing zebrafish embryo. A rotation stage was used to rotate the sample so that images could be acquired from two opposite directions, improving the overall resolution and depth of tissue from which data could be collected.

In choosing technical parameters for our setup, the predominant constraint was to avoid photodamage to normally growing and regenerating roots; optimizations for penetration depth were unnecessary thanks to the root's small size and low optical density, the acquisition period of several minutes necessary to observe mitotic events is modest compared to imaging neuronal activity, and axial resolution sufficient to resolve neighboring cells in the root is readily achieved with a simple optical setup. Thus our implementation of the microscope is most similar to those described by Fuchs et al. and Huisken et al.(9, 14). The numerical aperture of the excitation sheet was chosen to yield sufficiently high resolution for separating nuclei over the extent of the root along

the optical axis of the sheet.

8.2 Experimental setup

8.2.1 Optics

The microscope is depicted schematically in Figure 8.1. An 80 mW 473 nm diode pumped solid state laser (Lasever, Ningbo, China) or a 60 mW Argon laser (Spectra Physics, Irvine, CA) is filtered by an excitation filter (Chroma) and optional neutral density filter (Thorlabs, Newton, NJ) and modulated by a Pockels cell electro-optic modulator (350-50, Conoptics, Danbury, CT) powered by a custom circuit coupled to the CCD camera exposure gate. The beam is directed into a 10× Galilean beam expander (Thorlabs), shaped by a 9 mm circular iris and focused in the z dimension by a cylindrical lens (f=30 mm, Thorlabs). A 20× super long working distance objective (NA=0.35, f=19.9 mm, Nikon) collects emission through a fluorescence filter (Chroma) onto a cooled CCD camera (1392 × 1024, 4.65 μm square pixels, 12-bit QICam, QImaging, Surrey, British Columbia, Canada). The tube length of the objective is adjusted to partially compensate for spherical aberration caused by imaging through interfaces, so that the actual magnification is 19×.

The coordinate axes are depicted in Figure 8.1: the x axis coincides with the optical axis of the cylindrical axis, the y axis is parallel to gravity, and the z axis coincides with the optical axis of the objective. The sample is positioned in the coincident foci of the cylindrical lens (the light sheet) and the objective by 3 translation stages on which the sample holder is mounted (travel in x, y and z) and 2 translation stages coupled to the CCD camera and objective (x and z). The stages are positioned by micrometers driven by servo motors (25 mm travel, 40 nm resolution, Thorlabs) controlled by a computer.

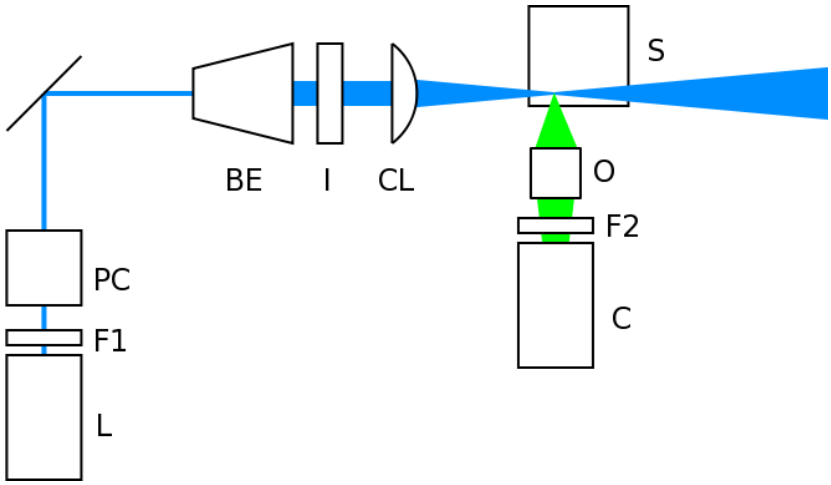

Figure 8.1: Schematic of TLSM optics - (L) laser, (F1) neutral density and excitation filters, (PC) Pockels cell, (BE) beam expander, (I) circular iris, (CL) cylindrical lens, (S) sample chamber, (O) objective, (F2) emission filter, (C) camera.

8.2.2 Sample chamber

Methods employing orthogonal illumination require embedding of the optics or two perpendicular transparent surfaces of optical quality. Concerns regarding contamination led us to forego embedding; instead, we chose fluorometer cuvettes with four polished windows to house the sample (inner dimensions 10 × 10 × 40 mm, Starna, Atascadero, CA). Although our routine for sample tracking allowed large three dimensional displacements of the sample within the chamber, it was found that unconstrained roots often grew with the tip oriented at large angles from gravity, resulting in orientations in which the penetration depth of the light sheet or the collection of emission were much greater than the root diameter. To restrict the root to the corner of the cuvette, a glass capillary tube (outer diameter 1.5 mm, Fisher) was placed vertically within the cuvette, forming a channel with two flat perpendicular walls and one concave round wall, a geometry which can accommodate a cylinder with diameter approximately 300 μm (Figure 8.2). To allow exchange of medium between the sample channel and the rest of the cuvette, the ends of the capillary tube are wrapped with two PTFE collars 80 μm thick. The cuvette is filled with 3 mm glass beads (Fisher) to maintain the

capillary tube into the corner while creating multiple channels for medium.

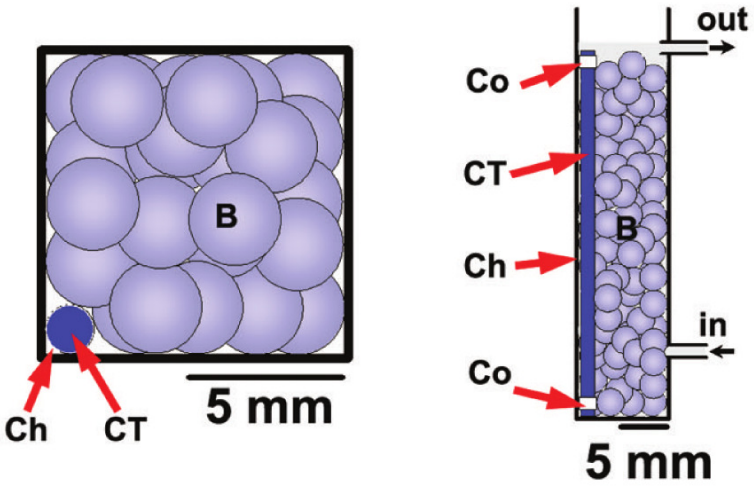

Figure 8.2: Schematic of sample chamber - (Ch) channel containing root, (CT) capillary tube, (B) glass bead, (Co) PTFE collar, arrows depict flow of medium.

The top of the cuvette is sealed with a custom top cap, designed to provide gas exchange, sterile conditions, and transparent windows for illumination of the plant leaves. The cap is made from a plastic spectrophotometer cuvette (inner dimensions 10 × 10 × 40 mm, whose three long sides have been cut and sealed with adhesive breathable sealing tape for gas exchange (Nunc). The base of the cap is cut and replaced with a glass coverslip for illumination of the plant leaves. The junction of the cap to the cuvette is sealed by wrapping with Parafilm.

The 3 to 7 day old plant is transferred to the sample chamber from agar plates under a sterile hood. The corner of the chamber in which the root will grow is wetted with medium, the plant root is placed in the corner using forceps, the capillary tube is used to force the root into the corner and the glass beads are added to keep the tube in place. It was found that increasing the humidity of the air under the hood with a humidifier increased the success rate of sample preparation as measured by root growth.

8.2.3 Growth conditions

An array of 12 bright white LEDs (Luxeon Star/O, Philips Lumileds Lighting Company, San Jose, CA) powered by a current source controlled by the computer illuminate the sample from above. The LED current is gated by the camera exposure signal to prevent imaging LED signal during acquisition. The optics and sample chamber are housed within a light tight box with a hinged door, thermally insulated with polystyrene foam. A thermoelectric assembly (AC-046, TE Technologies, Inc., Traverse City, MI) maintains constant temperature within the box.

Preliminary experiments in sealed cuvettes resulted in gradual decline of fluorescence intensity and root growth over time scales of hours, presumably due to the root exhausting the oxygen dissolved in the medium. In an attempt to overcome the decline in fluorescence intensity and maintain constant root growth, we developed a chamber which provides good optical qualities for imaging while allowing the medium to be continuously replaced.

Perfusion of liquid medium is maintained through the sample chamber by two peristaltic pumps (Dynamax RP-1, Rainin, Oakland, CA). One pump run at 30 rpm with 0.51 ID tubing (Pharmed BPT, Cole Parmer, Vernon Hills, IL) flows medium from a 4 L reservoir to the bottom of the sample chamber, while another pump run at the same speed with 0.89 mm tubing removes medium from the top of the chamber, just below the platlet's hypocotyl, to a waste bottle. The flow differential prevents flooding of the chamber. The medium is 1/4× Murashige and Skoog (MS) basal medium, enriched with Gamborg's vitamins (Sigma), 3.0% sucrose, 0.05% MES buffer (Sigma), and adjusted to pH 5.7 with potassium hydroxide. The medium is sterilized in an autoclave, then supplemented with antibiotic and antimycotic solution (A5955, 1/200×, Sigma) and Amphotericin B (A9528, 1.0 mg/L, Sigma). Preliminary experiments were often frustrated by contamination by bacteria in the medium within the sample chamber, and by fungus on the plant leaves. The addition of antibiotic and antimycotic solution

was successful in preventing contamination in all subsequent experiments, while the concentration used resulted in rates of root growth and maintenance of fluorescence intensity comparable to those from experiments without antibiotic solution. An aquarium air pump bubbles filtered air through the medium in the reservoir to ensure oxygen saturation.

8.2.4 Image acquisition

The root tip is positioned in the focus of the excitation sheet. The stage is repositioned to coincide with the collection optics by searching manually without the emission filter. The focal plane of the objective is determined by exciting fluorescence from a central region of the root while acquiring images from several positions along the optical axis of the objective. The sum of the spatial gradient at all pixels is calculated, and the position which achieves the maximum value is chosen as the focused position. The root is then scanned in the z dimension by repeatedly stepping the stages and exposing for 25-50 ms. Typically 2 $\times$ 2 pixel binning is used, and averaging several images taken in immediate succession at the same z position at correspondingly shorter exposure times can improve image quality by suppressing read noise from the camera compared to acquiring a single image. For each displacement of the sample in z by Δ, the collection optics are moved by $(n_{water} - n_{air})\Delta$ to maintain the sample focus.

The sectioning interval is typically set at 2.5 μm or less to satisfy the Nyquist criterion for the measured point spread function. Oversampling at 1.25 μm is useful for deconvolution (see section 8.4.1). To capture the entire root regardless of its orientation, a depth larger than the root itself is scanned (typically 200 μm).

The scan duration (typically 90 s) is limited by the time to reposition the motorized stages. After each scan completes, the stage is moved to place the imaged region of the root 1 mm along the z axis from the focus of the light sheet, so that the residual light passing the Pockels cell will not strike the root during the interim between scans.

Scans were typically acquired every 10 minutes.

8.2.5 Resolution

To first approximation, the lateral resolution is determined by the numerical aperture of the collection objective according to the Rayleigh criterion: $d = 0.61\lambda_{em}/NA_{obj}$, where λ_{em} is the emission wavelength. For our setup the lateral resolution is somewhat compromised by spherical aberration caused by the presence of water-glass and glass-air interfaces, although this has been compensated to some degree by shortening the tube length of the objective. Regardless, the actual resolution is sufficient to separate nearby nuclei, which are typically at least 3 μm apart. The axial resolution is determined by the numerical aperture of the collection objective and the properties of the light sheet(7). The objective's depth of field is given by $d_f = 0.61\lambda_{em}/NA_{obj}^2$ while the sheet thickness in the axial dimension at its focus is given by $d_s = 0.61\lambda_{ex}/NA_{cyl}$. For our implementation the values are $d_f = 2.6\,\mu$m and $d_s = 2.1\,\mu$m, assuming a YFP marker ($\lambda_{em} \approx 530\,$nm) excited with 514 nm laser light.

Spherical aberration of the excitation sheet will degrade its focus, and the sheet thickness varies away from the focus, so to fully characterize the axial resolution, we measured the sheet intensity as a function of x and z by scanning 0.3 μm diameter fluorescent beads (Duke Scientific) embedded in 0.5% Phytagel (Sigma-Aldrich). A fit to a Gaussian function was used to calculate the full width at half maximum (FWHM) for each x coordinate, revealing that the mean FWHM over the 180 μm region of interest was 4.2 $\pm$ 0.2 μm. This thickness allows sectioning over the entire diameter of the root with cellular resolution. Scattering from inhomogeneities in the sample degrade the quality of the sheet focus; as shown in section 8.4.2, the primary effect is attenuation of intensity, while resolution remains sufficient to separate neighboring nuclei.

8.2.6 Photoenergy

Since orthogonal illumination schemes restrict excitation to the focal plane, the reduction in total energy load is reduced by a factor equal to the number of sections compared to confocal or two photon microscopy with other parameters equal. Since point scanning is avoided, the irradiance in the focal plane is reduced by four orders of magnitude compared to confocal laser scanning microscopy: 57 W/cm^2 compared to 950 kW/cm^2 for values calculated from actual acquisitions of data from *Arabidopsis* roots with equivalent parameters. The reductions in excitation levels allows long term and frequent acquisitions without significant photobleaching or phototoxicity, as shown in Figure 8.3.

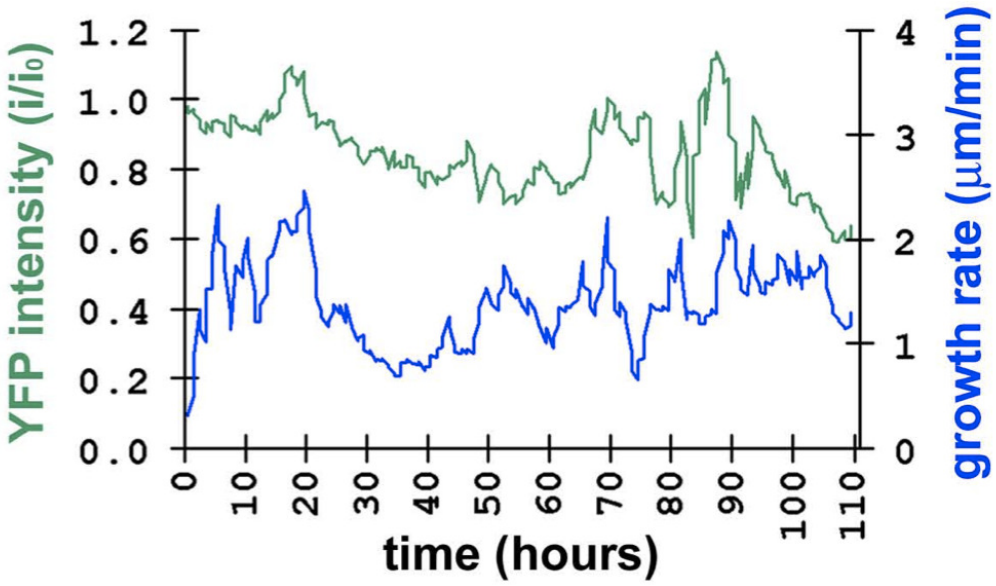

Figure 8.3: Time series of average nuclear intensity and growth rate for a typical experiment.

8.2.7 Sample tracking

The root grows as fast as 4 μm/min during experiments, which necessitates repositioning the root tip in the field of view. Tracking a region of a growing root is a problem which has arisen in other experiments(4); we sought a solution which could be applied rapidly (in about a minute) after every acquisition, which would account for the various motions of the growing root and would track roots expressing all markers of interest. We used image registration, alignment of the most recently acquired image to that previously acquired, with the translational component of the alignment applied to the stage motors.

The algorithm employed is an extension of the Lucas-Kanade algorithm(21) to align images transformed by a rigid motion. Let $I_t(\boldsymbol{r})$ be the measured intensity at time t. For two subsequently acquired images I_{t-1} and I_t, assume that a rigid transformation A_t exists so that $I_t(A_t\boldsymbol{r}) \approx I_{t-1}(\boldsymbol{r})$. We parameterize the transformation A_t by angles of rotation θ_x, θ_y and θ_z about the three axes and translations Δ_x, Δ_y, Δ_z:

$$A_t = \begin{pmatrix} \cos\theta_y\cos\theta_z & -\cos\theta_y\sin\theta_z & \sin\theta_y & \Delta_x \\ \cos\theta_x\sin\theta_z+\sin\theta_x\sin\theta_y\cos\theta_z & \cos\theta_x\cos\theta_z-\sin\theta_x\sin\theta_y\sin\theta_z & -\sin\theta_x\cos\theta_y & \Delta_y \\ \sin\theta_x\sin\theta_z-\cos\theta_x\sin\theta_y\cos\theta_z & \sin\theta_x\cos\theta_z+\cos\theta_x\sin\theta_y\sin\theta_z & \cos\theta_x\cos\theta_y & \Delta_z \\ 0 & 0 & 0 & 1 \end{pmatrix} \tag{8.1}$$

Define the weighted mean square error between the two images under the transformation:

$$\epsilon_t = \sum_{\boldsymbol{r}} w(\boldsymbol{r})\big(I_t(A_t\boldsymbol{r}) - I_{t-1}(\boldsymbol{r})\big)^2 \tag{8.2}$$

where w is the weight per voxel.

For small alignment parameters, we can expand the transformed image intensities:

$$I_t(A_t\boldsymbol{r}) \approx I_t(\boldsymbol{r}) + (\Delta_x - y\theta_z + z\theta_y)\frac{\partial I_t}{\partial x} + (\Delta_y + x\theta_z - z\theta_x)\frac{\partial I_t}{\partial y} + (\Delta_z - x\theta_y + y\theta_x)\frac{\partial I_t}{\partial z} \tag{8.3}$$

The accuracy of the approximation depends on the length scale over which image

intensities change appreciably; if this length scale is large compared to the motion of the rigid transformation, higher order terms can be neglected. As discussed below, the length scale of intensity changes can be manipulated by smoothing the images.

Insert equation (8.3) in (8.2):

$$\begin{aligned}\epsilon_t \approx \sum_{\boldsymbol{r}} w(\boldsymbol{r})\big(I_t(\boldsymbol{r}) - I_{t-1}(\boldsymbol{r}) \\ + (\Delta_x - y\theta_z + z\theta_y)\frac{\partial I_t}{\partial x} + (\Delta_y + x\theta_z - z\theta_x)\frac{\partial I_t}{\partial y} + (\Delta_z - x\theta_y + y\theta_x)\frac{\partial I_t}{\partial z}\big)^2\end{aligned} \tag{8.4}$$

Differentiate with respect to the parameters θ and Δ; for the optimal alignment, all of these derivatives are zero:

$$\begin{aligned}\frac{\partial \epsilon_t}{\partial \theta_x} = \sum_{\boldsymbol{r}} w(\boldsymbol{r})\Bigg((-2\Delta_y z - 2xz\theta_z + 2z^2\theta_x)\left(\frac{\partial I_t}{\partial y}\right)^2 \\ +(2\Delta_z y - 2xy\theta_y + 2y^2\theta_x)\left(\frac{\partial I_t}{\partial z}\right)^2 \\ -2z(I_t - I_{t-1})\frac{\partial I_t}{\partial y} + 2y(I_t - I_{t-1})\frac{\partial I_t}{\partial z}\Bigg) = 0 \\ \frac{\partial \epsilon_t}{\partial \theta_y} = \sum_{\boldsymbol{r}} w(\boldsymbol{r})\Bigg((2\Delta_x z - 2yz\theta_z + 2z^2\theta_y)\left(\frac{\partial I_t}{\partial x}\right)^2 \\ +(-2\Delta_z x - 2xy\theta_x + 2x^2\theta_y)\left(\frac{\partial I_t}{\partial z}\right)^2 \\ +2z(I_t - I_{t-1})\frac{\partial I_t}{\partial x} - 2x(I_t - I_{t-1})\frac{\partial I_t}{\partial z}\Bigg) = 0 \\ \frac{\partial \epsilon_t}{\partial \theta_z} = \sum_{\boldsymbol{r}} w(\boldsymbol{r})\Bigg((-2\Delta_x y - 2yz\theta_y + 2y^2\theta_z)\left(\frac{\partial I_t}{\partial x}\right)^2 \\ +(2\Delta_y x - 2xz\theta_x + 2x^2\theta_z)\left(\frac{\partial I_t}{\partial y}\right)^2 \\ -2y(I_t - I_{t-1})\frac{\partial I_t}{\partial x} + 2x(I_t - I_{t-1})\frac{\partial I_t}{\partial y}\Bigg) = 0\end{aligned} \tag{8.5}$$

$$\begin{aligned}
\frac{\partial \epsilon_t}{\partial \Delta_x} &= \sum_{\boldsymbol{r}} w(\boldsymbol{r}) \Bigg((2\Delta_x - 2y\theta_z + 2z\theta_y) \left(\frac{\partial I_t}{\partial x} \right)^2 \\
&\qquad + 2(I_t - I_{t-1}) \frac{\partial I_t}{\partial x} \Bigg) = 0 \\
\frac{\partial \epsilon_t}{\partial \Delta_y} &= \sum_{\boldsymbol{r}} w(\boldsymbol{r}) \Bigg((2\Delta_y + 2x\theta_z - 2z\theta_x) \left(\frac{\partial I_t}{\partial y} \right)^2 \\
&\qquad + 2(I_t - I_{t-1}) \frac{\partial I_t}{\partial y} \Bigg) = 0 \\
\frac{\partial \epsilon_t}{\partial \Delta_z} &= \sum_{\boldsymbol{r}} w(\boldsymbol{r}) \Bigg((2\Delta_z - 2x\theta_y + 2y\theta_x) \left(\frac{\partial I_t}{\partial z} \right)^2 \\
&\qquad + 2(I_t - I_{t-1}) \frac{\partial I_t}{\partial z} \Bigg) = 0
\end{aligned} \tag{8.6}$$

These six equations can be solved for the parameters θ and Δ. The rest of the approach is identical to that described by Lucas and Kanade(21): the process can be iterated by replacing $I_t(\boldsymbol{r})$ with $I_t(A_t \boldsymbol{r})$ and solving for the optimal alignment parameters again. The weighting parameter is chosen so that voxels are given more weight where the approximation (8.3) is most accurate:

$$w(\boldsymbol{r}) = \frac{L}{L + \left(\frac{\partial I_t(\boldsymbol{r})}{\partial x} - \frac{\partial I_{t-1}(\boldsymbol{r})}{\partial x} \right)^2 + \left(\frac{\partial I_t(\boldsymbol{r})}{\partial y} - \frac{\partial I_{t-1}(\boldsymbol{r})}{\partial y} \right)^2 + \left(\frac{\partial I_t(\boldsymbol{r})}{\partial z} - \frac{\partial I_{t-1}(\boldsymbol{r})}{\partial z} \right)^2} \tag{8.7}$$

where L is a parameter controlling the maximum weight.

At 10 minute acquisition intervals, the root can be displaced by 50 μm, which is much greater than the length scale on which the image intensity changes. To register images related by such large displacements, a rough alignment can be calculated on images smoothed with a large smoothing radius ρ_1. The aligned image resulting from this calculation can be smoothed with a smaller radius $\rho_2 = \alpha \rho_1$ and used to calculate a more refined alignment. Refinements can be repeated until the alignment is sufficiently accurate. In our implementation, $\rho_1 = 10\,\mu$m, $\alpha = 0.72$, 3 refinements are performed, and 50 iterations are performed at each scale. The total alignment typically requires

1 minute to calculate on a contemporary personal computer with a 3.0 GHz dual core processor (Intel Core 2 Duo E8400).

Once the optimal alignment A_t is calculated between the most recently acquired image $I_t(\boldsymbol{r})$ and the previously aligned image $I_{t-1}(A_{t-1}\boldsymbol{r})$, the sample stages are translated. The translation is chosen as follows: a point $\boldsymbol{r_0}$ within the imaged volume, corresponding to the center of the root region of interest, is calculated to travel to $A_t\boldsymbol{r_0}$ under the alignment, then the sample stages are moved according to the translation $\boldsymbol{r_0} - A_t\boldsymbol{r_0}$. This physical translation essentially reverses in image space the most recent displacement of the root. The stages supporting the collection optics are moved to keep the sample within the foci of the objective and the cylindrical lens, accounting for the variable path lengths through air and water. Although only translations are performed physically to track the growing root, the extension of the algorithm to include rotations was necessary to avoid losing the root during acquisitions of several days.

8.2.8 Acquisition software

A program with a graphical interface controlling the stages, camera, LEDs, perfusion system and all acquisition parameters was written in C++. The most computationally demanding task performed during the acquisition is the image registration.

8.3 Images

A variety of tissue specific and cell cycle fluorescent protein fusions have been engineered in *Arabidopsis*(19). We determined that nuclear markers were ideal for our microscope; since the nucleus is small compared to the typical cell, nuclear markers allow individual cells to be easily resolved, and their dynamics during mitosis aid the identification of cell divisions. To image as many nuclei as possible we chose the most uniformly expressed marker available, HISTONE 2B (H2B)::YFP fusion under the control of the

35S promoter of the cauliflower mosaic virus(2). Experiments were also performed with cyclin B markers and GFP fused to a nuclear localization sequence.

Example images are shown in Figure 8.4. The distal 300 μm of the root are imaged throughout experiments, a region which includes the stem cell niche, most of the mitotic activity, and the zone of competence for regeneration after lateral excision(25). With the H2B::YFP marker, about 1500 nuclei were typically observed. Expression was uniform and bright throughout the lateral root cap, columella, and epidermis, while the dense stele exhibited lower expression levels and the cortex expressed so dimly that nuclei could not be separated from noise by eye.

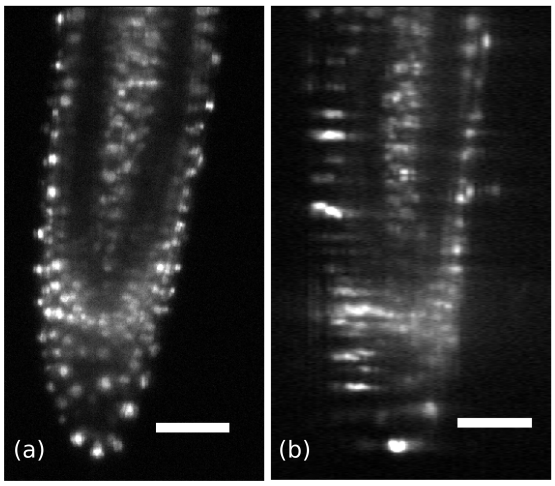

Figure 8.4: Raw images from TLSM - (a) median section, sliced parallel to light sheet, (b) median section, sliced perpendicular to light sheet to show axial resolution. 35S::H2B::YFP plant. Scale bar is 50 μm.

The fluorescence intensity and growth rate from one experiment are plotted in Figure 8.3. Upon transfer to the sample chamber, roots typically grew slowly (<1 μm/min) for about an hour. Mean growth rates were between 1.5 and 4.5 mm/day; rates were often higher for the first hours, with no observed decrease over subsequent days. A decrease in intensity was observed in most trials during the first few hours, of about 40%. No decreasing trend was measured over subsequent times. The continual growth of the root and expression of fluorescence suggest that photobleaching and

phototoxicity are sufficiently low to make long term observations.

8.4 Image analysis

8.4.1 Deconvolution

To extract quantitative data from acquired images, we designed software for segmenting nuclei. We found that deconvolution of images using the measured point spread function (PSF) significantly improved image quality for subsequent analysis. The TLSM PSF is the product of the sheet intensity and the objective PSF, and was measured by scanning 0.3 μm diameter fluorescent beads (Duke Scientific) embedded in 0.5% Phytagel (Sigma-Aldrich). Several scans were averaged, and a final radial averaging was performed to yield an estimate of the TLSM PSF with high signal to noise ratio (>10,000:1). The excitation sheet profile varies in x, but the variation over the typical root thickness of 100 μm is negligible and therefore our deconvolution routine assumes a shift invariant PSF. The algorithm for deconvolution is an expectation maximization assuming Poisson noise(13). 30 iterations are used, and 3D fast Fourier transforms are performed using the FFTW library(8). The deconvolution improves separability of nearby nuclei without introducing artifacts that would interfere with image analysis. Figure 8.5 plots the intensity profile along the axial dimension for nearby nuclei and Figures 8.6 and 8.7 compare raw and deconvolved images.

8.4.2 Intensity normalization

Measured intensities vary 3 fold within nuclei from the same tissue. The brightest nuclei are found in regions of the root near the surface facing the excitation sheet and the collection objective and the dimmest are found in the opposite sector, consistent with attenuation caused by passage through tissue. The wide range of nuclear intensities complicates automatic segmentation - a threshold low enough to separate dim nuclei

from background also separates noise in brighter regions. We developed a method to estimate the depths of penetration through tissue of the excitation and emission beams for each voxel, then used a large data set of measured intensity as a function of these two depths to fit a normalization function. To estimate the penetration depths, a global intensity threshold is applied to the image, with a level chosen low enough to extract all signal from background. The resulting cloud of points is a sparse representation of the volume comprising the root. To estimate its boundary, the three dimensional convex hull of the point cloud is calculated using the geometry package of R(1).

For a point p within the root, the distance along the excitation axis to the convex hull (ℓ_1) and the distance along the collection axis to the convex hull (ℓ_2) are calculated. The maximum intensity per nucleus I_{max} was plotted as a function of ℓ_1 and ℓ_2 for a crudely segmented data set of over 100,000 data points from an experiment with a 35S::H2B::YFP plant. The logarithm of I_{max} was found to decay monotonically with increasing l_1 and l_2, on average, and so a simple quadratic function was fit to $\log I_{max}$:

$$f(\ell_1, \ell_2) = c_1 + c_2\ell_1 + c_3\ell_2 + c_4\ell_1^2 + c_5\ell_2^2 + c_6\ell_1\ell_2 \tag{8.8}$$

with results of the fit shown in Table 8.1. The intensity is found to decay more rapidly with penetration depth from the collection axis, as expected due to the larger numerical aperture of the objective. In automated analysis, the depths ℓ_1 and ℓ_2 are calculated for each voxel, and a normalized image is created with intensity multiplied by $\exp(-f(\ell_1, \ell_2))$.

After normalization for penetration depth, intensities were found to be tightly distributed within tissue types, with more significant variation across tissues. As discussed in section 8.3, very dim expression was observed in the endodermis for 35S::H2B::YFP plants.

coefficient	value
c_1	arbitrary
c_2	-3.053e-2 μm^{-1}
c_3	-4.503e-2 μm^{-1}
c_4	2.609e-4 μm^{-2}
c_5	3.312e-4 μm^{-2}
c_6	4.948e-5 μm^{-2}

Table 8.1: Coefficients from equation 8.8 empirically fit to I_{max}.

8.4.3 Segmentation

Significant morphological heterogeneity of nuclei was observed (see Figures 8.4, 8.6 and 8.7). A custom segmentation routine was developed, similar to that described by Keller et al. for analysis of the nuclei of developing zebrafish embryos(16). A series of increasing global segmentation thresholds is applied, and the resulting contiguous sets of voxels are tested for a set of criteria for classification as a nucleus. Each contiguous set of voxels is called a blob. Upon positive classification, a blob's voxels are excluded from analysis at higher thresholds. The criteria for classification are ranges for the number of voxels, mean intensity, lateral size, lateral eccentricity and axial size. The intensity profile along the collection axis is computed for each blob and tested for the absence of multiple maxima, to prevent classification of two nearby nuclei with similar lateral coordinates as a single nucleus. The criteria ranges were optimized by simulated annealing, using a training set of 850 manually segmented nuclei.

The segmentation routine outputs a time series of centroid location, maximum and mean intensities, voxel count, lateral size, lateral eccentricity and axial size for each detected blob. The locations of segmented nuclei are shown superimposed on the corresponding deconvolved slices in Figure 8.8. The routine was validated on a set of 1303 manually identified nuclei, from a single time point of an experiment. The routine failed to identify 90 of the nuclei in the test set (false negative rate 6.9%), while labeling as nuclei 95 blobs not present in the test set (false positive rate 7.3%). The error rate

was significantly higher in the stele compared to the rest of the root.

The segmentation technique is robust to small differences in nuclear morphology, and extension to other markers should be straightforward. Images of a new marker could be manually segmented, with the results used to train a new set of classification criteria. Extension to morphologically distinct markers such as membrane markers would likely require a significantly different approach.

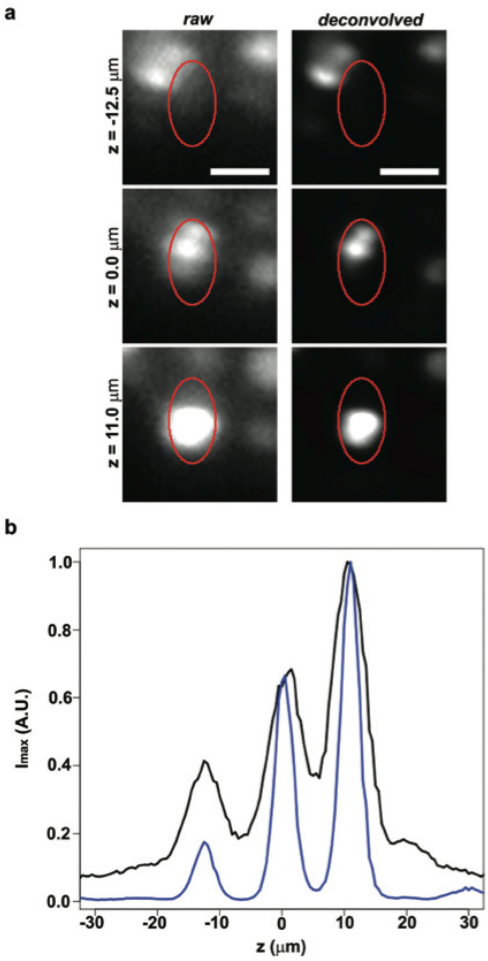

Figure 8.5: Axial intensity profiles comparing raw and deconvolved images - (a) three axial slices showing the relative positions of three nuclei, with the red ellipse outlining the region of interest, scale bar 7.5 μm, (b) plot of maximum intensity within region of interest per axial slice, raw data in black and deconvolved data in blue.

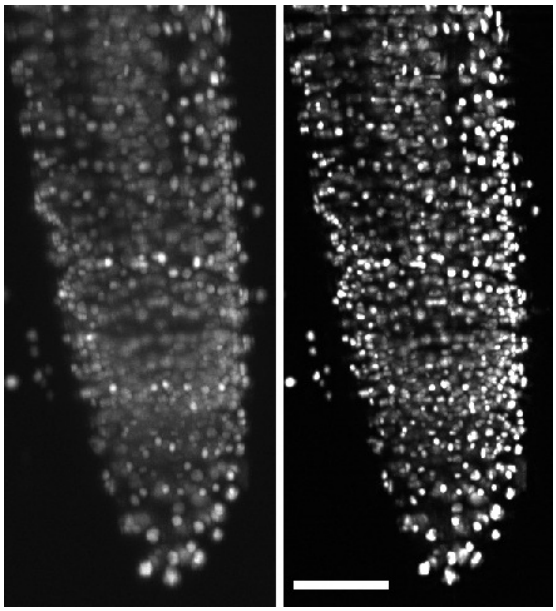

Figure 8.6: Maximum projections along z axis comparing raw image (left) to deconvolved image (right). 35S::H2B::YFP plant. Scale bar is 50 μm.

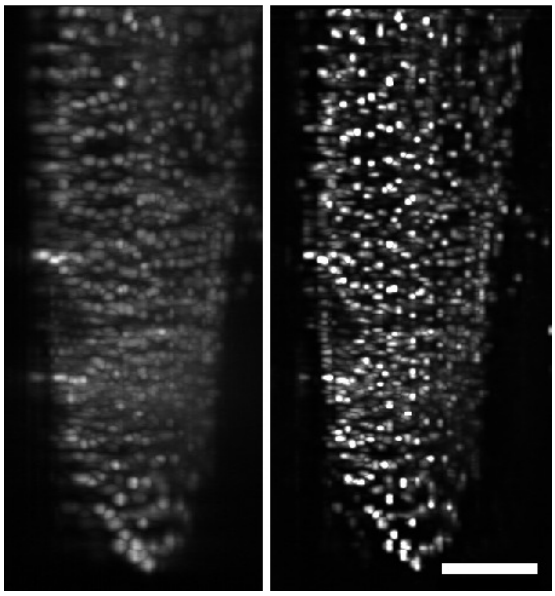

Figure 8.7: Maximum projections along x axis comparing raw image (left) to deconvolved image (right). 35S::H2B::YFP plant. Scale bar is 50 μm.

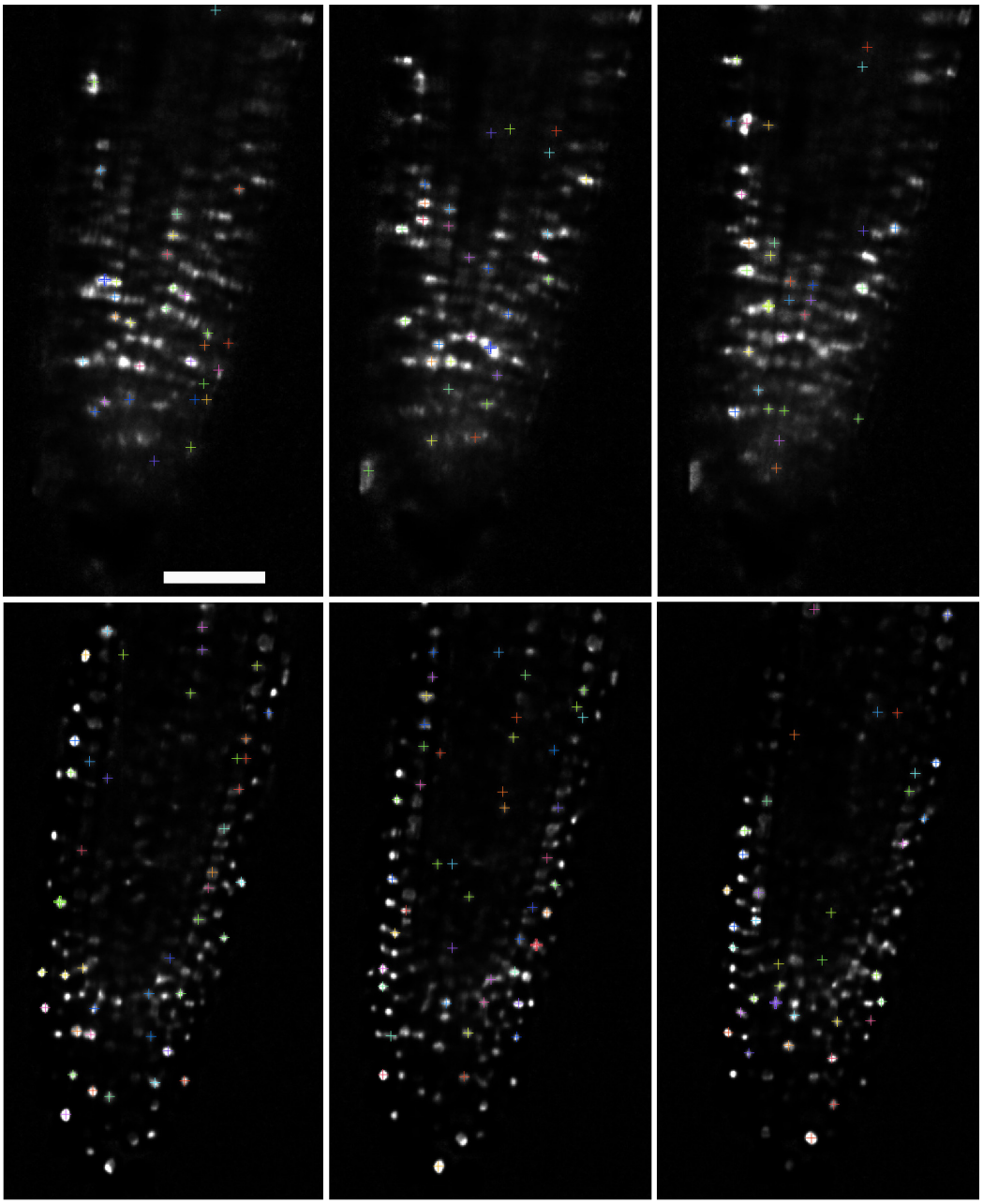

Figure 8.8: Overlay of segmented centroids on deconvolved slices - The top row shows three adjacent slices from the section of the root farther from the objective, while the bottom row shows three adjacent slices from the section of the root nearer the objective. Slice spacing is 2.5 μm and scale bar is 50 μm. Colored crosses show centroids of automatically segmented nuclei. Most unmarked nuclei are located in nearby planes which are not shown; see section 8.4.3 for details regarding segmentation error rates.

8.5 Nucleus tracking

To compile data on nuclear motions and cell divisions, we developed a software routine for automated nucleus tracking. The problem of cell tracking has arisen many times, but solutions tend to be specific to the biological system and even the markers and imaging methods(6, 20, 24). The general problem of tracking multiple objects in three spatial dimensions in the presence of noise is a difficult problem, and is complicated by biological processes such as cell division or death, and technical issues, such as object intermittency near the boundary of the imaged volume. Since data sets of interest may provide enormous amounts of data, the statistical resolution is likely to be limited by errors in the tracking routine. Thus it is crucial to pose the tracking problem in a general way, both so that development of useful tools can benefit many researchers and so that results from various organisms, developmental stages and imaging methodologies can be compared within a rigorous framework.

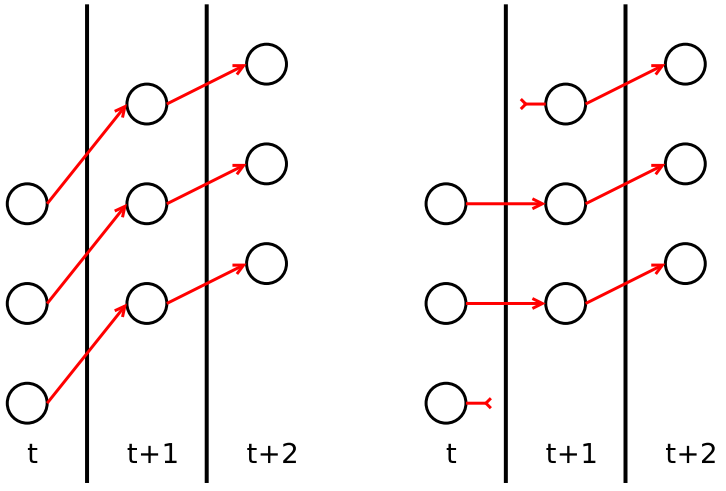

Figure 8.9: Example object tracking problem - Three objects are depicted as circles at three times, moving in a single spatial dimension. Assignment of identity is represented by red arrows. In the case that the objects are moving collectively, the configuration on the left is correct. However, local minimization of displacements would produce the erroneous configuration on the right.

The general problem of tracking requires a global minimization of object differences

over time; a local minimization can lead to many errors, as demonstrated by a simple example. Figure 8.9 shows three objects in collective motion across three discrete time points. The correct assignment is depicted on the left, with red arrows representing assignment of identity. The assignment reached by local minimization of displacements is shown on the right. By applying a penalty to unassigned objects, the problem could be solved using a semi-local approach, such as solving the simple assignment problem via the Hungarian algorithm(18) for each pair of neighboring time points, then stitching together the results appropriately. However, more complex cases cannot be solved with this simpler approach and the problem must be treated globally.

Tracking multiple objects over time is an instance of the multidimensional assignment problem (MAP), which is known to be NP-hard, so that the number of steps to find optimal solutions in the worst case is exponential in the problem size(15, 23). Due to the computational complexity, we advocate stochastic methods. The importance of generally phrasing the tracking problem and the use of stochastic optimization have been stressed by Gor et al.(10).

The MAP can be phrased as follows: consider a cost array A of size n and dimensionality m, so that $E \in (\mathbb{R}^m)^n$. The solution is the set of permutations σ_j which minimizes the total cost:

$$\min \sum_{i=1}^{n} E_{\sigma_1(i)\sigma_2(i)\ldots\sigma_m(i)} \tag{8.9}$$

where each σ_j maps $\{1, 2, \ldots, m\}$ to itself. For object tracking, the index i refers to time, and m is the number of objects, so that $\sigma_j(i)$ represents the identity assigned to the j^{th} object at time point i. The cost matrix E is defined so that the proper assignment of all object identities minimizes the total cost. For example, if position data $r_j(t)$ at each time t for each object j is presented, the squared displacement can

be used:

$$\begin{aligned} E_{j_1(t)j_2(t)\ldots j_m(t)} = &\Big(r_{j_1(t)}(t) - r_{j_1(t+1)}(t+1)\Big)^2 + \Big(r_{j_1(t-1)}(t-1) - r_{j_1(t)}(t)\Big)^2 \\ &+\Big(r_{j_2(t)}(t) - r_{j_2(t+1)}(t+1)\Big)^2 + \Big(r_{j_2(t-1)}(t-1) - r_{j_2(t)}(t)\Big)^2 \\ &\vdots \\ &+\Big(r_{j_m(t)}(t) - r_{j_m(t+1)}(t+1)\Big)^2 + \Big(r_{j_m(t-1)}(t-1) - r_{j_m(t)}(t)\Big)^2 \end{aligned} \quad (8.10)$$

False negatives can be handled without interrupting trajectories by assigning "virtual" or "ghost" objects. Cell divisions and fusions can also be treated within the MAP framework. The definition of the cost matrix E depends on the properties of the objects being tracked. The main difficulties in our case are the density of nuclei compared to the typical nuclear displacement over the sampling interval, the significant error rates of the segmentation routine and the presence of cell divisions. The approach uses correlation in nucleus position at adjacent time points as the predominant determinant of the cost matrix, as other features such as intensity and nucleus size fluctuate more than position, due to biological and optical effects. Additional terms are used for cell division events, since these were found to have stereotypical behavior.

8.5.1 Registration

Nucleus positions from neighboring time points must be aligned before starting the nucleus tracking. The alignment performed by the sample tracking as described in section 8.2.7 is predictive: the two previously acquired stacks are compared in order to calculate a translation for the next scan. A more refined alignment is calculated after segmentation and before nucleus tracking. This alignment minimizes by iterated gradient descent the mean squared nucleus displacements over adjacent time points, with respect to rigid motions. The resulting frame of reference is used for nucleus tracking.

8.5.2 Tracking algorithm

For tracking objects by position, the typical displacement per time point Δ and the typical distance between nearest neighbors r determine the difficulty of tracking. In our case, $\Delta = 1.5 \pm 1.2\,\mu$m over 10 minutes, while $r = 10 \pm 4\,\mu$m, a regime in which identity assignment according to minimum displacement leads to many conflicts and errors. Since the size of the problem is large ($\sim$1500 nuclei per time point, with hundreds of time points), exact solutions by deterministic algorithms are impractical. Instead, we obtain an approximate solution by simulated annealing, and the cost matrix E is interpreted as an energy(17). Segmentation errors are accommodated by allowing temporal gaps in nuclear trajectories, and cell divisions are dealt with using empirical properties of division events. The initial configuration is generated by assigning each nucleus at time t to its nearest neighbor at time $t+1$, producing many "fusion" events with corresponding high energy. The assignments are iteratively and randomly adjusted to lower the energy.

The data structure for nuclear identities is an array of trees, in which each tree represents a unique nucleus. Each node corresponds to a segmented blob, and an edge between two nodes indicates that the corresponding blobs represent the same nucleus at adjacent times. If no temporal gaps were present, each level of a tree would represent one time point of the experiment, but false negatives in the image analysis necessitate skipping isolated time points for some nuclei, so that a blob at time t can be directly associated with a blobs at times $t+1$, $t+2$, etc. In this way nuclei can be tracked for longer than the duration implied by the false negative rate of the segmentation procedure. In practice the temporal gap is limited to three time points. While most nodes have a single parent and a single child, it is possible for a node to have zero parent or child nodes, due to a nucleus leaving or entering the imaged volume during the experiment, or two parent or child nodes, due to a fusion or division event. Although fusions are not expected to occur biologically, the presence of these events in the analysis

allows manual consideration of cases where the optical quality is poor. Fusion events are especially useful for filtering spurious division events due to unresolved nuclei.

8.5.3 Configuration energy

The total energy of a configuration is a sum over all edges of all trees of squared spatial displacement, a penalty for temporal gaps, a penalty for terminal nodes and a penalty for branching. Number each blob i, its position r_i, time t_i, lateral size λ_i and maximum intensity I_i. Define an indicator function A_{ij} with value 1 when blob i is directly equated with blob j and 0 otherwise. Since the only term with physical meaning is the squared displacement, the unit of energy is μm^2. For each blob, the number of parent nodes m_i and the number of child nodes n_i are determined:

$$\begin{aligned} m_i &= \sum_{j:t_j<t_i} A_{ij} \\ n_i &= \sum_{j:t_j>t_i} A_{ij} \end{aligned} \tag{8.11}$$

The total energy of a configuration is

$$\epsilon = \sum_i f(m_i) + g(n_i) + \sum_{j:t_j<t_i} A_{ij}\big(|r_i - r_j|^2 + \alpha(t_i - t_j - 1)^2\big) \tag{8.12}$$

where $\alpha = 20\mu\text{m}^2$, and $f(m)$ and $g(n)$ are functions defined as follows for penalizing nodes with numbers of parents and children not equal to one:

$$f(m_i) = \begin{cases} 100\,\mu\text{m}^2 & : m_i = 0 \\ 0\,\mu\text{m}^2 & : m_i = 1 \\ 195\,\mu\text{m}^2 & : m_i = 2 \\ \infty\,\mu\text{m}^2 & : m_i > 2 \end{cases} \tag{8.13}$$

so that fusions are allowed but heavily penalized, without regard for other characteristics of the fusion event.

The penalty for two children $g(2)$ consists of several terms specific to cell divisions, derived from empirical observations. Terms are designed to favor the identification of stereotypical mitotic events as cell divisions while rejecting events in which two nuclei pass close to each other. The events to be rejected include the appearance of a false positive blob near a true nucleus as well as the disappearance of a nucleus at a time point (false negative) followed by its reappearance near another true nucleus. Without these extra terms, it was not possible to automatically identify true cell divisions with acceptable error rates.

In a set of 461 manually identified cell divisions from a single experiment, the centroid displacement from the parent cell to each daughter cell was on average 2.5 fold greater than the average non-dividing displacement (2.6 μm compared to 1.1 μm). These displacements are used to distinguish true divisions as follows. Consider a blob numbered i which has two daughter blobs j and k. Define the spatial displacements for the potential division event $\Delta r_{ij} = r_i - r_j$ and $\Delta r_{ik} = r_i - r_k$, the deviation of the magnitude of the displacement from the empirical average for true divisions $\delta_{ij} = |\Delta r_{ij}| - \langle |\Delta r| \rangle_{\text{divisions}}$ and the standard deviation of the empirical distribution of $|\Delta r|$, $\sigma = 0.63\,\mu$m. A term for displacements was designed to apply zero penalty to potential divisions with displacement within two standard deviations of the mean empirical displacement, and a penalty increasing quadratically for larger deviations:

$$L_{ij} = \left(1 - \text{rect}\left(\frac{\delta_{ij}}{4\sigma}\right)\right)\left(1.5\,\mu\text{m}^2 + (\delta_{ij} - 2\sigma)^2\right) \tag{8.14}$$

where rect is the rectangle function:

$$\mathrm{rect}(x) = \begin{cases} 1 & : |x| < 1/2 \\ 1/2 & : |x| = 1/2 \\ 0 & : |x| > 1/2 \end{cases} \tag{8.15}$$

It was observed that most real divisions have stereotypical orientation, so that the angle between the displacement vectors is close to π radians. Hence an additional term was defined to favor such orientations:

$$\omega_{ijk} = 75\,\mu\mathrm{m}^2 \left(1 + \frac{\Delta r_{ij} \cdot \Delta r_{ik}}{|\Delta r_{ij}||\Delta r_{ik}|}\right) \tag{8.16}$$

and the term for number of child nodes is

$$g(n_i) = \begin{cases} 100\,\mu\mathrm{m}^2 & : n_i = 0 \\ 0\,\mu\mathrm{m}^2 & : n_i = 1 \\ L_{ij} + L_{ik} + \omega_{ijk} & : n_i = 2 \\ \infty\,\mu\mathrm{m}^2 & : n_i > 2 \end{cases} \tag{8.17}$$

Although values were based on empirical measurements, the choice of form for the various terms was somewhat arbitrary, and limited by the statistical resolution available. With a larger set of true divisions (possibly arising from the automatic analysis of several experiments), a more exact empirical approach such as maximum likelihood could be used.

8.5.4 Optimization

The same scheme was used for analysis of all experimental data. The initial configuration is chosen by identifying each blob at time t with its nearest neighbor at time $t+1$. This results in many fusion events, as one blob can be nearest to multiple blobs from

the previous time point. Only assignments within a spatial radius of 6 μm are allowed, since displacements of this magnitude have not been observed in our experiments. The move at each step is chosen randomly, but with a bias proportional to node energy for choosing a move target. Once node i is chosen as a target, the possible moves include cutting a connection by flipping A_{ij} from 1 to 0 for some j, adding a connection by flipping A_{ij} from 0 to 1, or changing a connection by flipping A_{ij} to 0 and A_{ik} to 1 for some $k \neq j$. Move acceptance follows the Metropolis criterion(22). We found that allowing two serial moves, where one of the adjusted nodes from the first moves is chosen as target for the second move, improved the rate of convergence significantly, while allowing three or more moves in serial did not result in further improvement.

The critical temperature for annealing the energy defined in (8.12) was approximately 70 μm^2: see Figure 8.10 for data from an optimization over a large range of temperatures.

The initial temperature is set at twice the critical temperature, the configuration is equilibrated for several thousand moves, then the temperature is exponentially cooled. Optimization by simulated annealing was slow due to the large size of the typical problem - thousands of nuclei for hundreds of time points. To address this, the algorithm was parallelized, so that at each step of the annealing, n moves are attempted and scored in separate threads. It was found that accepting the lowest energy outcome according to the Metropolis criterion led to speed up almost equal to n for $n < 8$. Massive parallelization by this method is not practical due to memory requirements. It should be possible to optimize on smaller time intervals with a routine for concatenating the results but this is nontrivial due to edge effects. Other stochastic optimization schemes for combinatorial problems such as evolutionary algorithms or swarm algorithms may be more efficient for this problem, especially in the massively parallel regime. We chose simulated annealing because it is firmly established, understood by the author and straightforward to implement efficiently.

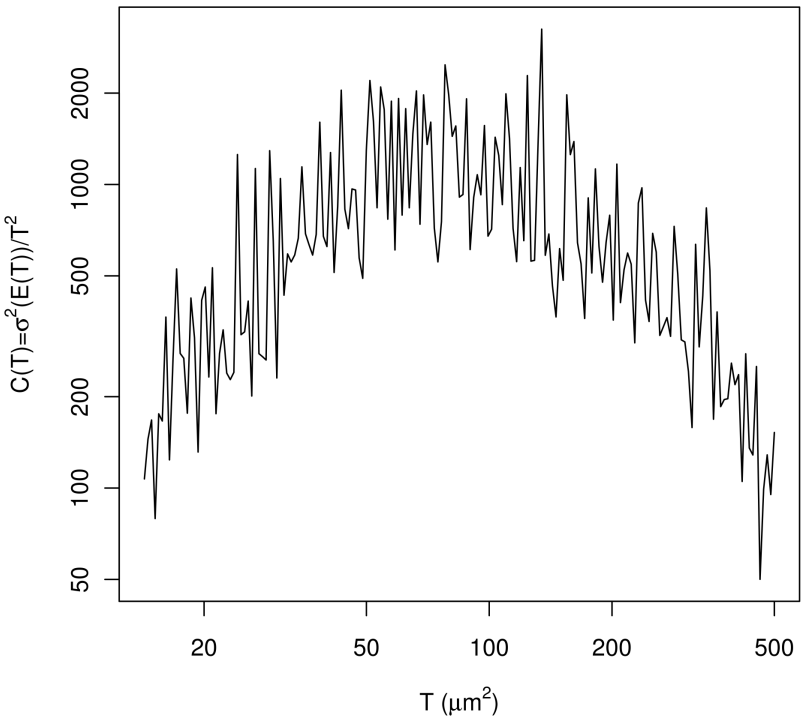

Figure 8.10: Critical temperature of trajectory annealing - the specific heat is estimated over a range of temperatures by $C(T) = \sigma^2(E(T))/T^2$. The critical temperature corresponds to the maximum around 70 μm^2.

Besides simple parallelization, an additional approach was taken to improve the efficiency of the tracking algorithm. The performance of the routine depends strongly on the number of nodes N, since in general the number of nodes which must be changed to achieve the lowest energy state from the initial state is linear in N, and several steps in the implementation require searching or copying all of the nodes, so that in the worst case the number of steps necessary is at least $O(N^2)$. However, early in the optimization most moves are made on very high energy nodes. Therefore a technique was designed to freeze the configuration between all nodes contributing an energy below a threshold, so that only the high energy nodes and their connections need be considered for optimization. Once this smaller problem has reached a minimum energy, the threshold can be removed and the full problem can be considered. This

technique was found to result in very similar final configurations compared to annealing the full configuration from the initial state, while significantly reducing the number of nodes and computational time. Experimental results will be presented in chapter 9.

8.5.5 Validation

The tracking procedure was validated manually by choosing 100 trajectories at random and identifying errors by considering high energy nodes and inspection of images when necessary. Some ambiguity exists in the manual tracking due to poor image quality. We calculated lower and upper bounds on the error rate of 2.4% and 3.9% per nucleus per time point.

The forward branching events in the configuration are considered potential cell divisions, but also contain many spurious divisions. The majority of spurious divisions result from false negatives in the segmentation procedure, in the form of classification of two nearby nuclei as a single nucleus at one time point, followed by proper separation the subsequent time point. Rather than attempt to tune the parameters in the energy, we used additional dynamic features of true cell divisions to build a classifier. We observed that nuclear intensity typically increased in the 20 minutes preceding a cell division, then rapidly decreased to below the mean value, and finally returned to the average over the following 30 minutes. Nuclear size was similarly stereotypical. We trained a support vector machine (SVM)(5) on nuclear size and intensity from time points within a temporal neighborhood of true cell division events as well as the temporal persistence of the parent trajectory and both daughter trajectories. A comprehensive set of 461 true cell divisions was built manually from a single experiment, and the SVM was trained on a subset of 424 of these along with 3805 spurious branching events. The result of the training was an out of sample accuracy of 92.3% in five fold cross validation. The SVM was then used to classify all branching events, yielding 340 true positives (73.8%) and 58 false negatives (12.6%).

Bibliography

[1] C. Bradford Barber, David P. Dobkin, and Hannu Huhdanpaa. The quickhull algorithm for convex hulls. *ACM Transactions on Mathematical Software*, 22:469–483, 1996. 150

[2] Corinne Boisnard-Lorig, Adan Colon-Carmona, Marion Bauch, Sarah Hodge, Peter Doerner, Estelle Bancharel, Christian Dumas, Jim Haseloff, and Frédéric Berger. Dynamic analyses of the expression of the HISTONE::YFP fusion protein in *Arabidopsis* show that syncytial endosperm is divided in mitotic domains. *Plant Cell*, 13:495–509, 2001. 148

[3] Jan A. N. Buytaert and Joris J. J. Dirckx. Design and quantitative resolution measurements of an optical virtual sectioning three-dimensional imaging technique for biomedical specimens, featuring two-micrometer slicing resolution. *Journal of Biomedical Optics*, 12:014039–1–13, 2007. 136

[4] Ana Campilho, Bernardo Garcia, Henk v.d. Toorn, Henk v. Wijk, Aurélio Campilho, and Ben Scheres. Time-lapse analysis of stem-cell divisions in the *Arabidopsis thaliana* root meristem. *The Plant Journal*, 48:619–627, 2006. 144

[5] Corinna Cortes and Vladimir Vapnik. Support-vector networks. *Machine Learning*, 20:273–297, 1995. 165

[6] O Dzyubachyk, W Niessen, and E Meijering. A variational model for level-set based cell tracking in time-lapse fluorescence microcopy images. In *4th IEEE international symposium on biomedical imaging: macro to nano*, volume 1-3, pages 97–100, 2007. 156

[7] Cristoph J. Engelbrecht and Ernst H. K. Stelzer. Resolution enhancement in a light-sheet-based microscope (SPIM). *Optics Letters*, 31:1477–1479, 2006. 142

[8] Matteo Frigo and Steven G. Johnson. The design and implementation of FFTW3. *Proceedings of the IEEE*, 93:216–231, 2005. 149

[9] Eran Fuchs, Jules S. Jaffe, Richard A. Long, and Farooq Azam. Thin laser light sheet microscope for microbial oceanography. *Optics Express*, 10:145–154, 2002. 135, 136

[10] Victoria Gor, Michael Elowitz, Tigran Bacarian, and Eric Mjolsness. Tracking cell signals in fluorescent images. In *Workshop on Computer Vision in Bioinformatics, IEEE CVPR Annual Meeting*, 2005. 157

[11] Doeke Hekstra. *Population dynamics in a model closed ecosystem.* PhD thesis, The Rockefeller University, New York, New York, 2009. 135

[12] Terrence F. Holekamp, Diwakar Turaga, and Timothy E. Holy. Fast three-dimensional fluorescence imaging of activity in neural populations by objective-coupled planar illumination microscopy. *Neuron*, 57:661–672, 2008. 136

[13] Timothy J. Holmes. Maximum-likelihood image restoration adapted for noncoherent optical imaging. *Journal of the Optical Society of America A*, 5:666–673, 1988. 149

[14] Jan Huisken, Jim Swoger, Filippo Del Bene, Joachim Wittbrodt, and Ernst H. K. Stelzer. Optical sectioning deep inside live embryos by selective plane illumination microscopy. *Science*, 305:1007–1009, 2004. 135, 136

[15] Richard Karp. Reducibility among combinatorial problems. In R.E. Miller and J.W. Thatcher, editors, *Complexity of Computer Computations*, pages 85–104, New York, NY, 1972. Plenum Press. 157

[16] Philipp J. Keller, Annette D. Schmidt, Joachim Wittbrodt, and Ernst H. K. Stelzer. Reconstruction of zebrafish early embryonic development by scanned light sheet microscopy. *Science*, 322:1065–1069, 2008. 136, 151

[17] Scott Kirkpatrick, C. D. Gelatt, and M. P. Vecchi. Optimization by simulated annealing. *Science*, 220:671–680, 1983. 159

[18] HW Kuhn. The Hungarian method for the assignment problem. *Naval Research Logistics Quarterly*, 2:83–97, 1955. 157

[19] Laurent Laplaze, Boris Parizot, Andrew Baker, Lilian Ricaud, Alexandre Martinière, Florence Auguy, Claudine Franche, Laurent Nussaume, Didier Bogusz, and Jim Haseloff. GAL4-GFP enhancer trap lines for genetic manipulation of lateral root development in *Arabidopsis thaliana*. *Journal of Experimental Botany*, 56:2433–2442, 2005. 147

[20] K Li, ED Miller, M Chen, T Kanade, and LE Weiss. Cell population tracking and lineage construction with spatiotemporal context. *Medical Image Analysis*, 12:546–566, 2008. 156

[21] Bruce D. Lucas and Takeo Kanade. An iterative image registration technique with application to stereo vision. In *Proceedings of Imaging Understanding Workshop*, pages 121–130, 1981. 144, 146

[22] Nicholas Metropolis, Arianna W. Rosenbluth, Marshall N. Rosenbluth, Augusta H. Teller, and Edward Teller. Equation of state calculations by fast computing machines. *The Journal of Chemical Physics*, 21:1087–1092, 1953. 163

[23] Carlos A.S. Oliveira and Panos M. Pardalos. Randomized parallel algorithms for the multidimensional assignment problem. *Applied Numerical Mathematics*, 49:117–133, 2004. 157

[24] G. Rabut and J. Ellenberg. Automatic real-time three-dimensional cell tracking by fluorescence microscopy. *Journal of Microscopy*, 216:131–137, 2004. 156

[25] Giovanni Sena, Xiaoning Wang, Hsiao-Yun Liu, Hugo Hofhuis, and Kenneth D. Birnbaum. Organ regeneration does not require a functional stem cell niche in plants. *Nature*, 457:1150–1153, 2009. 148

[26] H Siedentopf and R Zsigmondy. Über Sichtbarmachung und Größenbestimmung ultramikroskopischer Teilchen, mit besonderer Anwendung auf Goldrubingläser. *Annalen der Physik*, 315:1–39, 1902. 135

Chapter 9

Quantitative measurements of growing and regenerating *Arabidopsis* roots

9.1 Introduction

Chapter 7 motivated the study of regeneration in *Arabidopsis* roots as a system for studying development with certain experimental advantages over embryogenesis. As discussed, the dynamics of patterning in the adult intact organ have not been elucidated quantitatively. To this end we first performed experiments to measure nuclear motions and cell divisions in uncut roots over a time scale of several days, comparable to that required for regeneration. The data from these experiments can determine to what extent patterning arises deterministically from the location, timing and orientation of cell divisions, a process which has been hypothesized to maintain the pattern of the root from embryogenesis(2). In particular, the behavior of cells originating in the stem cell niche can be followed.

Detailed analysis was performed for images from a single experiment with an intact root to demonstrate the technique. This experiment will be presented in detail, supported by partial results from other experiments.

Much of our work on plant roots has been towards the technical developments

described in chapter 8. Although it is our hope that the methods we developed will be used to study regeneration from a quantitative perspective, we have yet to complete enough experiments and analyses to make conclusions regarding regeneration. Images acquired from a regenerating root will be presented to show that our setup is capable of acquiring suitable data from regenerating roots, although the analysis of this data is currently incomplete.

9.2 Results

In the first experiment, a plant expressing the nuclear protein histone H2B fused to yellow fluorescent protein (YFP) was imaged for 70 hours at 10 minute intervals. The root grew 2.74 mm during this time - a slower growth rate than average but well within the extrema for all experiments, excluding data in the case of contamination. A time series of the average nuclear intensity and the rate of growth is plotted in Figure 9.1. Images from this experiment were deconvolved and segmented as described in chapter 8. The first 29 hours of this experiment were further analyzed by building nuclear trajectories through time. The restriction to the first 40% of the experiment was due to computational cost while developing the tracking routine.

The segmentation routine returned an average of 1520 nuclei per time point, with a standard deviation of 57 nuclei. The fluctuations were largely due to motions of the root which caused nuclei near the edge of the field of view to enter or exit the analyzed region. The density of identified nuclei accurately reflects the known symmetry of the root, indicating that penetration depth through tissue does not appreciably interfere with automatic identification of nuclei (Figure 9.2).

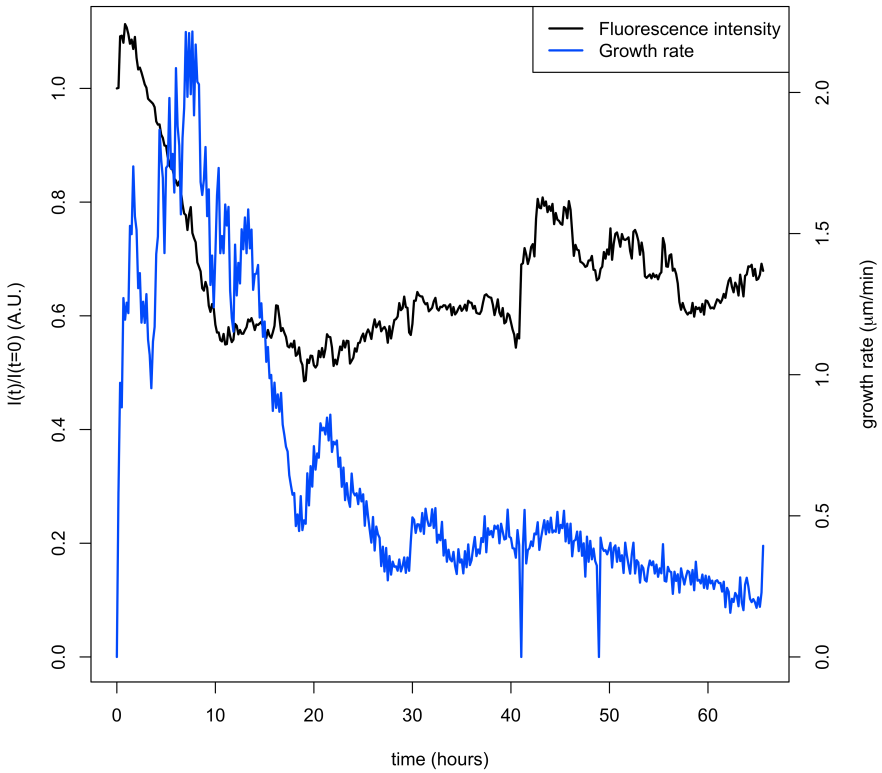

Figure 9.1: Intensity and growth dynamics of growing root - intensity of highest 0.3% intensity quantile of raw images vs. time and growth rate for uncut, growing root.

9.2.1 Nuclear motions

To analyze nuclear motions within the moving frame of reference in which the root tip is at rest, we transformed the positions of all nuclei to cylindrical coordinates m (main root axis), ρ (radial axis) and θ (angle). Visual inspection suggested that nuclear motions consisted of random individual fluctuations on short time scales plus collective motions of nearby cells on long time scales, primarily in the form of elongation of cells along the root axis m. The average periodogram of displacements for 651 nuclear trajectories consisting of at least 100 time points was calculated and is plotted in Figure 9.4. The peak at low frequency is interpreted as the directed component of motion, and the decomposition shows that most of this occurs along the m axis. The high frequency components seem to be random motions of the nucleus within the cell. Both

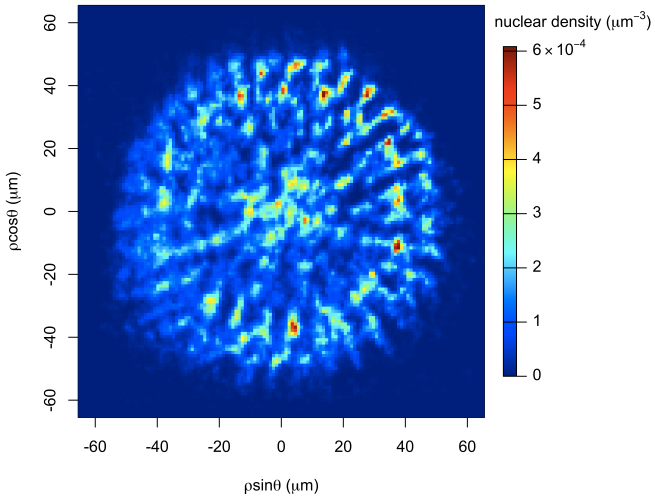

Figure 9.2: Number of nuclei per volume averaged over 29 hours, in cross section.

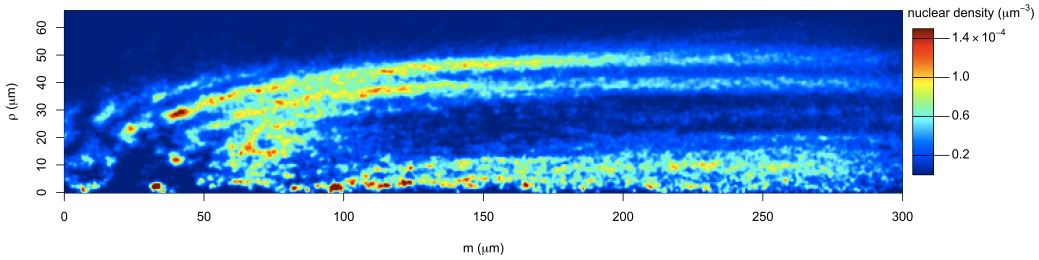

Figure 9.3: Number of nuclei per volume averaged over 29 hours, in longitudinal section.

components are shown for a typical nucleus in Figure 9.5.

Collective motions vary spatially over length scales of only a few cell lengths and temporally over several hours. To accurately estimate collective motions in light of these variations, data were binned spatially in cubes with edges of 5 μm and averaged over two temporal windows, chosen as 0-20 hours and 21-29 hours due to a decrease in the expansion rate and coincident narrowing by about 10 μm of the most proximal imaged region, occurring around 21 hours. The velocity vector field was estimated and the three cylindrical components of velocity (v_m, v_ρ and ρv_θ) were considered separately.

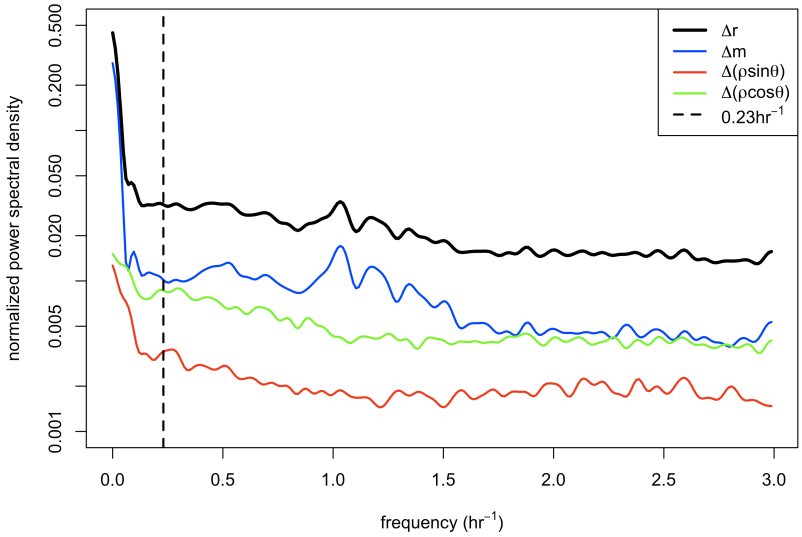

Figure 9.4: Average normalized power spectral density of displacements for 651 trajectories containing at least 100 time points (16.7 hours). The contributions in each dimension are shown in color, and the threshold frequency of 0.23 hr^{-1} used to separate fast and slow time scale motions is indicated by the dotted black line.

Only the velocity component along the root was found to vary significantly with time or space, and this component varied only with m and not with θ or ρ (Figure 9.6). The radial component of velocity v_ρ and the angular component ρv_θ were indistinguishable from zero in all bins (see Figure 9.7).

Collective motions, possibly combined with variable rates of cell division, also contribute to large changes in the spatial density of nuclei, as shown in Figures 9.8, 9.9 and 9.10. The most proximal region of the root narrows, as mentioned above, while the density of nuclei at intermediate ρ, corresponding to the second layer of tissue from the surface, increases over time (Figure 9.9). Elongation along m, possibly combined with inhomogeneities in the rate of cell division, causes the initially dense region located 100-150 μm from the tip to spread out, resulting in a much more uniform density of nuclei from 100-300 μm (Figure 9.8). The lack of twisting is evident in the plot of nuclear density in angular position θ versus time (Figure 9.10).

9.2.2 Cell divisions

The automated analysis identified 340 true cell divisions in the 29 hour interval. As discussed in chapter 8, cell divisions were found to have stereotypical dynamics; displacement of daughter cells from the parent is on average 2.5 times greater than the average displacement, while maximum intensity and lateral size increase just before division and decrease during division (Figure 9.12). The mean behavior An example of a dividing trajectory is shown in Figure 9.11. The timing of cell divisions exhibits temporal correlations (Figure 9.13), while the spatial distribution of cell divisions seems to be nonuniform. To normalize for temporal variations, the times of cell divisions can be used to weight the density of nuclei in space, producing a normalized spatial density for all nuclei which can be compared to the spatial distribution of identified divisions (Figure 9.14). It is clear that the rate of cell division is not proportional to the underlying density of nuclei, especially along the longitudinal axis m, but the statistics are insufficient to say much more about the spatio-temporal dependence of the division rate.

9.2.3 Regeneration experiment

A regeneration experiment was conducted by imaging a root which had been cut approximately 100 μm from its tip using a 30G sterile dental needle under a dissecting microscope. This root expressed the H2B::YFP fusion and was imaged for 100 hours; example images are shown in Figure 9.15. The dynamics of growth and intensity for this experiment are shown in Figures 9.16 and 9.17. Further analysis has yet to be performed for this experiment.

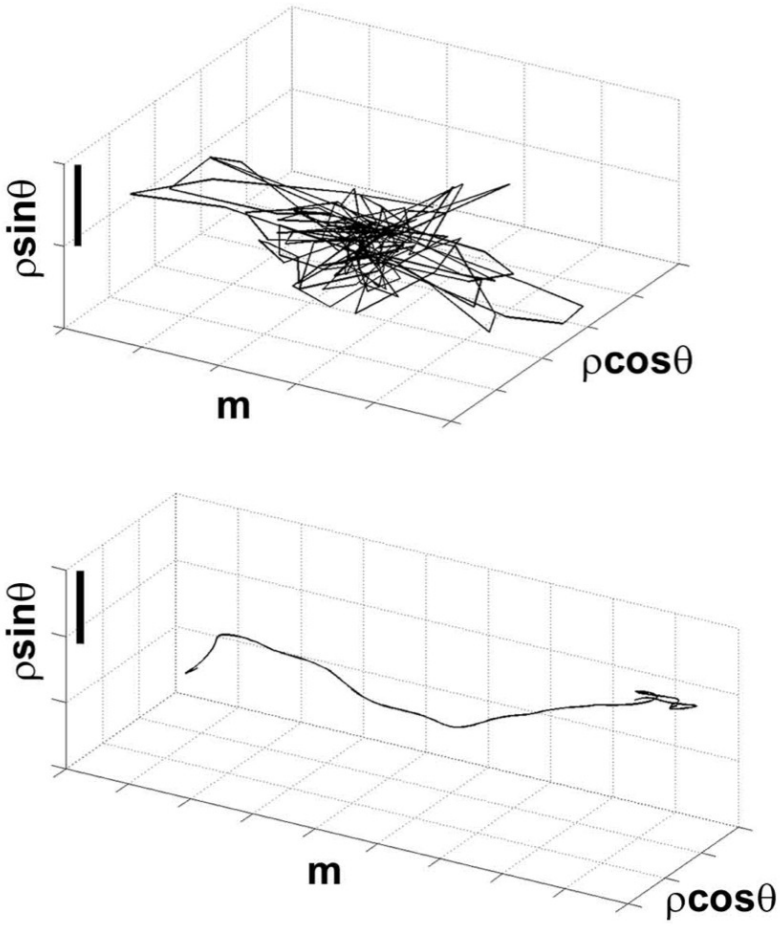

Figure 9.5: Trajectory of a single nucleus initially located near the root tip, decomposed into frequencies above (top plot) and below (bottom plot) the threshold of 0.23 hr^{-1} shown in Figure 9.4. The scale bar is 1 μm for the top plot and 20 μm for the bottom plot.

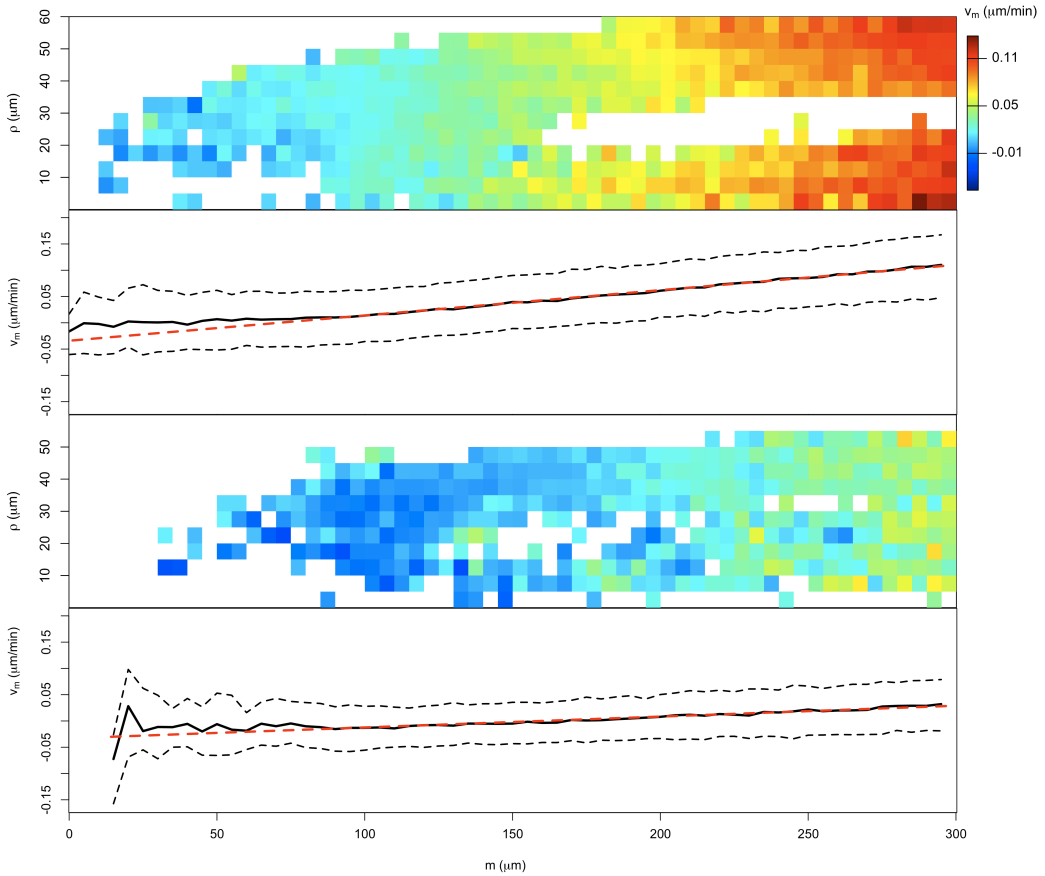

Figure 9.6: Heat maps and plots showing spatial dependence of longitudinal velocity - Longitudinal component of velocity v_m for early (0-20 hours, top) and late times (21-29 hours, bottom), with red line showing linear fit for region 80-300 μm, corresponding to expansion rates of $3.0 \times 10^{-2}\,\mathrm{hr}^{-1}$ for early times and $1.4 \times 10^{-2}\,\mathrm{hr}^{-1}$ for late times. Heatmaps show data for all bins having 36 or more data points; plots show median and upper and lower quartiles for each bin.

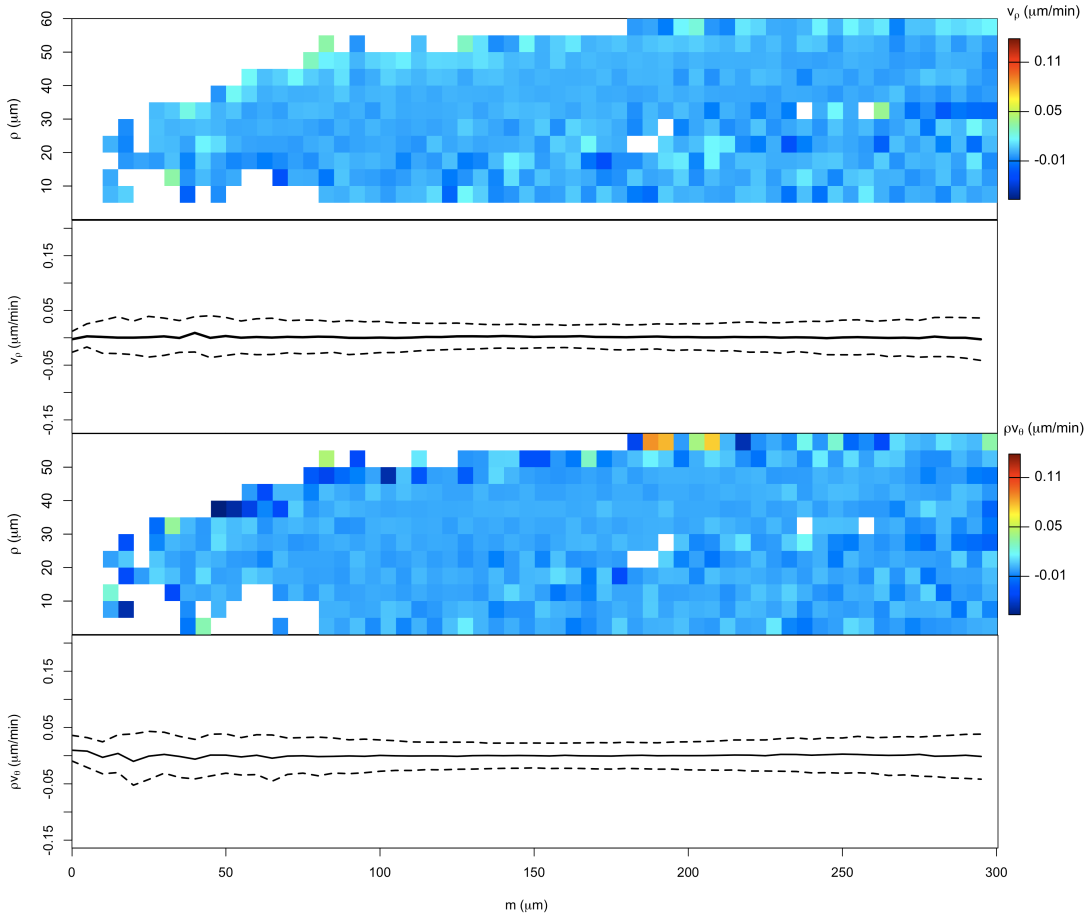

Figure 9.7: Heat maps and plots showing spatial dependence of radial and angular velocites - (top) radial component v_ρ for all times, (bottom) angular component ρv_θ for all times. Heatmaps show data for all bins having 36 or more data points; plots show median and upper and lower quartiles for each bin.

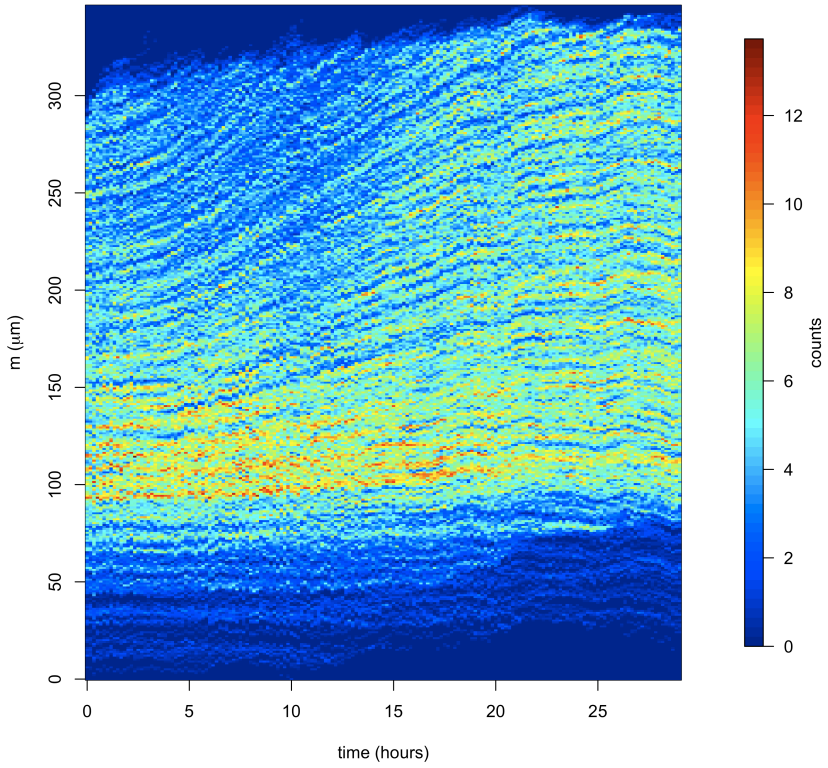

Figure 9.8: Nuclear density as a function of m and time - Data is presented as a histogram, in counts per time point per 2 μm bin.

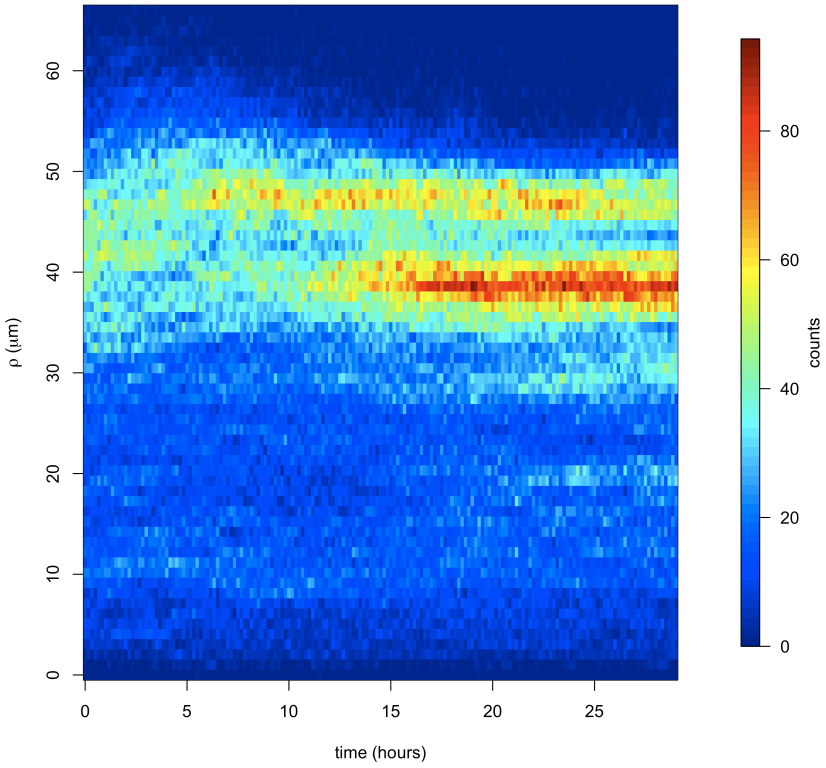

Figure 9.9: Nuclear density as a function of ρ and time - Data is presented as a histogram, in counts per time point per 1 μm bin.

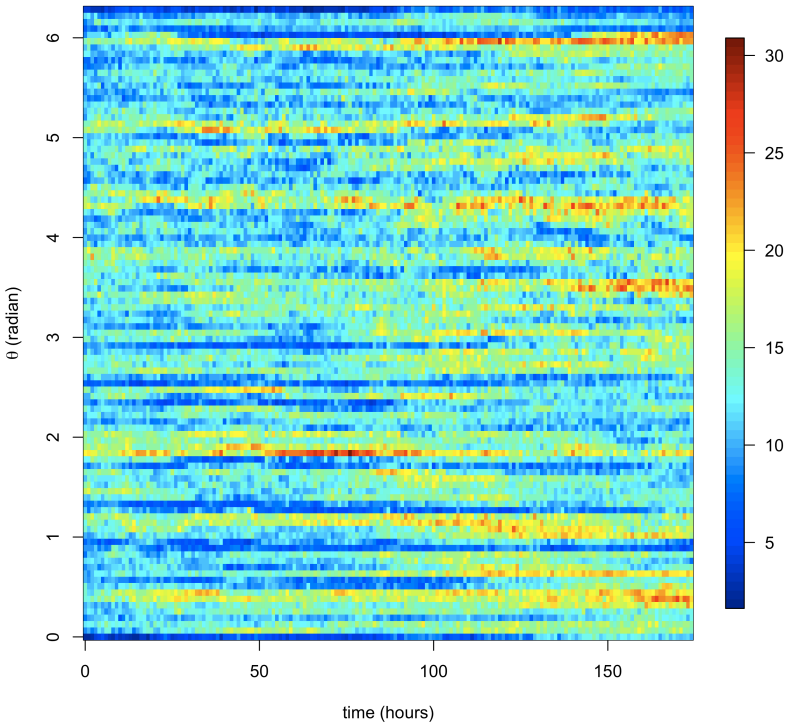

Figure 9.10: Nuclear density as a function of θ and time - Data is presented as a histogram, in counts per time point per 63 mrad bin.

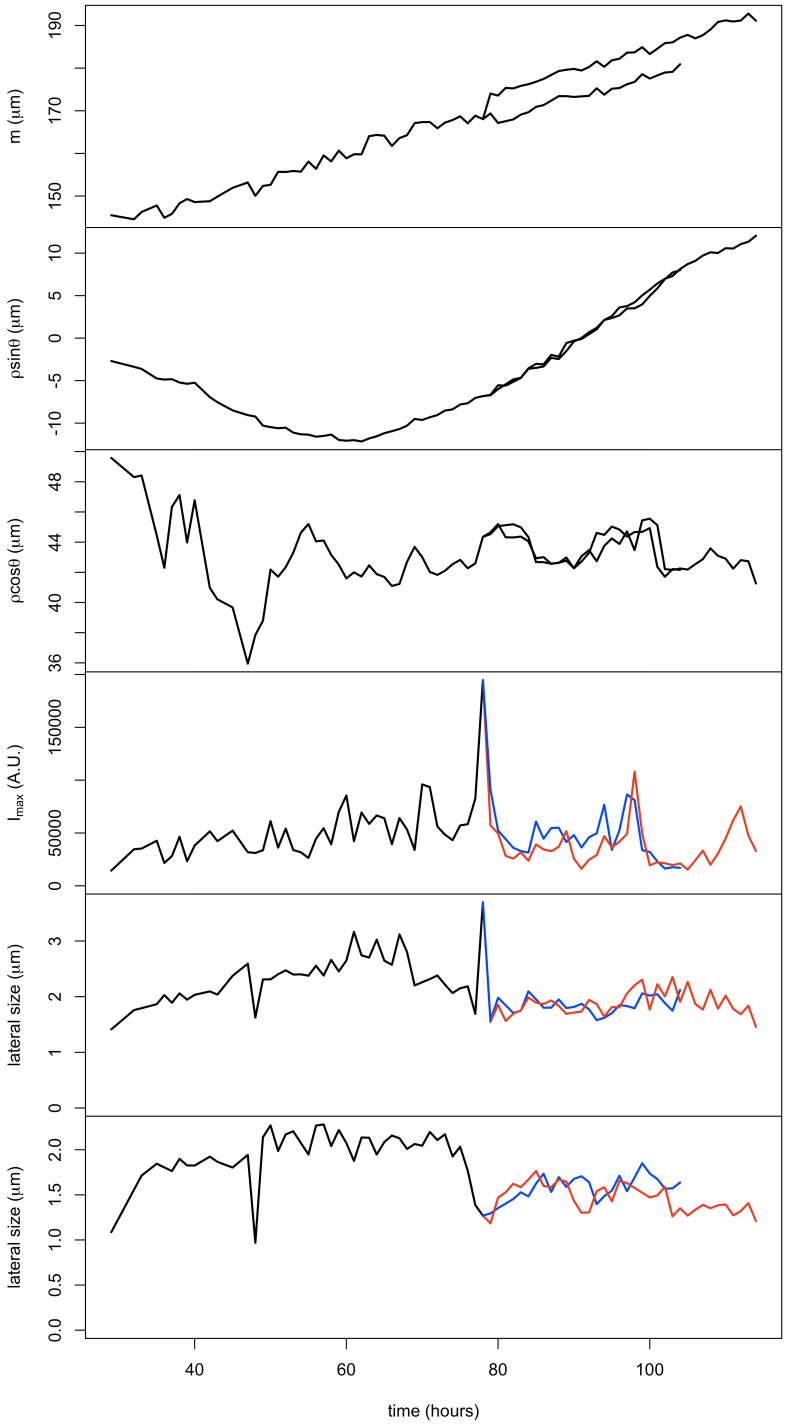

Figure 9.11: Time series of a typical dividing trajectory - From top to bottom are plotted coordinates m, $\rho \sin\theta$, and $\rho \cos\theta$, maximum intensity I_{max}, and lateral spatial moments of intensity λ_1 and λ_2.

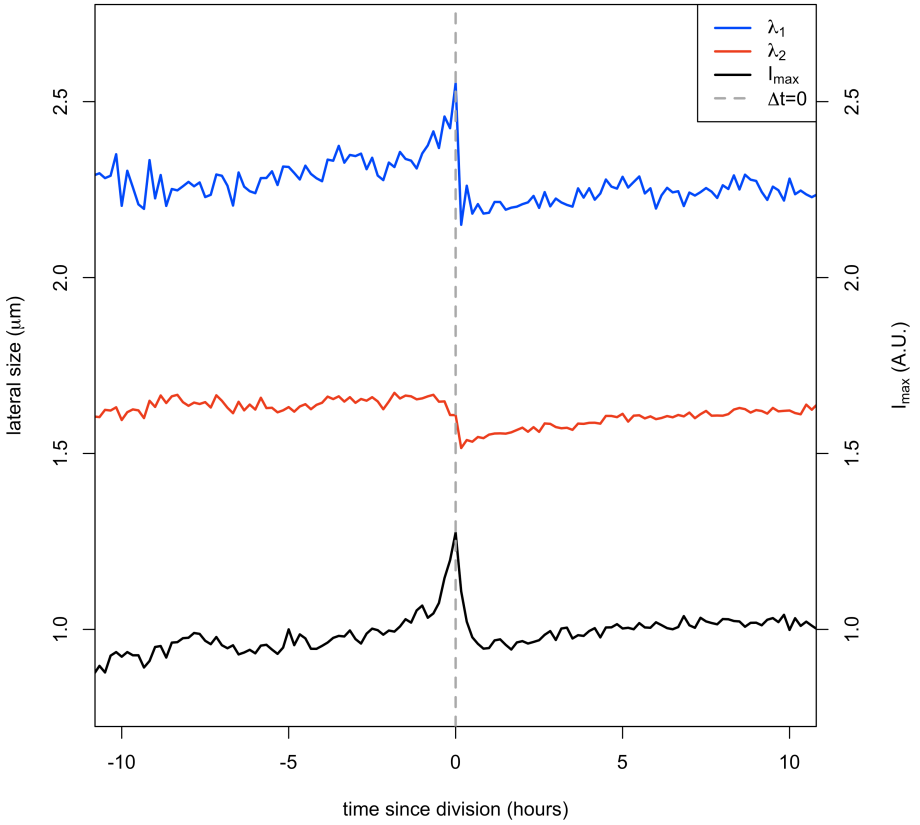

Figure 9.12: Mean behavior for all automatically identified cell divisions - The horizontal axis represents the time since division in hours. The larger and smaller lateral spatial moments are plotted in blue and red, respectively, and the normalized intensity is plotted in black. The dotted gray line denotes the time point immediately before cell division was identified.

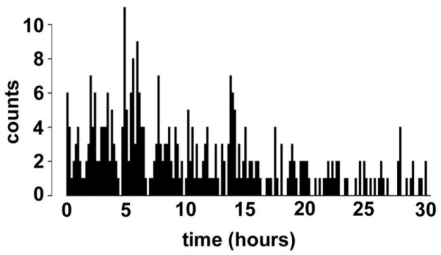

Figure 9.13: Time series of automatically identified cell divisions.

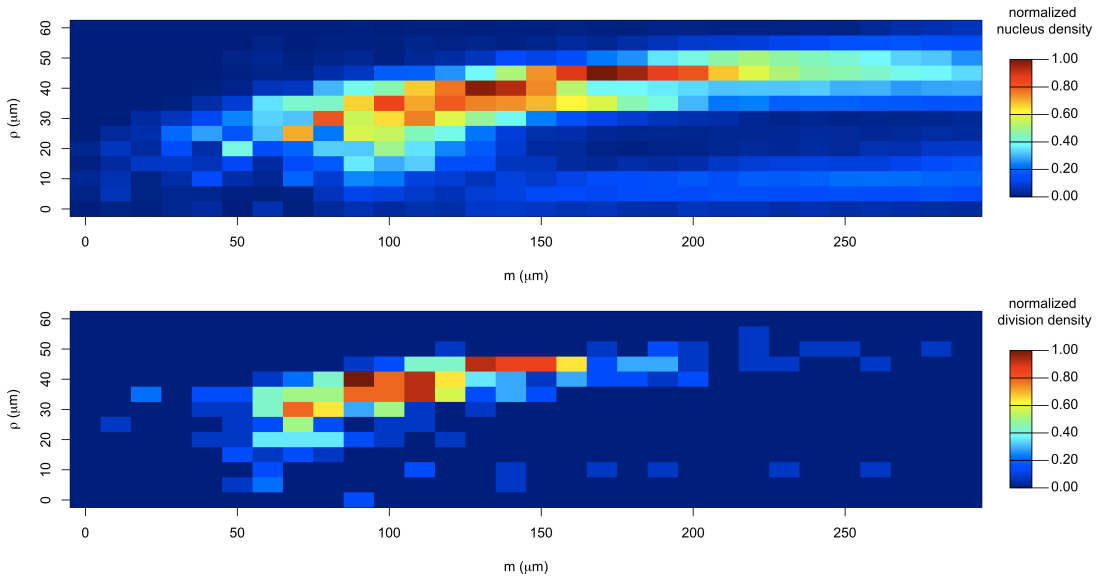

Figure 9.14: Heat maps comparing spatial distribution of nuclei weighted by times of cell divisions (top) to spatial distribution of cell divisions.

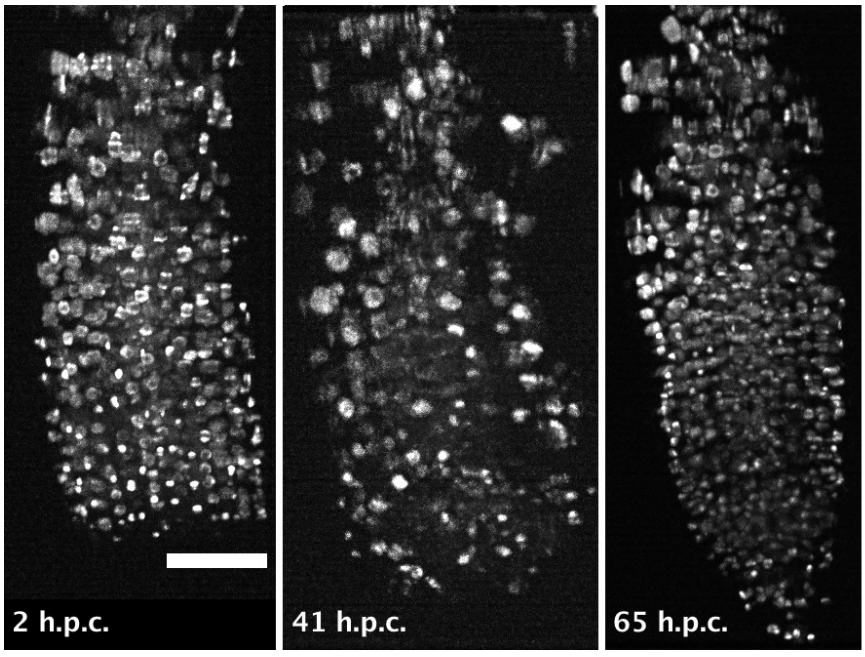

Figure 9.15: TLSM images of root regeneration - Maximum axial projections of intensity imaged from a regenerating root. Panels show data from 2, 41 and 65 hours post cut (h.p.c.), scale bar is 50 μm.

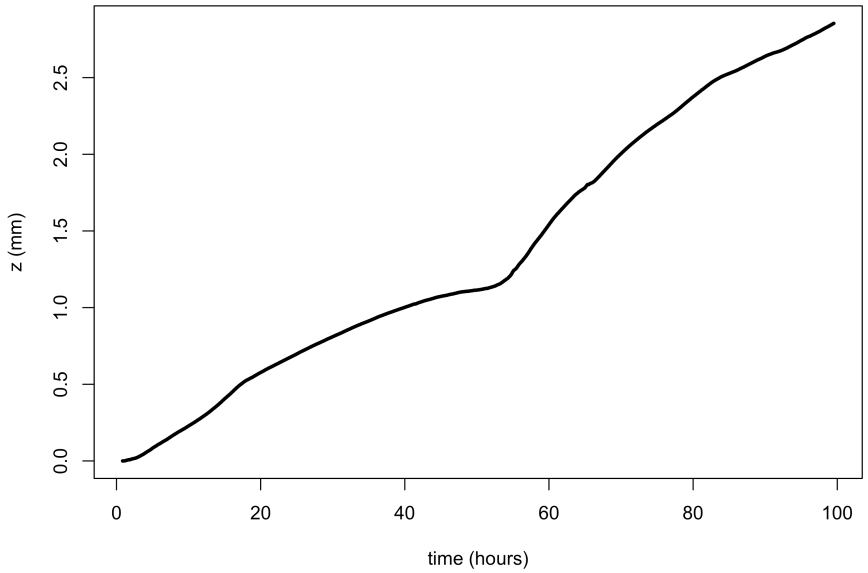

Figure 9.16: Growth dynamics of regenerating root

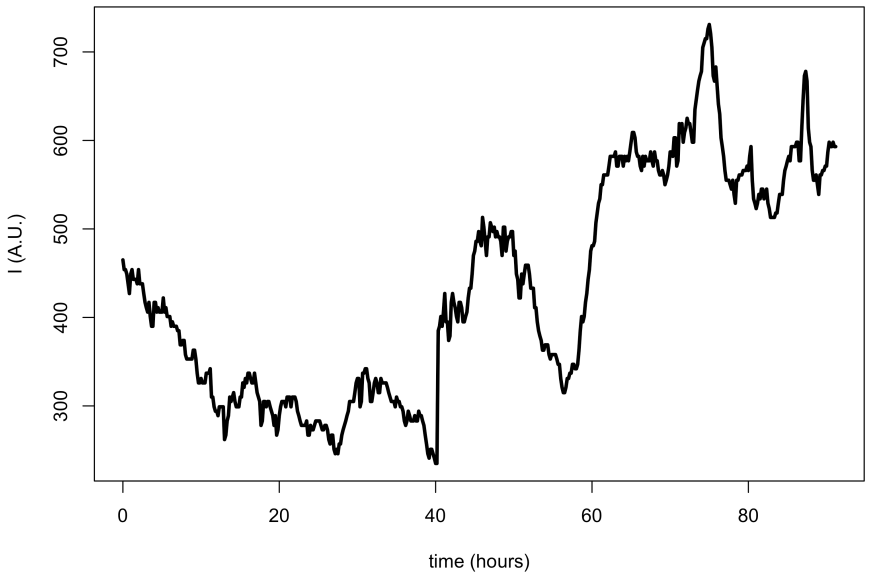

Figure 9.17: Intensity dynamics of regenerating root - intensity of highest 0.3% intensity quantile of raw images vs. time.

9.3 Conclusions

The incorporation of TLSM with a growth chamber and perfusion system specifically designed to maintain optimal conditions for imaging while supporting long term growth of the plant has allowed us to acquire at a temporal resolution of minutes high quality fluorescence images which resolve nuclei. In principle the acquisitions can continue indefinitely, thanks to the limited photobleaching and phototoxicity of the imaging technique and the accuracy of the sample tracking routine; we have presented results from experiments lasting over 4 days. The techniques for analysis allow automated identification of nuclei without spatial bias, and tracking of these nuclei over time reveals small scale collective motions as well as patterns of cell division. These observations largely corroborate earlier work; for example, a zone of elongation is known in *Arabidopsis*(1), although the scope of the data from our experiments is unprecedented. In addition, images have been acquired from a root regenerating after surgical excision, although analysis remains to be conducted. Following the acquisition of more data, the spatial-temporal correlations of cell divisions can be determined, both for uncut and cut roots. This should identify regions of the root which are important for regeneration if they exist; otherwise, mechanisms for global coordination may be involved.

Bibliography

[1] Gerrit T. S. Beemster and Tobias I. Baskin. Analysis of cell division and elongation underlying the developmental acceleration of root growth in *Arabidopsis thaliana*. *Plant Physiology*, 116:1515–1526, 1998. 185

[2] Liam Dolan, Kees Janmaat, Viola Willemsen, Paul Linstead, Scott Poethig, Keith Roberts, and Ben Scheres. Cellular organisation of the *Arabidopsis thaliana* root. *Development*, 119:71–84, 1993. 169